Regional Assessment of Tsunami Potential in the Gulf of Mexico

Report to the National Tsunami Hazard Mitigation Program

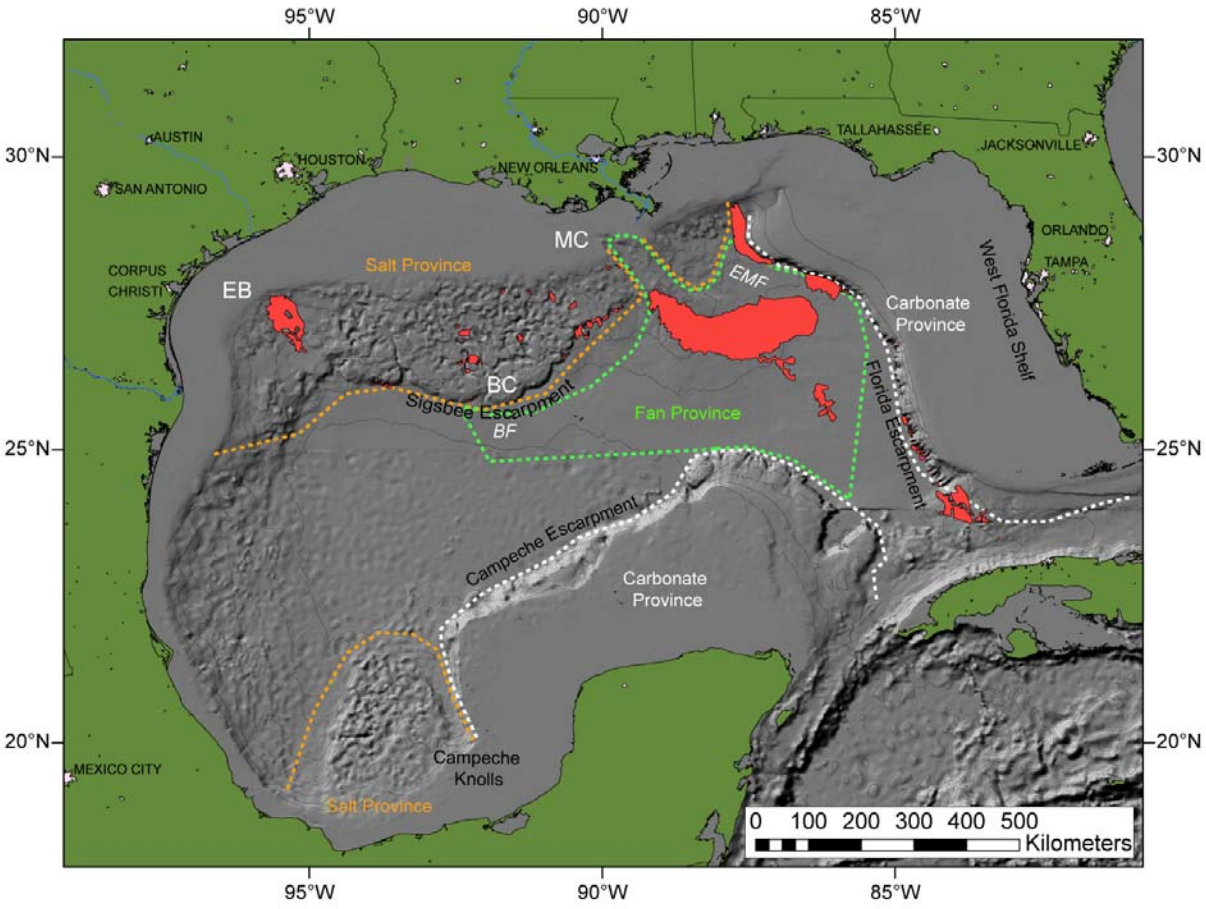

USGS
science for a changing world

Regional Assessment of Tsunami Potential in the Gulf of Mexico

Report to the National Tsunami Hazard Mitigation Program

Uri ten Brink[1], David Twichell[1], Patrick Lynett[2], Eric Geist[3], Jason Chaytor[1], Homa Lee[3], Brian Buczkowski[1], and Claudia Flores[1]

[1] U.S. Geological Survey, Woods Hole Science Center, Woods Hole, Massachusetts, USA
[2] Department of Civil Engineering, Texas A&M University, College Station, Texas, USA
[3] U.S. Geological Survey, Menlo Park, California, USA

September 2, 2009

NOTICE from USGS

This report should be cited as:

Regional Assessment of Tsunami Potential in the Gulf of Mexico: U.S. Geological Survey Administrative Report.

This report was compiled for the National Tsunami Hazard Mitigation Program

Cover: Shaded bathymetry of the Gulf of Mexico. Landslide deposits are marked in red. The three primary geologic provinces of the region are highlighted by the dashed lines. EB-East Breaks Landslide, MC-Mississippi Canyon, BC-Bryant Canyon, EMF-East Mississippi Fan, BF-Bryant Fan, MF-Mississippi Fan. Bathymetry derived from Armante and Eakins (2008)

Executive Summary

Assessment of natural hazards typically relies on analysis of past occurrences of similar disaster events. The assessment of tsunami hazard along the Gulf of Mexico coast of the United States poses a scientific challenge because of the paucity of both historical events and prehistoric tsunami evidence. The gulf coast of the U.S. is highly vulnerable to tsunami damage because major population centers and industrial facilities are located near the shoreline at low-lying elevations. This is in comparison with the Pacific coast of the United States where tsunamis are more frequent but the coastal regions are more sparsely populated and the emergent coastline has much greater relief. Therefore, the challenge for scientists is to define and quantify the hazard for these rare events.

Tsunami run-up can be significant along coastlines proximal to submarine landslides, as exemplified by the 1929 Grand Banks tsunami, offshore Nova Scotia, although the length of the coastline being affected by these tsunamis is much smaller than that impacted by earthquake-generated tsunamis. Therefore, a significant portion of this report is devoted to tsunami hazard from submarine landslides. The following summary is based on our observations and modeling results:

- There is sufficient evidence to consider submarine landslides in the Gulf of Mexico as a present-day tsunami hazard, as there are clear observations of large landslides along the continental margin of the gulf.
- Three geologic landslide provinces are defined in the Gulf of Mexico: Northwest Gulf of Mexico, Mississippi Canyon and fan, and Florida/Campeche Margin.
- Parameters for the maximum credible submarine landslide were determined for each of the provinces, except for the Florida/Campeche Margin where data are unavailable. All provinces contain landslides of sufficient volume to cause destructive tsunamis along the Gulf of Mexico Coasts.
- Mobility analysis suggests that constitutive parameters of the East Breaks landslide in the Northwest Gulf of Mexico are similar to the parameters for other landslides that have recently been analyzed (Palos Verdes and Currituck).
- The largest landslides are found in the submarine canyon and fan provinces extending from present (Mississippi) and former larger rivers that emptied into the Gulf of Mexico. Available data suggests that these large landslides were probably active prior to 7,000 years ago, when large quantities of sediments were emptied into the Gulf. However, sediment supply, especially from the Mississippi river, continues to contribute to slope steepening and increasing fluid pore pressure in the sediments, which may lead to further landslide activity. On the northern Gulf continental slope, landslides may still be active, probably because of salt movement, but are small and may not pose a tsunami hazard. A more detailed evaluation and sampling are needed to validate these conclusions.
- Hydrodynamic modeling of potential maximum tsunamis from landslide sources was conducted for the East Breaks slide (south Texas) and for hypothetical slides

along the Florida/Campeche margin. Conservative initial conditions related to tsunami generation efficiency, were used. Realistic wave propagation in two horizontal dimensions yielded potential maximum tsunami runup of approximately 4 m (relative to mean sea level).

- It is likely that seismic seiche waves resulting from the 1964 Gulf of Alaska earthquake are nearly the highest that can be generated owing to a predominantly continental ray path for seismic surface waves from Alaska to the Gulf Coast.
- There are no significant earthquake sources within the Gulf of Mexico that are likely to generate tsunamis, despite recent seismic activity in the area. Tsunami propagation from significant earthquake sources outside the Gulf of Mexico, such as the northern Panama Convergence Zone, Northern South America, Cayman Trough, the Puerto Rico trench, or the Gibraltar area shows that wave amplitude is greatly attenuated by the narrow and shallow passages into the gulf, and as a result, these tsunami sources do not constitute a tsunami hazard to the Gulf of Mexico coast.

Although the Gulf of Mexico is one of the most intensely studied ocean basins because of the energy resources it contains, information for understanding the timing, style, and distribution of landslides is still incomplete. Multibeam bathymetry is not publicly available either for the Mexican margin or for the northern part of the Florida Escarpment, the West Florida Slope, or the slope in the northwestern corner of the Gulf of Mexico. Little published information could be found on landslides along the Mexican margin preventing critical evaluation of hazards originating from this area. Acquisition of bathymetric data would improve our understanding of recent landslide source areas and triggering mechanisms.

Timing of landslides in the Gulf of Mexico needs to be refined to determine the likelihood of modern landslides and potential for future landslide-generated tsunamis. For example, it is not known if the Mississippi Fan landslides are associated with glacial melt water floods that discharged into the Gulf of Mexico, or whether they occurred more recently. Available age dates indicate that this large landslide complex is younger than 11,100 y BP, but the minimum age is still unknown. Additional modeling of potential sources is required to determine the magnitude of the initial waves, the amount of shallow water amplification, and the level of run-up expected at points around the Gulf of Mexico.

Table of Contents

Chapter 1: Distribution of Submarine Landslides in the Gulf of Mexico

Introduction

Submarine landslides have been studied in the Gulf of Mexico for two reasons: first they can pose a hazard to offshore platforms and pipelines for hydrocarbon extraction and transportation and second, when more deeply buried, they can serve either as hydrocarbon reservoirs or barriers in reservoirs depending on their composition. The threat of submarine landslides as a generator of tsunamis has not been addressed for the Gulf of Mexico region. Here we present a brief review of the literature on the distribution and style of submarine landslides that have occurred in the Gulf of Mexico during the Quaternary. This review will focus on landslides that have occurred on the continental slope and rise in the Gulf of Mexico; with much of the discussion focused on the part of the basin within the U.S. EEZ due to the availability of a greater number of publications from this region.

Setting

The Gulf of Mexico is a small, geologically diverse ocean basin that includes three distinct geologic provinces: a carbonate province, a salt province, and a canyon to deep-sea fan province (Figure 1-1). The basement under the deep Gulf of Mexico is Upper Triassic to Lower Jurassic oceanic or transitional crust (Sawyer et al., 1991). The stratigraphy of the overlying deposits records the subsequent evolution of this small ocean basin (Buffler, 1991). Three particular aspects of the basin's evolution that should be considered in an assessment of landslide activity within the basin are the Jurassic-aged salt that was deposited during the early stages of the opening of this ocean basin (Salvador, 1991a), the development and growth of extensive carbonate reef tracts during the late Jurassic and Cretaceous (Bryant et al., 1991), and the siliciclastic sediment input from the North American continent during the latest Mesozoic and Cenozoic (Buffler, 1991).

Salt deposited in the late Jurassic Gulf of Mexico basin, the Louann salt, originally underlay large parts of Louisiana, southern Texas, and the area offshore of Mexico in the Bay of Campeche (Salvador, 1991a). As sediment eroded from the North American continent was deposited on this salt sheet throughout the Mesozoic and Cenozoic, the increased load caused the salt to flow with it migrating southward from the source area into the northern Gulf of Mexico (Salvador, 1991b; Diegel et al., 1995). Presently the Louann salt underlies large parts of the northern Gulf of Mexico continental shelf and continental slope. South of Louisiana and Texas, the Sigsbee Escarpment is a pronounced cliff that marks the seaward limit of the shallowest salt tongue (Bryant et al., 1991) (Figure 1-3a). As

the salt is loaded, it flows seaward as sheets and tongues up toward the surface as cylindrical salt domes. The morphology of the salt sheet varies considerably across the margin. Salt domes are most common under the continental shelf, and most of the original salt sheet between individual domes in this region has been removed in response to the sediment loading, and migrated farther seaward. Under the upper and middle continental slope the salt is shaped into a network of ridges and narrow salt sheets that are interrupted by sub circular basins, (referred to in this chapter as mini-basins) which have thin salt or no salt underlying them. Farther down slope, immediately north of the Sigsbee Escarpment, the salt is more sheet-like in appearance and has a thin sediment cover over it (Diegel et al., 1995). Rates of salt movement are largely due to the confining pressure of sediment deposition. Calculated rates of salt motion range from as high as 17 cm/year to as low as only a few cms/1,000 yrs (Lowrie et al., 1991).

In the southwestern corner of the Gulf, in the Bay of Campeche, the seafloor has an irregular morphology that is similar to that of the northern Gulf of Mexico slope and appears to be the result of sediment loading an underlying salt deposit (Figure 1-1; Worzel et al., 1968; Martin and Bouma, 1978).

During the Mesozoic, an extensive reef system developed around much of the margin of the Gulf of Mexico Basin by the vertical growth of reefs and carbonate shelf edge banks (Bryant et al., 1969; Sohl et al., 1991). This reef system is exposed along the Florida Escarpment and the Campeche Escarpment that fringe the eastern and southern margins of this basin (Figure 1-1). These escarpments stand as much as 1,500 m above the abyssal plain floor, and have average gradients that commonly exceed 20° and locally are vertical (Jordan and Stewart, 1959; Paull et al., 1990a). Reef growth ended during the Middle Cretaceous (Freeman-Lynde, 1983; Locker and Buffler, 1984; Paull et al., 1990b), and subsequently the platform edges have been sculpted and steepened by a variety of erosional processes (Freeman-Lynde, 1983; Corso et al., 1989; Paull et al., 1991; Twichell et al., 1996). The tops of the steep escarpments are in 1,500-2,500 m of water, and above these steep cliffs is a slope with a markedly gentler gradient (Figure 1-2a).

A huge volume of continental sediment has been supplied to the deep Gulf of Mexico basin from the North American continent during the Cenozoic through submarine canyons. These sediments were deposited in the central deep part of the Gulf of Mexico as a series of deep-sea fans. The oldest sediments were deposited in the western part of the basin, and the depocenter shifted progressively eastward (Buffler, 1991). Three fan systems formed during the Pliocene and Pleistocene: Bryant Fan (Lee et al., 1996; Twichell et al., 2000), Mississippi Fan (Weimer, 1989), and Eastern Mississippi Fan (Weimer and Dixon, 1994). The Mississippi Fan is the largest of these three fans, and covers most of the eastern half of the deep Gulf of Mexico basin and reaches 4 km in thickness under the upper fan off the mouth of the Mississippi Canyon (Weimer, 1989; 1991). Sediment was supplied to the Mississippi Fan through the Mississippi Canyon which has retained its morphologic expression on the slope (Figure 1-1). The canyons that supplied sediment to Bryant and Eastern Mississippi Fans have been largely erased by salt movement (Weimer and Dixon, 1994; Lee et al., 1996; Twichell et al., 2000).

Types of Submarine Mass Movements

Several classification schemes exist for submarine mass movements. For this report we use one presented by Locat and Lee (2002) that was adapted from the classification of

subaerial mass movements proposed by the International Society for Soil Mechanics and Geotechnical Engineering (ISSMGE) Technical Committee on Landslides. While it has been observed that one type of mass movement can lead to another, here we briefly describe the end-member types.

- **Topples** – The displaced material usually is lithified rock that descends mainly through water as a coherent block that does not disintegrate during movement. Topples result in minimal lateral displacement.
- **Falls** – The displaced material mostly is lithified to semi-lithified material that is broken into smaller blocks and rubble during the failure process and descends mainly through water by falling, bouncing, and rolling. Falls also result in minimal lateral displacement.
- **Rotational slides** – The failed material undergoes rotation along a curved slip surface during displacement. This material tends to be rigid although in some cases beds within the failed mass are folded but do not undergo disintegration during translation.
- **Translational slides** – The failed material is translated along a discrete, flat slip surface. The material is rigid, and thus maintains its internal stratigraphy; however displacement can be great distances.
- **Debris flows** – Mass movements in which the failed material disintegrated during transport, and results in the deposit being a heterogeneous mix of clasts supported in a matrix of fine sediment. The clasts in debris flows vary in size and sediment texture.
- **Mudflows** – Mass movements of predominantly fine-grained material. These are similar to debris flows, but because of the more uniform texture their internal structure is not as clearly defined.
- **Turbidity currents** – Mass movements that involve the down slope movement of a relatively dilute suspension of sediment grains that are supported by the upward component of fluid turbulence.

Distribution of Submarine Landslides

Submarine landslides have occurred in each of the three provinces of the Gulf of Mexico basin although they vary in style and size among these different provinces. Landslides also have been active throughout much of the history of this basin, but this report will focus mostly on those that occurred during the Quaternary Period.

Carbonate Province

Landslides in the carbonate provinces that fringe the eastern and southern Gulf of Mexico appear to have been derived from both the steep West Florida and Campeche Escarpments as well as from the gentler slopes above these escarpments (Figure 1-2A). On the escarpments themselves, the amount and style of erosion varies along their lengths. Landslides have removed material from the gentler slope above the Florida Escarpment as well, but this process apparently has acted on different parts of the West Florida Slope at

different times. No information could be found on the processes acting on the slope above the Campeche Escarpment.

The presence of reef structures under the northern part of the Florida Escarpment suggests this part of the cliff has undergone little erosion since it originally formed during the Cretaceous (Locker and Buffler, 1984; Corso *et al.*, 1989; Twichell *et al.*, 1990). In fact, sidescan sonar imagery suggest that the only erosion along this section of the escarpment is the removal of a thin veneer of younger sediment that has accumulated as thin turbidity current or debris flow deposits at the foot of the escarpment (Figure 1-2B).

The carbonate platform edge that is exposed along the southern part of the Florida Escarpment and the Campeche Escarpment has been eroded since its initial formation and lagoonal facies are now exposed on the cliff face (Freeman-Lynde, 1983; Paull *et al.*, 1990b). The present morphology of these sections of the escarpments is quite different from the northern part of the Florida Escarpment (Figure 1-2A). Here canyons with steep sides and near-vertical headwalls, called box canyons (Paull *et al.*, 1991), incise these parts of the escarpments. These box canyons may be the result of dissolution of the limestone by discharge of acidic groundwater at the base of the escarpment in the canyon heads that resulted in collapse of the steep canyon headwalls (Paull *et al.*, 1990a).

A large talus deposit has been identified in seismic profiles along the base of the Campeche Escarpment that was deposited prior to the mid-Cretaceous (Schlager *et al.*, 1984; Locker and Buffler, 1984). The full extent of this deposit is unknown because of limited seismic coverage. Breccia recovered from a DSDP (Deep Sea Drilling Program) hole near the base of the Campeche Escarpment (Schlager *et al.*, 1984; Halley *et al.*, 1984) presumably is the result of topples and falls from the escarpment face. The amount of material associated with an individual failure is unknown. Talus blocks up to 5-m across and rubble have been observed on the seafloor along the base of the southern part of the Florida Escarpment which suggests this cliff has recently undergone erosion (Paull *et al.*, 1990a; Twichell *et al.*, 1990). The talus deposits in the heads of some of the box canyons cover areas less than 15 km^2, and their thickness is unknown. Published information suggests that the recent falls and topples were limited to the southern part of the Florida Escarpment and perhaps the Campeche Escarpment (Twichell *et al.*, 1996), but those that have been mapped are of limited aerial extent and are concentrated in the heads of box canyons (Figure 1-2b).

Landslides on the West Florida Slope above the Florida Escarpment are sourced in Tertiary and Quaternary carbonate deposits. Mullins *et al.* (1986) mapped large collapse scars along the central part of the West Florida Slope near the latitude of Tampa, FL (Figure 1-2B). The entire slide scar is 120 km long, 30 km wide, and has 300-350 m relief. While the total volume of material removed is around 1,000 km^3, there were at least 3 generations of failures with most of the sediment removal occurring prior to the middle Miocene. Presently these landslide scarps are buried and only local episodic failures have subsequently occurred along this section of the slope (Doyle and Holmes, 1985). Along the southern part of the West Florida Slope, Doyle and Holmes (1985) and Twichell *et al.* (1993) have mapped another extensive area of the slope that has undergone collapse (Figure 1-2B). Here the scarps are still exposed on the seafloor and have 50-150 m relief and are 10-70 km in length. Some of the mass-movement deposits are on the slope above the Florida Escarpment, but it is unknown how much of the failed material was transported farther and deposited at the base of the Florida Escarpment. The cross-cutting of the headwall scarps clearly imaged by recent multibeam data, indicates that these landslides are composed of several smaller failure events (Twichell *et al.*, 1993). The age of these failures is not known, but Mullins *et al.* (1986) and Doyle and Holmes (1985) suggest periods of increased mass wasting which are probably

associated with periods of higher sedimentation rates. If this is the case, then the landslides along the southern part of the West Florida Slope are most likely early Holocene or older in age (Doyle and Holmes, 1985).

Salt Province

No published information has been found on landslides in the salt province in the Bay of Campeche, so this discussion will focus on the northern Gulf of Mexico slope where further information is available on landslides. Presumably the northern Gulf is an appropriate analogue for the Bay of Campeche area (Figure 1-1). Detailed bathymetric mapping of the salt province in the northern Gulf of Mexico shows that it has a unique morphology characterized by relatively small sub-circular basins that have areas of 5-312 km^2 (Figure 1-3). These basins are bordered by narrow salt-cored ridges that stand 50-521 m above the basin floors (Pratson and Ryan, 1994).

Landslide deposits have been mapped in several of the mini-basins using GLORIA imagery (Rothwell *et al.*, 1991; Twichell *et al.*, 2000; Twichell *et al.*, 2005) as well as with high-resolution sidescan sonar, high resolution seismic profiles, and cores (Behrens, 1988; Lee and George, 2004; Orange *et al.*, 2003; 2004; Sager *et al.*, 2004, Silva *et al.*, 2004; Tripsanas *et al.*, 2004a; 2004b). The GLORIA imagery provides a regional perspective on the size and distribution of landslides, while the detailed studies provide more information on the types of failures. The GLORIA imagery identified 37 landslides in the salt province and along the base of the Sigsbee Escarpment (Figure 1-3a). The largest of these failures occurs in the northwestern Gulf of Mexico, is 114 km long, 53 km wide, covers about 2,250 km^2, and has been interpreted to consist of at least two debris flows (Rothwell *et al.*, 1991; McGregor *et al.*, 1993). This landslide, known as the East Break landslide, lies offshore of the Rio Grande River system and Rothwell *et al.* (1991) suggest it is the result of failure of the shelf edge delta that formed off this river during the last lowstand of sea level.

The remaining landslides within the salt province are considerably smaller and cover areas ranging from 4-273 km^2 (Figure 1-3b). Most have sources on the walls of the mini-basins or on the Sigsbee Escarpment. The detailed studies indicate a wide variety of landslide types that include translational slides, rotational slides, debris flows, and creep movements (Lee and George, 2004; Orange *et al.*, 2004; Silva *et al.*, 2004). It has been suggested that triggering mechanisms for these landslides include shallow stratigraphic layers with overpressured pore waters (Orange *et al.*, 2003), salt movement (Lee and George, 2004; Tripsanas *et al.*, 2004a), oversteepening of shelf edge deltas (Tripsanas *et al.*, 2004b), and possibly gas hydrates (Twichell and Cooper, 2000).

Information is limited on the age of landslides in the salt province. In the salt province south of western Louisiana (26º 30.4 N, 92º 06.1 W, 2422 meters water depth) the most extensive study (Tripsanas *et al.*, 2004a; b) indicates that most of the youngest landslides sampled in the salt province occurred during oxygen isotope stages 2, 3, and 4 (18,170-71,000 yr BP) when salt movement due to sediment loading was most active. One unpublished age date of a sample below a thin landslide deposit (< 3 m thick) indicates that it is younger than 6,360 yr BP (H. Nelson, personal communication). Localized failure of mini-basin walls may continue to be active, but available data suggests these small failures were more prevalent during the last lowstand of sea level. Chapter 5 discusses a possible landslide based on an interpretation of the 2006 Green Canyon Earthquake.

Canyon/Fan Province

Three canyon/fan systems formed during the Quaternary period; the Bryant, Mississippi, and Eastern Mississippi systems (Figure 1-1). Of these three systems, the Mississippi is the largest and youngest (Weimer, 1989). During the latest Pleistocene, sediment was supplied to the Mississippi Fan from a point source, the Mississippi Canyon (Bryant *et al*, 1991). Regional seismic stratigraphic analysis has been used to divide the Mississippi Fan into 17 seismic sequences (Weimer, 1989): most contain a basal chaotic unit inferred to be mass-transport deposits. The mass-transport deposits are overlain by channel-levee complexes, which are capped by a thin interval of hemipelagic sediment that represents a period of limited sediment input. Depositional style within each sequence has been attributed to changes in sea level: the mass-transport complexes were deposited during falling sea level and the initial part of the lowstand; the channel-levee complexes formed during the lowstand and the onset of the transgression; and condensed sections were deposited during highstands (Weimer, 1989). According to this interpretation, the Holocene should have been a period of quiescence.

However, studies of the Mississippi Canyon and present surface of the Mississippi Fan indicate a different stratigraphic progression (Twichell *et al*., 1990; Twichell *et al*., 2009) and reveal evidence of landslides at several scales. Turbidity current deposits and thin debris flow deposits associated with channel-levee development have been mapped and sampled on the distal fan (Twichell *et al*., 1990; Twichell *et al*., 1992; Nelson *et al*., 1992; Schwab *et al*., 1996). Some of these deposits have been mapped with sidescan sonar and cores and are relatively small: covering areas less than 331 km^2, and having volumes less than 1 km^3 (Twichell *et al*., 2009). At the other extreme is a large landslide complex that covers approximately 23,000 km^2 of the middle and upper fan (Figure 1-4) and reaches 100 m in thickness (Walker and Massingill, 1970; Normark *et al*., 1986; Twichell *et a*l., 1992). The total volume of this deposit cannot be accurately estimated because of inadequate seismic coverage. A denser grid of high-resolution seismic data is needed to accurately estimate the complete volume, and to determine whether it failed as one event, or as a series of events. Available seismic profiles and GLORIA imagery suggest that this feature consists of at least two separate events (Twichell *et al*., 2009). The Mississippi Canyon appears to have the source area for these landslide deposits (Walker and Massingill, 1970; Coleman *et al*., 1983; Goodwin and Prior, 1989; Lowrie *et al*., 2004). Borings and seismic data from the head of Mississippi Canyon (Goodwin and Prior, 1989) indicate that there were alternating episodes of canyon filling and excavation between 19,000 and 7,500 yr BP, and Coleman *et al.* (1983) estimate total volume of sediment removed was approximately 8,600 km^3. One DSDP hole through this landslide deposit penetrated thick sections of tilted beds (Normark *et al*., 1986). This information in conjunction with the GLORIA imagery which shows a swirling pattern on the surface of the youngest part of this failure suggests it may be a translational slide that has undergone deformation but not complete disintegration as it moved (Figure 1-4).

The timing of these landslides needs to be refined to determine whether they are associated with glacial meltwater floods that discharged into the Gulf of Mexico (Laventer *et al*., 1982; Marchitto and Wei, 1995, Aharon, 2003), or whether they occurred more recently. Available age dates indicate that this large landslide complex is younger than 11,100 yr BP, when turbidity current and debris flow transport to the distal fan ceased due to the channel

being blocked by part of this landslide (Schwab *et al.*, 1996; Twichell *et al.*, 2009). This large landslide is older than 7,500 yr BP, when hemipelagic sedimentation resumed in Mississippi Canyon and covered the headwall scarps of the failures (Prior *et al.*, 1989). Meltwater discharge to the Gulf of Mexico ceased about 9,000 yr BP (Marchitto and Wei, 1995; Aharon, 2003). Refining the timing of these large landslides is needed to determine if they are associated with meltwater floods or are younger than the floods and formed under conditions similar to the present.

The Bryant and Eastern Mississippi Fans may both have canyon head failures associated with them as well. The Bryant Canyon system was immediately downslope of a shelf edge delta system (Morton and Sutter, 1996), and failure of this system has been proposed as the explanation for thick chaotic deposits in mini basins along the path of this canyon system (Lee *et al.*, 1996; Prather *et al.*, 1998; Twichell *et al.*, 2000; Tripsanas *et al.*, 2004a). Debris from the failure of the shelf edge delta was transported down the Bryant Canyon system (Lee *et al.*, 1996; Prather *et al.*, 1998), but these landslide deposits predate and are buried by the smaller landslides off the mini-basin walls that are shown in Figure 1-3 (Twichell *et al.*, 2000).

The Eastern Mississippi Fan system also has a relatively large landslide that partially buries the fan channel that supplied this fan (Figure 1-4). This landslide deposit is approximately 154 km long, as much as 22 km wide, and covers an area of 2,410 km^2. The volume of the deposit and its age are unknown.

Summary

Landslides occur in all three geologic provinces (carbonate, salt, and canyon/fan) in the Gulf of Mexico. The largest failures are found in the canyon/fan province. More information is needed on the timing of the large failures that filled the Bryant Canyon and covered the upper parts of the Mississippi and Eastern Mississippi Fans (Figure 1-1). The resumption of hemipelagic sedimentation in the head of Mississippi Canyon by 7,500 yr BP (Goodwin and Prior, 1988) indicates that at least the largest of these landslide complexes had ceased being active by mid-Holocene time. Further age dating is needed to refine the timing of the landslides derived from the Mississippi Canyon area to determine if they are associated with meltwater floods discharged into the Gulf of Mexico during the early part of the Holocene or whether they were triggered by other processes at a later time.

Figures

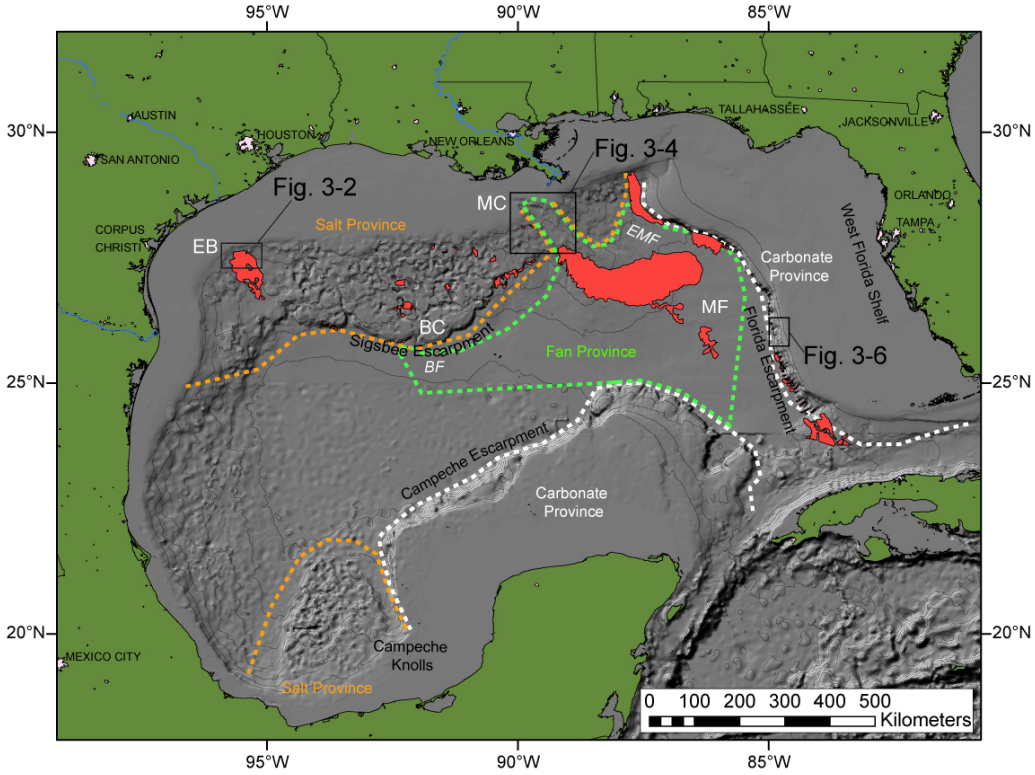

Figure 1-1: Shaded bathymetry of the Gulf of Mexico. Landslide deposits are marked in red. The three primary geologic provinces of the region are highlighted by the dashed lines. EB-East Breaks Landslide, MC-Mississippi Canyon, BC-Bryant Canyon, EMF-East Mississippi Fan, BF-Bryant Fan, MF-Mississippi Fan. Bathymetry derived from Armante and Eakins (2008)

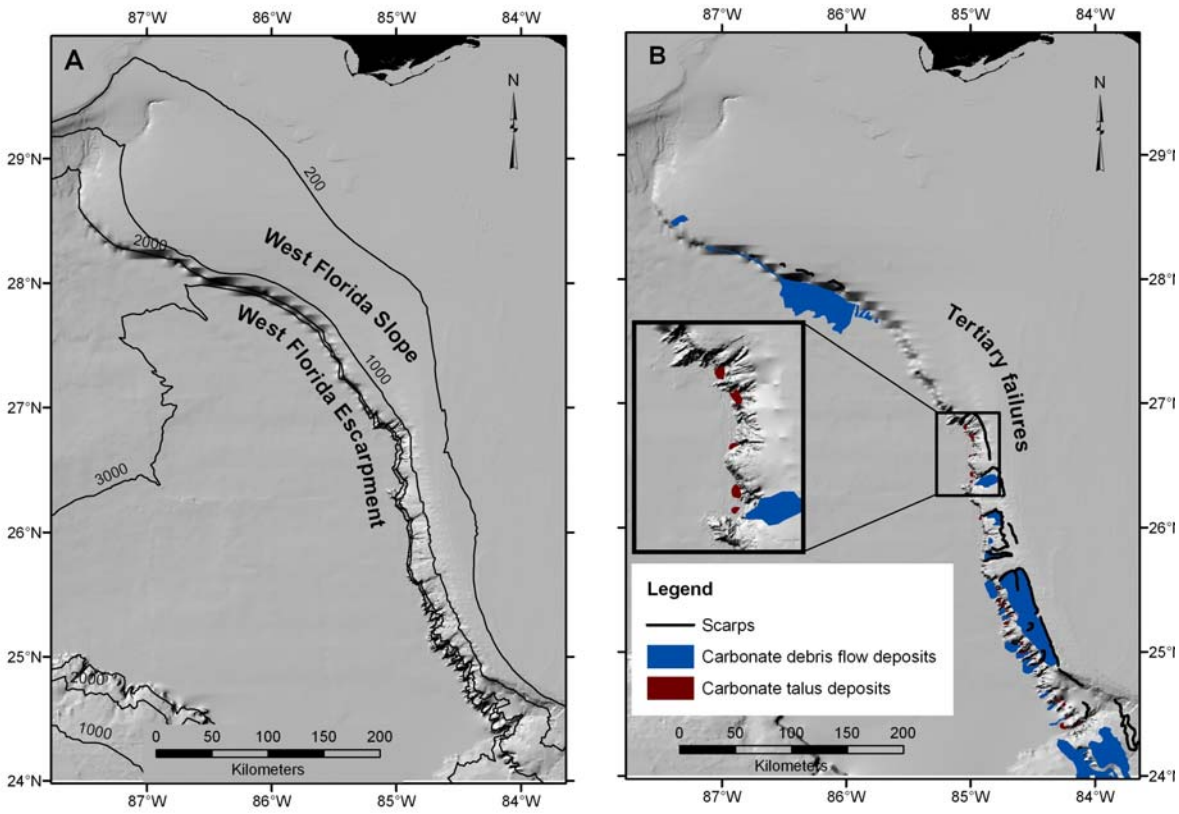

Figure 1-2: (A) Morphology of the West Florida Escarpment and the West Florida Slope, and (B) the extent and distribution of carbonate debris flow deposits and talus deposits derived from this part of the carbonate province. "Tertiary failures" marks the general location of older landslides mapped by Mullins *et al.* (1986) that now have been completely buried. Inset box shows a detailed view of some of the carbonate talus deposits. Equivalent information is not available for the slope above the Campeche Escarpment.

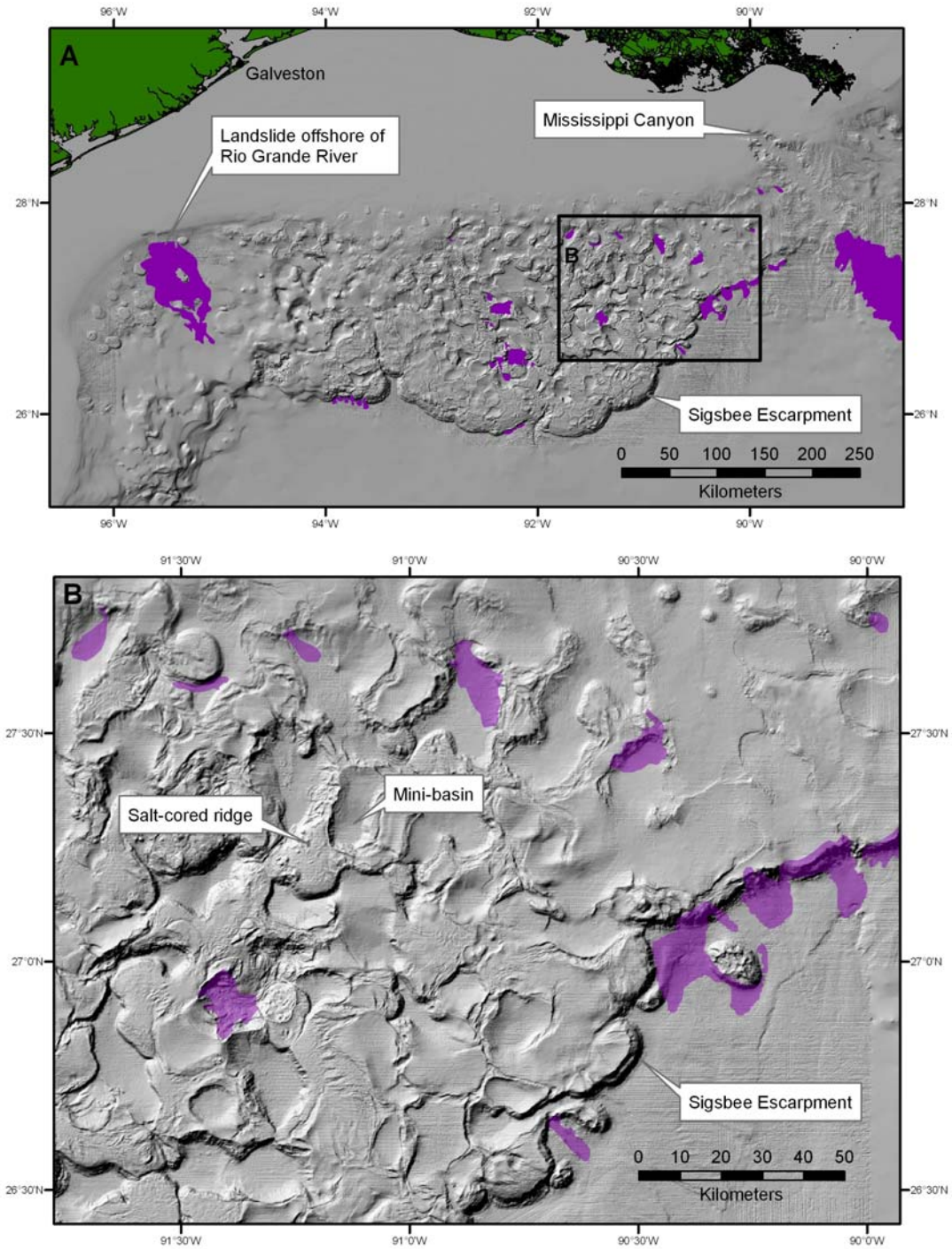

Figure 1-3: (A) Shaded relief image of a large part of the northern Gulf of Mexico salt deformation province west of Mississippi Canyon showing the irregular morphology of this continental slope and the distribution of landslides (purple areas), and (B) an enlarged view of part of this region showing the relation of landslides (purple areas) to the mini basins and the Sigsbee Escarpment.

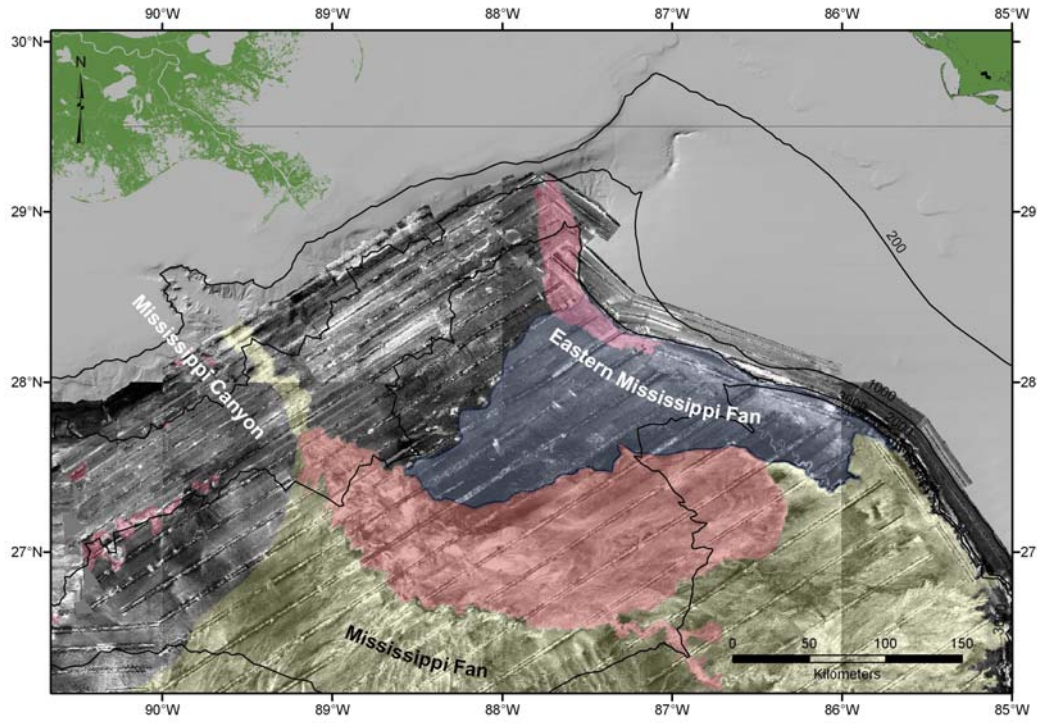

Figure 1-4: GLORIA sidescan sonar imagery showing part of the Mississippi Fan (light-yellow) and Eastern Mississippi Fan (indigo) and two large landslide areas (maroon) that spread across the upper parts of these two fans. The landslide on the upper Mississippi Fan was sourced from the Mississippi Canyon region (Coleman *et al.*, 1983) and is the largest Quaternary landslide found in the Gulf of Mexico.

References

Aharon, P., 2003, Meltwater flooding events in the Gulf of Mexico revisited: Implications for rapid climate changes during the last deglaciation: *Paleoceanography, v. 18*, 1079, doi: 10.1029/2002PA000840.

Armante C. and Eakins, B.W., 2008, ETOPO1 1 Arc-Minute Global Relief Model: Procedures, Data Sources and Analysis: National Geophysical Data Center, NESDIS, NOAA, U.S. Department of Commerce, Boulder, CO.

Behrens, W.E., 1988, Geology of a continental slope oil seep, northern Gulf of Mexico: *American Association of Petroleum Geologists Bulletin, v. 72*, p. 105-114.

Bryant, W.R., Lugo, J., Cordova, C., and Salvador, A., 1991, Physiography and bathymetry, *in* Salvador, A. (Editor), The Geology of North America, Vol. J, Gulf of Mexico Basin: Geological Society of America, Boulder, CO, p. 13-30.

Bryant, W.R., Meyerhoff, A.A., Brown, N.K., Furrer, M.A., Pyle, T.E., and Antoine, J.W., 1969, Escarpments, reef trends, and diapiric structures, eastern Gulf of Mexico: *American Association of Petroleum Geologists Bulletin, v. 53*, p. 2506-2542.

Buffler, R.T., 1991, Seismic stratigraphy of the deep Gulf of Mexico basin and adjacent margins, *in* Salvador, A. (Editor), The Geology of North America, Vol. J, Gulf of Mexico Basin: Geological Society of America, Boulder, CO, p. 353-387.

Coleman, J.M., Prior, D.B., and Lindsay, J.F., 1983, Deltaic influences on shelf edge instability processes, *in* Stanley, D.J., and Moore, G.T. (Editors), The shelfbreak: Critical interface on continental margins: Society of Economic Paleontologists and Mineralogists Special Publication 33, p. 121-137.

Corso, W., Austin, J.A., and Buffler, R.T., 1989, The early Cretaceous platform off northwest Florida: Controls on morphologic development of carbonate margins: *Marine Geology, v. 86*, p. 1-14.

Diegel, F.A., Karlo, J.F., Schuster, D.C., Shoup, R.C., and Tauvers, P.R., 1995, Cenozoic structural evolution and tectono-stratigraphic framework of the northern Gulf Coast continental margin, *in* Jackson, M.P.A.,

Roberts, D.G., and Snelson, S. (Editors), Salt tectonics: A global perspective: AAPG Memoir 65, p. 109-151.

Doyle, L.J., and Holmes, C.W., 1985, Shallow structure, stratigraphy, and carbonate sedimentary processes of West Florida Continental Slope: *American Association of Petroleum Geologists Bulletin, v. 69*, p. 1133-1144.

Freeman-Lynde, R.P., 1983, Cretaceous and Tertiary samples dredged from the Florida Escarpment, eastern Gulf of Mexico: *Transactions Gulf Coast Association of Geological Societies, v. 33*, p. 91-99.

Goodwin, R.H., and Prior, D.B., 1989, Geometry and depositional sequences of the Mississippi Canyon, Gulf of Mexico: *Journal of Sedimentary Petrology, v. 59*, p. 318-329.

Halley, R.B., Pierson, B.J., and Schlager, W., 1984, Alternative diagenetic models for Cretaceous talus deposits, Deep Sea Drilling Project site 536, Gulf of Mexico, *in*, Buffler, R.T., Schlager, W. *et al.*, Initial Reports of the Deep Sea Drilling Project v. 77, Washington DC, U.S. Government Printing Office, p. 397-408.

Jordan, G.F., and Stewart, H.B., 1959, Continental slope off southwest Florida: *American Association of Petroleum Geologists Bulletin, v. 43*, p. 974-991.

Laventer, A., Williams, D.F., and Kennett, J.P., 1982, Dynamics of the Laurentide Ice Sheet during the last deglaciation: Evidence from the Gulf of Mexico: *Earth and Planetary Science Letters, v. 59*, p. 11-17.

Lee, E.Y.D., and George, R.A., 2004, High-resolution geological AUV survey results across a portion of the eastern Sigsbee Escarpment: *American Association of Petroleum Geologists Bulletin, v. 88*, p. 747-764.

Lee, G.W., Watkins, J.S., and Bryant, W.R., 1996, Bryant Canyon fan system: An unconfined large river-sourced system in the northwestern Gulf of Mexico: *American Association of Petroleum Geologists Bulletin, v. 80*, p. 340-358.

Locat, J., and Lee, H. J., 2002, Submarine landslides: advances and challenges: *Canadian Geotechnical Journal, v. 39*, p. 193-212.

Locker, S.D. and Buffler, R.T., 1984, Comparison of Lower Cretaceous carbonate shelf margins, northern Campeche Escarpment and northern Florida Escarpment, Gulf of Mexico, *in* Bally, P.W. (Editor), Seismic Expression of Structural Styles – A Picture and Work Atlas, American Association of Petroleum Geologists Studies in Geology Series, No. 15, v. 2, p. 123-128.

Lowrie, A., Lutken, C.B., and McGee, T.M., 2004, Multiple outer shelf deltas and downslope massive mass-wastings characterize the Mississippi Canyon, northern Gulf of Mexico: *Transactions Gulf Coast Association of Geological Societies, v. 54*, p. 383-392.

Lowrie, A., Yu, Z., and Lerche, I., 1991, Hydrocarbon trap types and deformation styles modeled using quantified rates of salt movement, Louisiana margin: *Transactions-Gulf Coast Association of Geological Societies, v. 41,* p. 445-459.

Marchitto, T.M., and Wei, K., 1995, History of Laurentide meltwater flow to the Gulf of Mexico during the last deglaciation, as revealed by reworked calcareous nannofossils: *Geology, v. 23*, p. 779-782.

Martin, R.G., and Bouma, A.H., 1978, Physiography of Gulf of Mexico, *in* Bouma, A.H., Moore, G.T., and Coleman, J.M., eds., Framework, facies, and oil-trapping characteristics of the upper continental margin: American Association of Petroleum Geologists Studies in Geology no. 7, p. 3-19.

McGregor, B.A., Rothwell, R.G., Kenyon, N.H., and Twichell, D.C., 1993, Salt tectonics and slope failure in an area of salt domes in the northwestern Gulf of Mexico, in Schwab, W.C., Lee, H.J., and Twichell, D.C. (Editors), Submarine Landslides: Selected Studies in the U.S. Exclusive Economic Zone: U.S. Geological Survey Bulletin, 2002, p. 92-96.

Morton, R.A., and Suter, J.R., 1996, Sequence stratigraphy and composition of Late Quaternary shelf-margin deltas, northern Gulf of Mexico: *American Association of Petroleum Geologists Bulletin, v. 80*, p. 505-530.

Mullins, H.T., Gardulski, A.F., and Hine, A.C., 1986, Catastrophic collapse of the West Florida carbonate platform margin: *Geology, v. 14*, p. 167-170.

Nelson, C.H., Twichell, D.C., Schwab, W.C., Lee, H.J., and Kenyon, N.H., 1992, Late Pleistocene turbidite sand beds and chaotic silt beds in the channelized distal outer fan lobes of Mississippi Fan: Geology, v. 20, p. 693-696.

Normark, W.R., Meyer, A.H., Cremer, M., Droz, L., O'Connell, S., Pickering, K.T., Stelting, C.E., Stow, D.A.V., Brooks, G.R., Mazzullo, J., Roberts, H., and Thayer, P., 1986, Summary of drilling results for the Mississippi Fan and considerations for application to other turbidite systems, *in* Bouma, A.H., Coleman, J.M., Meyer, A.W., *et al.* (Editors), Initial Reports of the Deep Sea Drilling Project: U.S. Government Printing Office, Washington, D.C., v. 96, p. 425-436.

Orange, D.L., Angell, M.M., Brand, J.R., Thomson, J., Buddin, T., Williams, M., Hart, W., Berger, W.J., 2004, Geologic and shallow salt tectonic setting of the Mad Dog and Atlantis fields: Relationship between salt, faults, and seafloor geomorphology: *The Leading Edge, v. 23*, p. 354-365.

Orange, D.L., Saffer, D., Jeanjean, P., Khafaji, Z.A., Humphrey, G., and Riley, G., 2003, Measurements and modeling of the shallow pore pressure regime at the Sigsbee Escarpment: Successful prediction of overpressure and ground-truthing with borehole measurements: *The Leading Edge, v. 22*, p. 906-913.

Paull, C.K., Freeman-Lynde, R.P., Bralower, T.J., Gardemal, J.M., Neumann, A.C., D'Argenio, B., and Marsella, E., 1990b, Geology of the strata exposed on the Florida Escarpment: *Marine Geology, v. 91*, p. 177-194.

Paull, C.K., Spiess, F.N., Curray, J.R., and Twichell, D.C., 1990a, Origin of Florida Canyon and the role of spring sapping on the formation of submarine box canyons: *Geological Society of America Bulletin, v. 102*, p. 502-515.

Paull, C.K., Twichell, D.C., Spiess, F.N., and Curray, J.R., 1991, Morphological development of the Florida Escarpment: Observations on the generation of time transgressive unconformities in carbonate terrains: *Marine Geology, v. 101*, p. 181-201.

Prather, B.E., Booth, J.R., Steffens, G.S., and Craig, P.A., 1998, Classification, lithologic calibration, and stratigraphic succession of seismic facies of intraslope basins, deep-water Gulf of Mexico: *American Association of Petroleum Geologists Bulletin, v. 82*, p. 701-728.

Pratson. L.F., and Ryan, W.B.F., 1994, Pliocene to Recent infilling and subsidence of intraslope basins offshore Louisiana: *American Association of Petroleum Geologists Bulletin, v. 78*, p. 1483-1506.

Rothwell, R.G., Kenyon, N.H., and McGregor, B.A., 1991, Sedimentary features of the south Texas continental slope as revealed by side-scan sonar and high-resolution seismic data: *American Association of Petroleum Geologists Bulletin, v. 75*, p. 298-312.

Sager, W.W., and MacDonald, I.R., and Hou, R., 2004; Side-scan sonar imaging of hydrocarbon seeps on the Louisiana continental slope: *American Association of Petroleum Geologists Bulletin, v. 88*, p. 725-746.

Salvador, A., 1991a, Triassic-Jurassic: *in* Salvador, A. (Editor), The Geology of North America, Vol. J., The Gulf of Mexico Basin, Geological Society of America, Boulder, CO, p. 131-180.

Salvador, A., 1991b, Origin and development of the Gulf of Mexico basin: *in* Salvador, A. (Editor), The Geology of North America, Vol. J., The Gulf of Mexico Basin, Geological Society of America, Boulder, CO, p. 389-444.

Sawyer, D.S., Buffler, R.T., and Pilger, R.H., 1991, The crust under the Gulf of Mexico basin, *in* Salvador, A. (Editor), The Geology of North America, Vol. J, Gulf of Mexico Basin: Geological Society of America, Boulder, CO, p. 53-72.

Schlager, W., Buffler, R.T., and Scientific Party of DSDP Leg 77, 1984, DSDP Leg 77; Early history of the Gulf of Mexico: *Geological Society of America Bulletin, v. 95*, p. 226-236.

Schwab, W.C., Lee, H.J., Twichell, D.C., Locat, J., Nelson, C.H., McArthur, W.G., and Kenyon, N.H., 1996, Sediment mass-flow processes on a depositional lobe, outer Mississippi Fan: *Journal of Sedimentary Research, v. 66*, p. 916-927.

Silva, A.J., Baxter, C.D.P., LaRosa, P.T., and Bryant, W.R., 2004, Investigation of mass wasting on the continental slope and rise: *Marine Geology, v. 203*, p. 355-366.

Sohl, N., Martinez, E., Salmeron-Urena, P., and Soto-Jaramillo, F., 1991, Upper Cretaceous, *in* Salvador, A. (Editor), The Geology of North America, Vol. J., The Gulf of Mexico Basin, Geological Society of America, Boulder, CO, p. 205-244.

Tripsanas, E.K., Bryant, W.R., and Phaneuf, B.A., 2004a, Slope-instability processes caused by salt movements in a complex deep-water environment, Bryant Canyon area, northwest Gulf of Mexico: *American Association of Petroleum Geologists Bulletin, v. 88*, p. 801-824.

Tripsanas, E.K., Bryant, W.R., and Phaneuf, B.A., 2004b, Depositional processes of uniform mud deposits (unifites), Hedberg Basin, northwest Gulf of Mexico: New perspectives: *American Association of Petroleum Geologists Bulletin, v. 88*, p. 825-840.

Twichell, D.C., and Cooper, A.K., 2000, Relation between sea floor failures and gas hydrates in the Gulf of Mexico; a regional comparison: *American Association of Petroleum Geologists Annual Convention, v. 9*, p. A150.

Twichell, D.C., Cross, V.A., Paskevich, V.F., Hutchinson, D.R., Winters, W.J., and Hart, P.E., 2005, GIS of selected geophysical and core data in the northern Gulf of Mexico continental slope collected by the U.S. Geological Survey: U.S. Geological Survey Open-File Report 2005-1071, 1 DVD-ROM.

Twichell, D.C., Dillon, W.P., Paull, C.K., and Kenyon, N.H., 1996, Morphology of carbonate escarpments as an indicator of erosional processes, *in* Gardner, J. V. Field, M.E., and Twichell, D.C. (Editors), Geology of the United States' Seafloor: The view from GLORIA, Cambridge University Press, p. 97-107.

Twichell, D.C., Nelson, C.H., and Damuth, J.E., 2000, Late-stage development of the Bryant Canyon turbidite pathway on the Louisiana continental slope, in Weimer, P., Slatt, R.M., Coleman, J., Rosen, N.C., Nelson, H., Bouma, A.H., Styzen, M.J., and Lawrence, D.T. (Editors), Deep-Water Reservoirs of the World: Proceedings of the Gulf Coast Section SEPM, p. 1032-1044, CD-ROM.

Twichell, D.C., Nelson, C.H., Kenyon, N. and Schwab, W., 2009, The influence of external processes on the Holocene evolution of the Mississippi Fan, *in,* Kneller, B., McCaffrey, W., Martinsen, O., and Posamentier, H. (Editors), External Controls on Deep Water Depositional Systems: Climate, sea-level, and Sediment Flux, SEPM Special Publication no. 92, p. 145-157.

Twichell, D.C., Parson, L.M., and Paull, C.K., 1990, Variations in the styles of erosion along the Florida Escarpment, eastern Gulf of Mexico: *Marine and Petroleum Geology, v. 7*, p. 253-266.

Twichell, D.C., Schwab, W.C., Nelson, C.H., Lee, H.J., and Kenyon, N.H., 1992, Characteristics of a sandy depositional lobe on the outer Mississippi Fan from SeaMARC IA sidescan sonar images: *Geology, v. 20*, p. 689-692.

Twichell, D.C., Valentine, P.C., and Parson, L.M., 1993, Slope failure of carbonate sediment on the West Florida Slope, *in*, Schwab, W.C., Lee, H.J., and Twichell, D.C. (Editors), Submarine landslides: Selected studies in the U.S. Exclusive Economic Zone, U. S. Geological Survey Bulletin 2002, p. 69-78.

Walker, J.R., and Massingill, J.V., 1970, Slump features on the Mississippi Fan, northeastern Gulf of Mexico: *Geological Society of America Bulletin, v. 81*, p. 3101-3108.

Weimer, P. and Dixon, B.T., 1994, Regional sequence stratigraphic setting of the Mississippi Fan complex, northern deep Gulf of Mexico: Implications for evolution of the northern Gulf basin margin, *in* Weimer, P., Bouma, A.H., and Perkins, B.F. (Editors), Submarine fans and turbidite systems: Sequence stratigraphy, reservoir architecture and production characteristics, GCSEPM Foundation 15th Annual Research Conference, p. 373-381.

Weimer, P., 1989, Sequence stratigraphy of the Mississippi Fan (Plio-Pleistocene), Gulf of Mexico: *Geo-Marine Letters, v. 9*, p. 185-272.

Weimer, P., 1991, Seismic facies, characteristics, and variations in channel evolution, Mississippi Fan (Plio-Pleistocene), Gulf of Mexico, *in* Weimer, P., and Link, M.H. (Editors), Seismic Facies and Sedimentary Processes of Submarine Fans and Turbidite Systems, Springer-Verlag, New York, p. 323-347.

Worzel, J.L., Leyden, R., and Ewing, M., 1968, Newly discovered diapirs in the Gulf of Mexico: *American Association of Petroleum Geologists Bulletin, v. 52*, p. 1194-1203.

Chapter 2: Timing of Occurrence of Large Submarine Landslides

Temporal Variations of Failure Conditions

Just as some areas of the seafloor are more prone to failure than others, the environmental conditions that cause landslides of this nature are also not uniformly distributed with geologic time. There are most likely some time periods when the probability of failure is greater, and some periods when the probability is less. If we can evaluate when these periods occur, we can either reduce or increase our estimate of the likelihood of landslide tsunamis for the present period in geologic history.

One of challenges in understanding landslide processes is accurately dating when they occurred. Accurate dates are needed to understand the role that changes in sea level, climate, sediment supply, tectonics, and other environmental conditions played in triggering landslides. This information is needed to determine whether conditions when the landslides occurred were similar to or dramatically different from present-day conditions. There are no landslides in the Gulf of Mexico that have been dated accurately enough to determine under what environmental or temporal conditions they occurred. Because of this lack of information in the Gulf of Mexico, we present a regional synthesis of available data on the timing of landslides in the North Atlantic and other parts of the world to provide a background on the importance of this issue.

Many temporally varying factors influence submarine slope stability. These include the following:

(1) Quantities and types of sediment delivered to the margins. As the quantity of sediment delivered increases, the likelihood of formation of thick, potentially unstable sedimentary deposits also increases. The influence of sediment type is less clear. Sandy sediment is more vulnerable to failure during cyclic loading events but fine-grained sediment, if deposited rapidly, can form weak, gassy, pore-water pressure-charged material. During glacial periods, the input of sediment to the continental margins generally increases, particularly near the edges of continental ice sheets

(2) Locations of depocenters; particularly slope vs. shelf. Thick, relatively weak sediment deposits on the continental slope clearly have a greater potential for producing open-slope failures than similar deposits on the shelf. Likewise, during glacial periods, when sea level is lowered to near the shelf break, the likelihood of deposition on the slope increases (formation of shelf-edge deltas) vs. interglacial periods when river deltas are commonly located on the shelf. Catastrophic drainage

of glacial lakes (Uchupi *et al.*, 2001) can also occur during glacial periods and can bring large quantities of sediment to the outer shelf and continental slope. According to Uchupi *et al.* (2001) such floods can trigger gravity flows on the upper slope and carry coarse debris into the deep sea.

(3) Changes in seafloor pressures and temperatures, which can influence hydrate stability and the possible generation of free gas (Kayen and Lee, 1992). Changes in sea level alter hydrostatic pressures on the seafloor and can cause destablilization of gas hydrates contained within some bottom sediment. Global oceanic temperature changes and redirection of warm and cold currents can have a similar effect. When gas hydrate is destabilized, it can release free gas, increase pore-water pressure, and reduce sediment strength. Critical times in geologic history include sea-level falls during the onset of continental glaciation, the beginning and end of glacial cycles when the locations of major currents, such as the Gulf Stream, change their course and other periods of extensive environmental change.

(4) Variations in seismicity related to isostatic loading or unloading of coastal and near-coastal regions by ice (or to a lesser extent by large sea level changes) (Bungum *et al.*, 2005). The formation and melting of thick sheets of ice produce large changes in crustal stresses. Particularly in areas near the margins of ice sheets, the crust may respond to strong induced stress gradients by internal failure and the generation of earthquakes that are larger than would generally be expected for these areas. Crustal stress changes related to ice loading and sea-level changes may also play a role in the frequency of island and coastal volcanism (McGuire *et al.*, 1997). Variations in volcanism could lead to variations in volcanic island collapses.

(5) Changes in groundwater flow conditions within the continental slope and shelf (Dugan and Fleming, 2000). Some sediment beds within continental margins can become pressurized for a variety of reasons, including flow from higher elevations, tectonic activity, direct loading by ice and gas reservoirs. Pressure gradients in these beds induce groundwater flow, commonly from the continents into the offshore. Sea-level changes during the waxing and waning of ice sheets alter these conditions and rates of flow. This in turn alters the pore water pressure regime within the slope and can, under some conditions, contribute to slope failure.

Although all of the above conditions can occur on a small scale, because of local effects (*e.g.*, river course changes, tectonic activity, opening and closing of straits, etc.), the dominant factor that can influence the times of occurrence of significant submarine landslides is glaciation. Pleistocene glacial and interglacial cycles include several phases (see Figure 2-1 for a conceptual diagram of these effects) that can cause or impede the development of large submarine landslides:

(1) Initiation of glaciation. With the onset of a glacial cycle, large, thick ice sheets form over high latitude continental areas. The resulting impoundment of water causes sea level to fall worldwide in the range of 100 m, and the fronts of the ice sheets advance toward the coast. The ice erodes large quantities of geologic material, and meltwater from the front of the ice sheets increases in flow rate and sediment concentration. Deposits of rapidly accumulating sediment form near the shelf break and these increase in thickness with time. With sea level lowered, a result is the development of more extensive and potentially more unstable shelf-edge deltas, even in areas far removed from continental ice sheets. Shifting the weight of large amounts of water

from the ocean to land changes crustal stresses and can create an environment of increased seismicity, particularly near the edges of the ice sheets where the stress gradients are highest.

(2) Most of these effects increase the likelihood of submarine slope failure. Lowering sea level immediately decreases seafloor pressure and this can lead to gas-hydrate dissociation and the development of high excess pore-water pressures in some places. The resulting decreased shear strength can lead to failure. Increased seismicity can load continental slope sediment bodies and also potentially cause them to fail. The development of thick sediment bodies near the shelf break, including shelf-edge deltas, can also increase the risk of failure. However, sediment thickness continues to increase throughout a glacial cycle and to progressively increase the risk of failure. Groundwater flow conditions can change. Certainly the head difference between groundwater levels in near coastal highlands and the ocean is increased, owing to sea-level fall. In the absence of other changes, this can reduce stability.

(3) Full glaciation. After the ice sheets have reached their maximum extent, seismicity at the margins may begin to decline and the tendency toward hydrate dissociation will be reduced. Both of these factors will, in themselves, lead to reduced slope instability. However, rapidly deposited sediment bodies will continue to form on the slope and as they become thicker the tendency towards excess pore-water pressure development will actually increase. Likewise, enhanced groundwater flow and resulting elevated pore-water pressures may also continue. The net effect of all of these factors is unclear. Almost certainly the likelihood of slope instability is greater during full glaciation than during interglacial times although it may well be less than during the transition period between interglacials and glacials.

(4) Transition from glacial to interglacial time. As continental ice sheets melt and sea levels rise, increased seismicity near the margins of areas that were heavily glaciated will begin to occur as a result of isostatic readjustment. Shelf-edge deltas will be near their maximum extent and may have pore-water pressures that are near their greatest values owing to long periods of rapid deposition during the glacial period. Major current systems such as the Gulf Stream may readjust, bringing warmer water to areas like northern Europe and possibly altering the stability of gas hydrates. This effect, of course, is countered by larger seafloor pressures produced by greater water depths on the slope. Groundwater flow may be slowed owing to higher sea levels, and new deposition will tend to occur more commonly on the shelf than on the slope. The net effect of these changes is not immediately obvious, although, as will be seen below, the geologic record shows many large submarine landslides occurring in the early Holocene.

(5) Interglacial time. After sea level has risen, seismicity near the margins of the former ice sheets will slowly decline. Unstable shelf edge deltas formed during the glacial period will either already have failed or will become gradually less likely to fail. Enhanced stability occurs because of a lack of new sediment and the dissipation of excess pore-water pressures produced during rapid deposition. Conditions of hydrate stability will become less variable and elevated pore-water pressures related to groundwater flow will decline. The period well after the end of a glacial cycle is most likely one in which the likelihood of submarine slope failure is lowest, except on deltas of large rivers that have prograded across the shelf, *e.g.*, the Mississippi River Delta.

Modeling

Hutton and Syvitski (2004) report on numerical modeling of the role of sediment failure in the development of continental margins. The authors use the *SedFlux* model (Syvitski and Hutton, 2001) to simulate the lithologic character of basin stratigraphy through the use of a series of process-based event modules to distribute sediment through surface or subsurface plumes, ocean storm events, slope failures, turbidity currents or debris flows. The model can change accommodation space (space available for sediment deposition) as a result of subsidence, tectonics or compaction. The model produces distributions of grain size, bulk density, porosity and permenability.

Hutton and Syvitski (2004) applied the model to a representative 2-D continental margin and allowed the margin to develop over a period of one million years, incorporating many glacial and sea level cycles. The authors related the modeled sedimentologic properties to geotechnical properties and used the results to predict how earthquake-loading influenced slope stability of the margin as a function of time over this large time span. The model simulates many of the factors thought to be important in continental margin stability and allows an additional check on the role of glacial cycles in affecting margin stability. The results show a strong association between slope stability and sea-level stand. Although failures were modeled to occur at any sea-level position, depending on the prior depositional history, many more (by a factor of 3-5) occur during periods of falling or low sea level than during comparable periods of rising or high sea level. The largest number of failures was modeled to occur during falling sea level. The model showed that most of the failures are located on the upper continental slope in 500±250 m water depth. The model also showed that most of the failures have a thickness less than 10 m although some can exceed 30 m. The thickness of sediment failure increases during periods of rising or high sea level.

Findings and Conclusions

Table 2-1 summarizes the ages of submarine landslides reviewed in this chapter (including failures in both the Atlantic Ocean and elsewhere but excluding those from the last 100 years), and these results are plotted in Figure 2-2. Also provided in the table is a brief description of the bases used for making age estimates. As can be seen, many different age estimate strategies have been applied, and the reliability of the estimates varies greatly. Conclusions drawn from these results must be considered as tentative. If these ages are binned in groups of 5,000 years for the last 20,000 years (using the mean age for landslides that show a range of possible ages), we find the following: two slides in the last 5,000 years, five from 5 to 9.9 ka, four from 10 to 14.9 ka, and five from 15 to 19.9 ka. Using 10,000 years ago as a crude approximation for the end of the last glacial cycle and 20,000 year ago as a crude approximation for the last glacial peak, these results imply that the occurrence of large landslides was roughly evenly distributed with time from the last glacial maximum until about 5,000 years after the end of glaciation. In the past 5,000 years the occurrence of submarine landslides has been less frequent. Note that the last 100 years were excluded because landslide-tsunamis are now directly observed and these observations lead us to conduct surveys and find landslides. Some, perhaps most, of the very recent tsunamigenic landslides would not have been seen if we had not known where to look. However, possibly the Grand Banks event, which laid down a 1-m-thick turbidite layer over large parts off the Sohm Abyssal Plain (Heezen *et al.*, 1954), would still have been observed even if observers

had not been available to experience the earthquake, tsunami, and cable breaks. If so, then we can increase the apparent number of large landslides of the last 5,000 years from two to three. We could then conclude that ratio of landslide occurrence during and shortly after glacial cycles to landslide occurrence well into an interglacial period is about 5:3.

These observations regarding large landslides are supported by other data. For example, as discussed above, Piper *et al.* (2003) show that glacial periods produce about 3.5 times as many submarine landslides on the Canadian margin as do non-glacial periods. Likewise, Lebreiro *et al.* (1997) estimate that there were about 2.7 times as many turbidity currents during glacial periods off the coast of central Europe. Although at least part of the reason for reduced turbidity current activity during interglacial periods is that some canyon heads become stranded at the shelf break, an association is still likely between turbidity-current deposits on deep-sea fans and abyssal plains and submarine-slope failures on the slope and within canyons. In summary, all these field results appear to indicate an increase in the frequency of large landslides by about a factor of 1.7 to 3.5 during and shortly after glacial periods, relative to times well after glaciation.

Model results (Hutton and Syvitski, 2004) support the idea that significantly more submarine landslides occur during falling or lowered sea level than during rising or high sea level. The model, in fact, suggests that occurrences are 3 to 5 times more likely under falling or lowered conditions, with the greatest number corresponding to the time when sea level is falling.

A plausible explanation for field observations that many more landslides occur during and shortly after glacial periods is that during glacial periods and the associated lowstands of sea level, thick deposits of sediment form readily on the upper continental slope, often in shelf-edge deltas. When glaciation ends, seismicity is increased near previously glaciated areas, serving as a trigger for causing these thick slope deposits to fail. Even in regions that were not glaciated, relatively thick, potentially weak deposits may have been preferentially deposited on the upper slope. These deposits might be more susceptible to failure during glacial cycles or shortly thereafter than similar slopes at times farther into an interglacial cycle (after most of the potentially unstable slopes have failed, probably during large earthquakes).

The role of hydrate dissociation in the initiation of submarine landslides has been discussed extensively in the literature (*e.g.*, Maslin *et al.*, 2004, Paull *et al.*, 1996, Kayen and Lee, 1992) but there are few definitive studies that show that this process indeed caused a landslide. One problem is that most of the landslides reported are from the last 20,000 years, which is a period of mostly stable or rising sea level, a time when significant hydrate dissociation might not be expected. Also, the relatively poor accuracy of landslide dates makes it difficult to associate failure events with relatively short periods of sea level fall (Maslin *et al.*, 2004). Large landslides such as the Storegga slide were at one point thought of as possibly having been caused by hydrate dissociation but more recent studies appear to show that hydrates were not a major factor in causing failure (Bryn *et al.*, 2005).

Clearly, not all tsunamigenic landslides involve failures of sediment deposits that were emplaced on the slope during lowstands or were failures triggered by isostatic-rebound related seismicity. Collapses of volcanic islands and other mechanisms for steepening slopes, such as the salt tectonics associated with the Cape Fear slide and some failures in the Gulf of Mexico, may be less influenced by glacial stands, although even for these cases, crustal stress changes associated with sea level change may play a role (McGuire *et al.*, 1997).

In summary, a risk of tsunamigenic submarine landslides exists off the continental margin during intergracial periods. However, the probability of occurrence is less during the present interglacial period, perhaps by a factor of 1.7 to 3.5. Most likely areas where future

tsunamigenic landslides could occur include volcanic islands (which are possibly too distant to have a significant impact on the Gulf Coast), within salt tectonics areas in the Gulf of Mexico, and off large deltas that reach the shelf edge, such as the Mississippi Delta.

Table

Table 2-1: Distribution of ages of several large submarine landslides. Non-Atlantic Ocean landslides are in italics.

Name of landslide	Age in 1000's of years	References	Basis for age determination
Sur slide	*1.5-6*	*Normark and Gutmacher (1988)*	*Sediment thickness and published deposition rates from nearby cores.*
Traenadjupet	4	Laberg *et al.*, 2002	^{14}C with a reservoir age of 440 yrs; calibrated using CALIB 4.0
Afen	5.8	Wilson *et al.*, 2004	AMS ^{14}C and biostratigraphy
Storegga	8.1	Haflidason *et al.*, 2005	^{14}C with a reservoir age of 400 yrs
Palos Verdes	*7.5*	*Normark et al., 2004*	^{14}C with a reservoir age of 800 yrs; calibrated using CALIB 4.3
Goleta west	*8*	*Fisher et al., 2005*	*Stratigraphic correlation with ODP 893; ^{14}C dating of ODP samples, corrected to calendar years using methods of Ingram and Kennett (1995)*
Faeroe	9.9	Van Weering *et al.*, 1998	^{14}C with a reservoir correction
Goleta middle lobe	*10*	*Fisher et al., 2005*	*Stratigraphic correlation with ODP 893; ^{14}C dating of ODP samples, corrected to calendar years using methods of Ingram and Kennett (1995)*
Peach	10.5	Holmes *et al.*, 1998; Maslin *et al.*, 2004	Regional stratigraphy based on dated cores and borings
BIG'95	*11.4*	*Canals et al., 2004; Lastras et al., 2004*	^{14}C with a reservoir age of 402 yrs; calibrated using CALIB 3.0
Cape Fear	8-14.5	Embley, 1980; Poponoe *et al.*, 1993; Paull *et al.*, 1996; Rodriguez and Paull, 2000	Recently obtained dates (Rodriguez and Paull, 2000; Paull *et al.*, 1996) are uncalibrated ^{14}C
Amazon Shallow East	14-17	Maslin *et al.*, 1998	Radiocarbon dating and oxygen isotope correlation with Leg 155 sediment and piston cores. Radiocarbon years corrected to calendar years.
Amazon Shallow West	14-17	Maslin *et al.*, 1998	Radiocarbon dating and oxygen isotope correlation with Leg 155 sediment and piston cores. Radiocarbon years corrected to calendar years.
Rockall	15-16	Flood *et al.*, 1979	Carbonate and cocccolith stratigraphy
Canary	15	Masson , 1996	Calibrated ^{14}C dating of turbidites; K/Ar dating of volcanic events
Nyk	16.3	Lindberg *et al.*, 2004	^{14}C with a reservoir age of 440 yrs
Amazon Deep Eastern	35	Maslin *et al.*, 1998	Biostratigraphy, seismic stratigraphy, magneto-stratigraphy, and sedimentation rate constraints
Currituck	25-50	Prior *et al.*, 1986	Sediment thickness and published deposition rates from nearby cores
Amazon Deep Western	42-45	Maslin *et al.*, 1998	Biostratigraphy, seismic stratigraphy, magneto-stratigraphy, and sedimentation rate constraints
Saharan	60	Gee *et al.*, 1999	Coccolith assemblage analysis using the method of Weaver (2000)

Figures

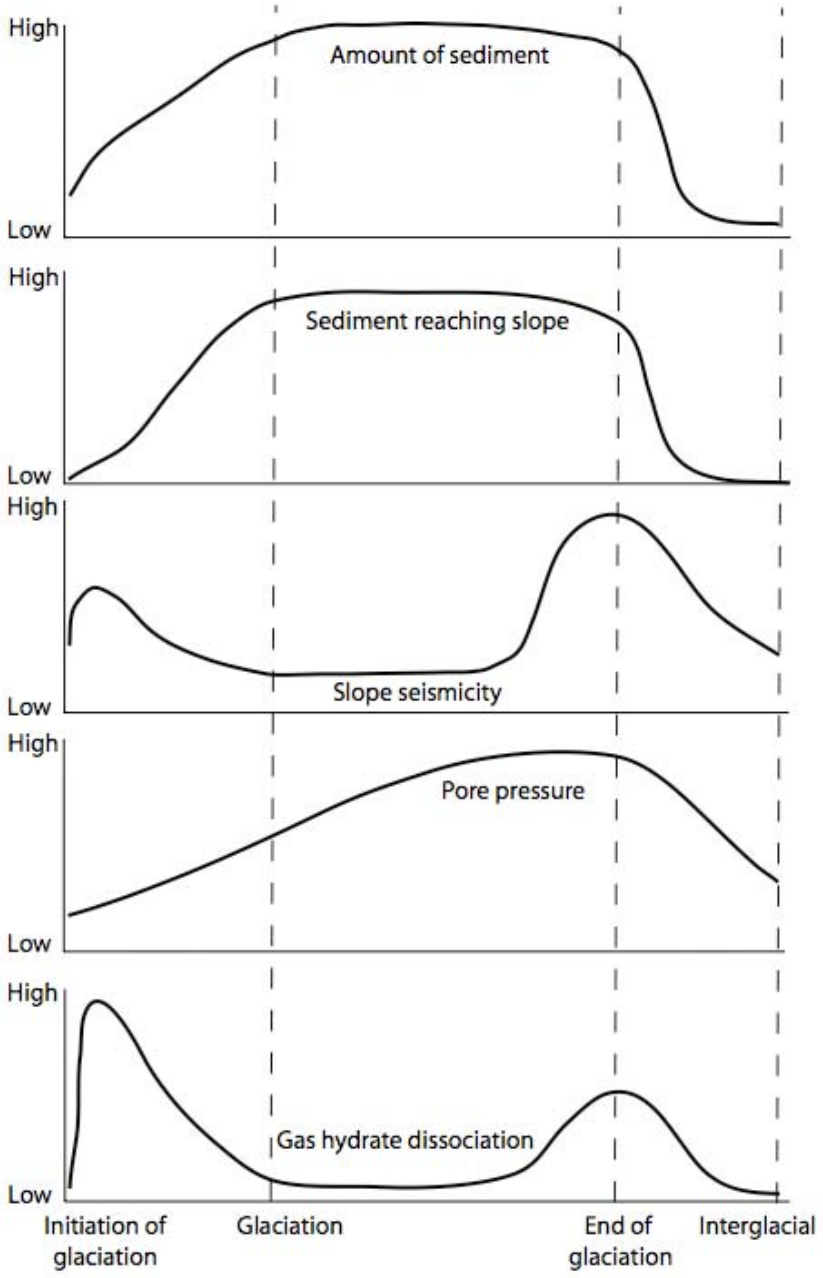

Figure 2-1: Approximate impact of time on several factors that impact the stability of submarine slopes.

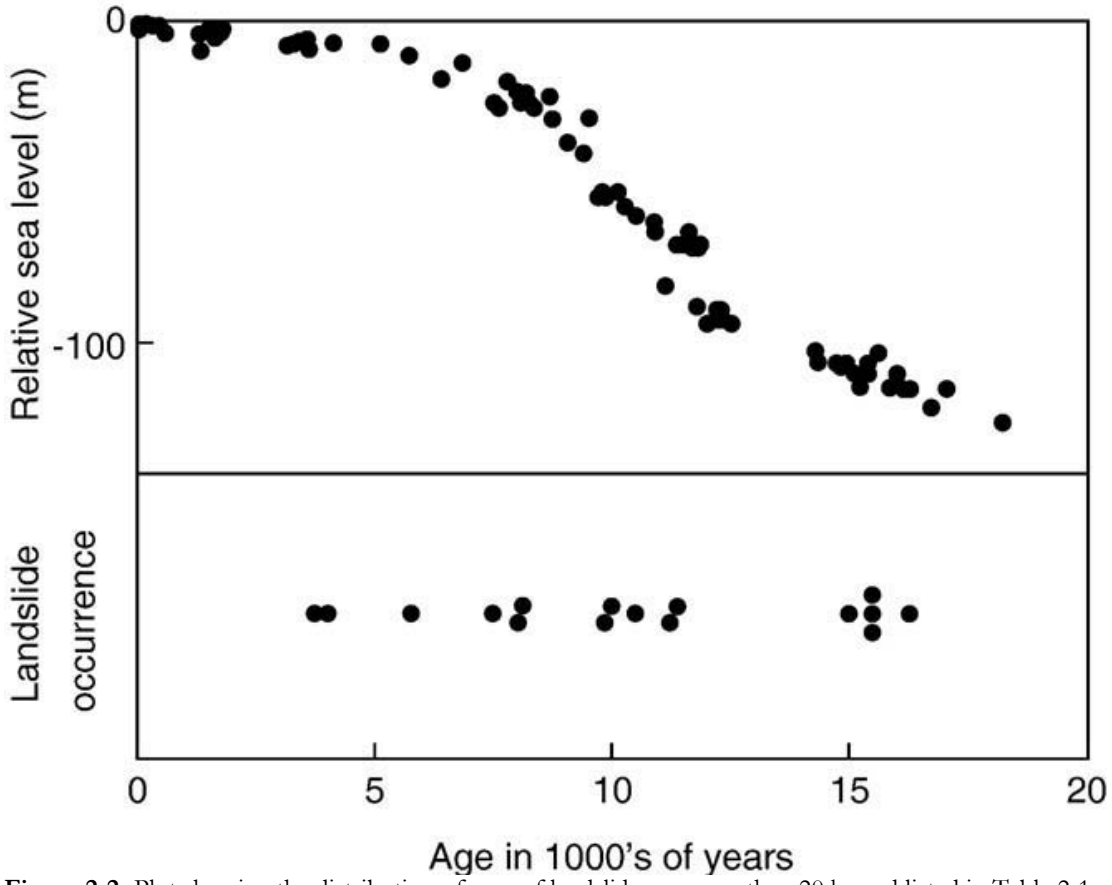

Figure 2-2: Plot showing the distribution of ages of landslides younger than 20 ky and listed in Table 2-1. For comparison with glacial cycles, sea level versus time (according to corrected 14C dating of samples from Barbados and elsewhere; Fairbanks, 1992) are also plotted. The figures shows a reduced occurrence of landslides during the last 5 ky, an interglacial time with elevated sea level.

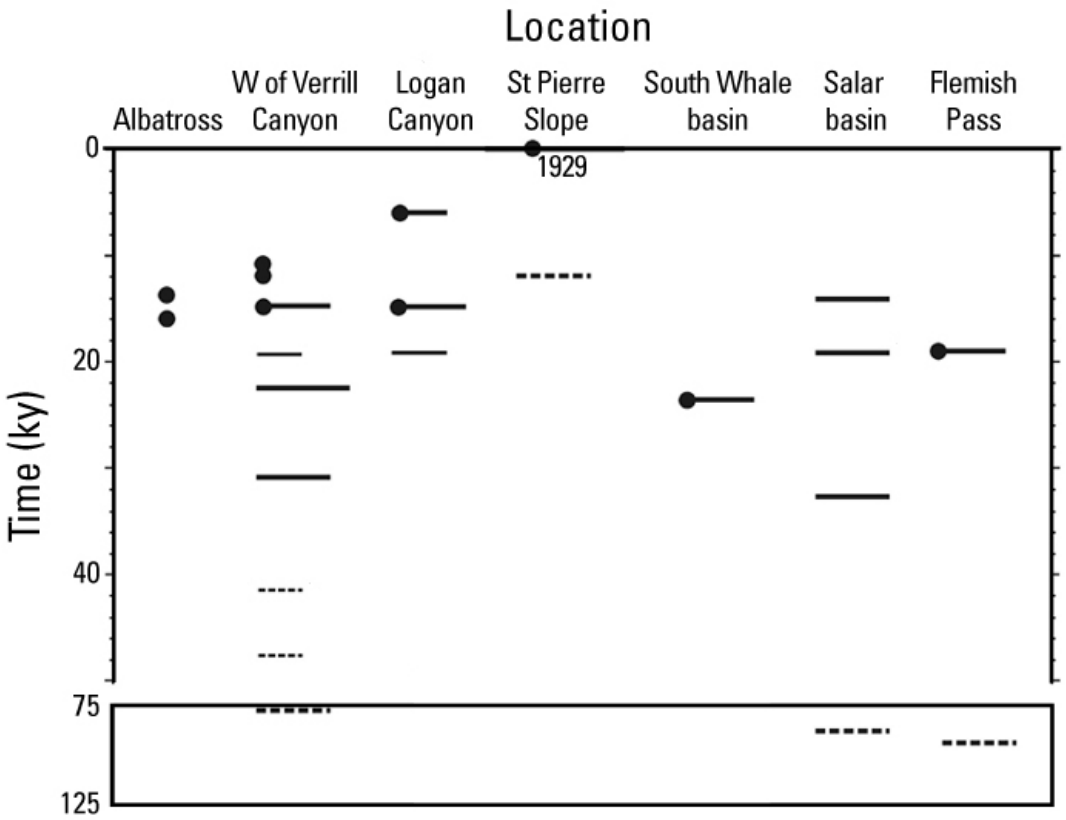

Figure 2-3: Occurrence of submarine landslides off eastern Canada by time and general location (after Piper et al., 2003). Dots indicate direct dates of unconformities or failure deposits in a core. Solid lines indicate chronology established using sparker profiles and a set of key reflectors that have been dated back to 36 ka. Dashed lines represent an extrapolation of this sparker reflector chronology to older ages (Mosher et al., 2004).

References

Booth, J.S., O'Leary, D.W., Popenoe, P., and Danforth, W.W., 1993, U.S. Atlantic continental slope landslides: their distribution, general attributes, and implications, *in* Schwab, W.C., Lee, H.J., and Twichell, D.C. (Editors), Submarine landslides: Selected studies in the U.S. EEZ: USGS Bulletin 2002, p.14-22.

Bryn, P., Berg, K., Forsberg, C.F., Solheim, A., and Kvalstad, T.J., 2005, Explaining the Storegga slide: *Marine and Petroleum Geology*, *v. 22*, p. 11-19.

Bungum, H., Lindholm, C. and Faleide, J.I., 2005, Postglacial seismicity offshore mid-Norway with emphasis on spatio-temporal-magnitudal variations: *Marine and Petroleum Geology*, *v. 22*, p. 137/148.

Canals, M., Lastras, G., Urgeles, R., Casamor, J.L., Mienert, J., Cattaneo, A., De Batist, M., Haflidason, H., Imbo, Y., Laberg, J.S., Locat, J., Long, D., Longva, O., Masson, D.G., Sultan, N., Trincardi, F., and Bryn, P., 2004, Slope failure dynamics and impacts from seafloor and shallow sub-seafloor geophysical data: case studies from the COSTA project: *Marine Geology*, *v. 213*, p. 9-72.

Dugan, B. and Flemings, P.B., 2000, Overpressure and fluid flow in the New Jersey continental slope: implications for slope failure and cold seeps: *Science*, *v. 289*, p. 288-291.

Edgers, L., and Karlsrud, K., 1982, Soil flows generated by submarine slides: case studies and consequences, *in* Chryssostomomidis, C. and Connor, J.J (Editors), Proceedings of the 3rd International Conference on the Behavior of Offshore Structures, Hemisphere Publishing Corporation, volume 2, p. 425-437.

Embley, R.W., 1980, The role of mass transport in the distribution and character of deep-ocean sediments with special reference to the North Atlantic: *Marine Geology*, *v. 38*, p. 23-50.

Fairbanks, R., 1992, Barbados sea level and Th/U 14C calibrations: IGBP Pages/World Data Center for Paleoclimatology Data Contribution Series #92-020.

Fisher, M.A., Normark, W.R., Greene, H.G., Lee, H.J., and Sliter, R.W., 2005, Geology and tsunamigenic potential of submarine landslides in Santa Barbara Channel, southern California: *Marine Geology*, *v. 224*, p. 1-22.

Flood, R.D., Hollister, C.D., and Lonsdale, P., 1979, Disruption of the Feni sediment drift by debris flows from Rockall Bank: *Marine Geology*, *v. 32*, p. 311-334.

Gee, M.J.R., Masson, D.G., Watts, A.B. and Allen, P.A., 1999, The Saharan debris flow: an insight into the mechanics of long runout submarine debris flows: *Sedimentology*, *v. 46*, p. 317-335.

Haflidason, H., Lien, R., Sejrup, H.P., Forsberg, C.F., and Bryn, P., 2005, The dating and morphometry of the Storegga slide: *Marine and Petroleum Geology*, *v. 22*. p. 123-136.

Hampton, M.A., Lee, H.J., and Locat, J., 1996, Submarine landslides: *Reviews of Geophysics*, *v. 34*, p. 33-59.

Heezen, B.C., Ericsson, D.B., Ewing, M., 1954, Further evidence of a turbidity current following the 1929 Grand Banks earthquake: *Deep Sea Research*, *v. 1*, p. 193-202.

Holmes, R., Long, D., and Doded, L.R., 1998, Large-scale debrities and submarine landslides on the Barra Fan, west of Britain, *in* Stoker, M.S., Evans, D. and Cramp, A. (Editors), Geological Processes on Continental Margins: Sedimentation, Mass-Wasting and Stability: *Geological Society, London, Special Publications*, *v. 129*, p. 67-79.

Hutton, E.W.H. and Syvitski, J.P.M., 2004, Advances in the numerical modeling of sediment failure during the development of a continental margin: *Marine Geology*, *v. 203*, p. 367-380.

Ingram, B.L. and Kennett, J.P., 1995, Radiocarbon chronology and planktonic-benthic foraminiferal ^{14}C age differences in Santa Barbara Basin sediments, Hole 893A, *in* Kennett, L.P., Baldauf, J.G., and Lyle, M. (Editors), Proceedings of the Ocean Drilling Program, Scientific Results 146 (Pt. 2), p. 19-27.

Kayen, R.E. and Lee, H.J., 1992. Pleistocene slope instability of gas hydrate-laden sediment on the Beaufort Sea margin, *in* Lee, H.J. (Editor), Special Issue on Marine Slope Stability: *Marine Geotechnology*, *v. 10*, p. 125-142.

Laberg, J.S., Vorren, T.O., Mienert, J., Evans, D., Lindberg, B., Ottesen, D., Kenyon, N.H., and Henriksen, S., 2002, Late Quaternary palaeoenvironment and chronology in the Traenadjupet slide area offshore Norway: *Marine Geology*, *v. 188*, p. 35-60.

Lastras, G., Canals, M., Urgeles, R., de Batist, M., Calafat, A.M. and Casamor, J.L., 2004, Characterisation of the recent BIG'95 debris flow deposit on the Ebro margin, Western Mediterranean Sea, after a variety of seismic reflection data, *Marine Geology*, *v. 213*, p. 235-255.

Lebreiro, S.M., McCave, N.I., and Weaver, P.P.E., 1997, Late Quaternary turbidite emplacement on the Horseshoe abyssal plain (Iberian Margin): *Journal of Sedimentary Research*, *v. 67*, p. 856-870.

Lindberg, B., Laberg, J.S. and Vorren, T.O., 2004, The Nyk Slide—morphology, progression, and age of a partly buried submarine slide offshore northern Norway: *Marine Geology*, *v. 213*, p. 277-289.

Maslin, M., Mikkelsen, N., Vilela, C., and Haq, B., 1998, Sea-level and gas-hydrate-controlled catastrophic sediment failures of the Amazon Fan: *Geology*, *v. 26*, p. 1107-1110.

Maslin, M., Owen, M., Day, S. and Long, D., 2004, Linking continental-slope failures and climate change: testing the clathrate gun hypothesis: *Geology*, *v. 32*, p. 53-56.

Masson, D.G., 1996, Catastropic collapse of the volcanic island of Hierro 15 ka ago and the history of landslides in the Canary Islands: *Geology*, *v. 24*, p. 231-234.

McGuire, W.J., Howarth, R.J., Firth, C.R., Solow, A.R., Pullen, A.D., Saunders, S.J., Stewart, I.S. and Vita-Finzi, C., 1997, Correlation between rate of sea-level change and frequency of explosive volcanism in the Mediterranean: *Nature*, *v. 389*, p. 473-476.

Mosher, D.C., Piper, D.J.W., Campbell, D.C. and Jenner, K.A., 2004, Near-surface geology and sediment-failure geohazards of the central Scotian Slope: *AAPG Bulletin*, *v. 88*, p. 703-723.

Normark, W.R. and Gutmacher, C.E., 1988, Sur submarine slide, Monterey Fan, central California: *Sedimentology*, *v. 35*, p. 629-647.

Normark, W.R., McGann, M. and Sliter, R.W., 2004, Age of Palos Verdes submarine debris avalanche, southern California: *Marine Geology*, *v. 203*, p. 247-259.

Paull, C.K., Buelow, W.J., Ussler, W., III, and Borowski, W.S., 1996, Increased continental-margin slumping frequency during sea-level lowstands above gas hydrate-bearing sediments: *Geology*, *v. 24*, p. 143-146.

Piper, D.J.W., Mosher, D.C., Gauley, B.-J., Jenner, K., and Campbell, D.C., 2003, The chronology and recurrence of submarine mass movements on the continental slope off southeastern Canada, *in* Locat, J., and Mienert (Editors), Submarine Mass Movements and their Consequences: Kluwer Academic Publishers, The Netherlands, p. 299-306.

Popenoe, P., Schmuck, E.A., and Dillon, W.P., 1993, The Cape Fear landslide: slope failure associated with salt diapirism and gas hydrate decomposition, *in* Schwab. W.C., Lee, H.J., and Twichell, D.C. (Editors), Submarine Landslides: Selected Studies in the U.S. EEZ: USGS Bulletin 2002, p. 40-53.

Prior, D.B., Doyle, E.H., and Neurauter, T., 1986, The Currituck slide, mid-Atlantic continental slope-revisited: *Marine Geology*, *v. 73*. p. 25-45.

Rodriguez, N.M. and Paull, C.K., 2000, Data Report: ^{14}C dating of sediment of the uppermost Cape Fear slide plain: constraints on the timing of this massive submarine landslide, *in* Paull, C.K., Matsumoto, R., Wallace, P.J., and Dillon, W.P. (Editors), Proceedings of the Ocean Drilling Program, Scientific Results, volume 164, p. 325-327.

Syvitski, J.P.M., and Hutton, E.W.H., 2001, SEDFLUX 1.0C: An advanced process-response numerical model for the fill of marine sedimentary basins, *Computers and Geosciences*, *v. 27*, p. 731-754.

Uchupi, E., Driscoll, N., Ballard, R.D. and Bolmer, S.T., 2001, Drainage of late Wisconsin glacial lakes and the morphology and late quaternary stratigraphy of the New Jersey—southern New England continental shelf and slope: *Marine Geology*, *v. 172*, p. 117-145.

Van Weering, T., Nielsen, T., Kenyon, N.H., Akentieva, K., and Kulipers, A.H., 1998, Large submarine slides on the NE Faeroe continental margin, *in* Stoker, M.S., Evans, D. and Cramp, A. (Editors), Geological Processes on Continental Margins: Sedimentation, Mass-Wasting and Stability: *Geological Society, London, Special Publications*, *v. 129*, p. 5-17.

Weaver, P.K., Wynn, R.B., Kenyon, N.H. and Evans, J., 2000, Continental margin sedimentation, with special reference to the north-east Atlantic margin: *Sedimentology*, *v. 47* (Supplement 1), p. 239-256.

Wilson, C.K., Long, D. and Bulat, J., 2004, The morphology, setting and processes of the Afen Slide: *Marine Geology*, *v. 213*, p. 149-167.

Chapter 3: Preliminary Mapping and Analysis of Potential Landslide-generated Tsunamigenic Sources

Submarine landslides in the Gulf of Mexico are considered a potential tsunami hazard for two reasons: (1) some dated landslides in the Gulf of Mexico have post-glacial ages (Coleman *et al.*, 1983) and (2) recent suggestions from seismic records of small-scale energetic landslides in the Gulf of Mexico (Nettles, 2007) (see Chapter 6).

With regard to (1), the Mississippi Canyon landslide is dated at 7,500-11,000 yr BP (years before present) (Coleman *et al.*, 1983) and the East Breaks landslide is dated at 15,900 ± 500 yr BP (Piper and Behrens, 2003). Both landslides, which are among the largest landslides in the Gulf of Mexico, occurred after the end of the last glacial maximum, during post-glacial transgression. Although landslide activity along the passive margins of North America may be decreasing with time since the last glacial period, the 1929 Grand Banks landslide is a historic example of such an event that produced a destructive tsunami (Fine *et al.*, 2005). In addition, the Mississippi River continues to discharge large quantities of water-saturated sediments on the continental shelf and slope, making them vulnerable to over-pressurization and slope failure.

Tsunami Observations in the Gulf of Mexico

A review of the historical record reveals three events during the 20th century that are the primary tsunamis and seismic seiches measured and observed along the Gulf Coast. An additional entry in the National Geophysical Data Center (NGDC) tsunami database for the Gulf of Mexico occurred at Grand Isle, Louisiana on September 22, 1909. As indicated in the database, this event was likely caused by a hurricane, not a tsunami.

(1) The primary observation of October 1918 seismogenic tsunami originating west of Puerto Rico is a small wave of indeterminate amplitude recorded at the Galveston tide gauge station. The original reference for this observation appears to be the International Seismological Summary (Oxford Univ.) 1913-1934 as cited by Heck (1947). However, there is confusion regarding the date of the event. The date is listed as October 24, 1918 in the NGDC Tsunami Database (NGDC, 2007), cross-referenced to the date of a large aftershock following the devastating October 11, 1918 Puerto Rico earthquake and a tsunami observed at the Mona lighthouse (Puerto Rico) from that aftershock. In Heck (1947), Berninghausen (1968), and Lockridge *et al.* (2002), the date is listed as October 25, 1918. It appears that the

October 24, 1918 NGDC date is a local date (Lockridge *et al.*, 2002). All of the aforementioned reports clearly note that the waves recorded at Galveston did not occur on October 11, 1918 (date of the Puerto Rico mainshock).

(2) The primary observation of the May 2, 1922 event is a 0.64 m amplitude recorded at the Galveston tide gauge station. The original reference for this observation appears to be Parker (1922). The record is shown in Figure 3-1. The 1922 tidal disturbance is linked to an earthquake in Vieques only because of the unfortunate note by Parker (1922) with regard to a single seismograph station. The NEIC historical catalog for the Caribbean and for the world, which lists earthquakes estimated to be larger than 6, does not mention any earthquake in Vieques. The Centennial catalog of Engdahl and Villaseñor (2002), which is complete for magnitudes approximately 6.5 and greater, does not list this earthquake either. Finally, Bill McCann's unpublished local catalog for Puerto Rico (written communication, 2005), does not mention an earthquake at that time. It is more likely that the tidal disturbance was the result of a source local to the Gulf of Mexico and Galveston. If it was a landslide or a slow earthquake offshore Galveston, it would not have been felt. This event does emphasize the potential hazard from local sources.

(3) The primary references of seismic seiche waves originating from the March 27, 1964 Gulf of Alaska earthquake are reports by Donn (1964) and Berninghausen (1968) who indicated that the waves reached maximum height (peak-trough) of 0.18 m (7 in.) at the Freeport tide gauge station. These reports also refer to eyewitness observations of wave heights up to 2 m from this event.

Maximum Credible Submarine Landslides

We define three geological provinces in the Gulf of Mexico that are likely to be the origin of submarine landslides. The three provinces defined for the analysis are the Northwest Gulf of Mexico, Mississippi Canyon, Florida and Campeche Margins. The first two are canyon/fan provinces involving failure of terrigenous and hemipelagic sediment, whereas the third are carbonate provinces. The northern Gulf of Mexico coast would be affected primarily be the back-going tsunami emanating from the Northwest Gulf of Mexico (East Breaks) and Mississippi Canyon landslides, and would be affected primarily by the outgoing tsunami from a landslide sourced from above the Florida and Campeche Margins. For the tsunami sourced from the Florida Margin, there is a significant directivity effect that scales with the speed of downslope motion of the landslide (up to the phase speed of the tsunami). The characteristics and the parameters that define the maximum credible landslide are given below for the East Breaks Landslide in the Northwest Gulf of Mexico and the Mississippi Canyon and Florida Margin provinces.

Landslide volume calculations were based on measuring the volume of material removed from the landslide source area using a technique similar to that applied by ten Brink *et al.* (2006). Briefly stated, the approach involves using multibeam bathymetry to outline the extent of the source area, interpolating a smooth surface through the polygons that define the edges of the slide to provide an estimate of the pre-slide slope surface, and subtracting this surface from the present seafloor surface. These calculations were only completed for part of the East Breaks landslide, the Mississippi Canyon landslide, and a Florida Margin landslide. No calculations were made for failures above the Campeche Margin because available bathymetric data are inadequate. In the case of the East Breaks landslide, the

source area may be somewhat larger, but multibeam bathymetry is not available for the entire source area.

East Breaks Landslide

Geologic Setting: Shelf-edge delta
Post Failure Sedimentation: Canyon appears to be partially filled (predominantly failure deposits with some post-failure sedimentation)
Age: 10,000 – 25,000 years (Piper, 1997)
Maximum Credible Single Event (East Breaks landslide):

Max

Volume: 21.95 km^3
Area: 519.52 km^2

Min

Volume: 20.80 km^3
Area: 420.98 km^2

Other Reported Volumes: 50-60 km^3 (Trabant *et al.*, 2001)
Excavation depth: ~160 m (shelf to base of headwall scarp)
Run out distance: 91 km from end of excavation and 130 km from headwall based on GLORIA mapping (Rothwell *et al.*, 1991) (See Figure 3-2 and 3-3).
Other reported run-out distance: 160 km (Trabant *et al.*, 2001)

Mississippi Canyon

Geologic Setting: Shelf-edge delta and fan system
Post Failure Sedimentation: Canyon appears to be partially filled (failure deposits or post-failure sedimentation)
Age: 7,500 to 11,000 years (Coleman *et al.*, 1983; Chapter 3 in ten Brink *et al.*, 2007)
Maximum Credible Single Event:

Volume: 425.54 km^3
Other reported volumes – 1750 km^3 (Chapter 3 in ten Brink *et al.*, 2007); 1500-2000 km^3 (Coleman *et al.*, 1983)
Area: 3687.26 km^2
Excavation depth: ~300 m (in the upper canyon)
Runout distance: 297 km from toe of excavation area and 442 km from the headwall scarp (see Figure 3-4 and 3-5).

Florida Margin

Geologic Setting: Edge of a carbonate platform
Post Failure Sedimentation: None visible on multibeam images or on available high-resolution seismic profiles (Twichell *et al.*, 1993).
Age: Early Holocene or older (Doyle and Holmes, 1985)
Maximum Credible Single Event:

Volume: 16.2 km^3
Area: 647.57 km^2
Excavation depth: ~150 m, but quite variable
Runout distance: Uncertain. The landslide deposit is at the base of the Florida Escarpment buried under younger Mississippi Fan deposits (see Figure 3-6).

Campeche Margin

Geologic Setting: Carbonate platform

One of the persistent issues during the independent confirmatory analysis is acquiring sufficient geologic information about the Campeche Escarpment with which to estimate the maximum credible landslide parameters is done for other Gulf of Mexico provinces. Plans to conduct multibeam bathymetry surveys are pending clearance by Mexico to work in it's Exclusive Economic Zone. A similar request was denied in 2008. Presently, there is no published information showing the detailed bathymetry, nor distribution of landslides on or above the Campeche Escarpment.

Mobility Analysis

We have conducted a preliminary mobility analysis of the East Breaks landslide to determine the time scale of landslide dynamics as input into the tsunami generation and propagation model (COULWAVE) discussed in the next section. We use the method set forth by Locat, *et al.* (2004) for the Palos Verdes debris avalanche offshore southern California and in Chapter 7 of ten Brink *et al.* (2007) for the Currituck landslide offshore North Carolina.

Submarine landslide mobility is modeled using a bilinear rheology that combines characteristics of Newtonian and Bingham viscoplastic behaviors. The rheology is parameterized by an apparent yield strength (τ_{ya}), a reference strain rate

$$\gamma_r = \frac{\tau_{ya}}{\mu_{dh}} \qquad (1)$$

where μ_{db} is the plastic viscosity, and the ratio of strain rates

$$r = \frac{\gamma_r}{\gamma_o} \qquad (2)$$

where γ_o is the shear strain rate at the transition from Newtonian to Bingham behavior. The apparent yield strength is estimated using the following equation (Johnson, 1984):

$$\tau_{ya} = H_f \gamma' \sin\beta_f \qquad (3)$$

where H_f is the final flow thickness, γ' is the buoyant unit weight (kN/m^3), and β_f is the slope angle where the debris flow comes to rest. A reference strain rate of 1000 is used according to the estimate for clayey sediment by Jeong *et al.* (2007). As in the previous studies, we use the program BING (Imran *et al.*, 2001) to carry out the numerical computations of landslide dynamics in 1D.

Using a seafloor profile along the flank of the East Breaks landslide (*i.e.*, pre-slide conditions), we preliminarily estimate that τ_{ya} = 3000 Pa based on the runout distance and final flow thickness. This estimate is slightly smaller than that for the Palos Verdes debris avalanche (5000 Pa) and slightly larger than for the Currituck landslide (2000 Pa). The ratio of strain rates (r) is determined from a best fit to the runout length. Figure 3-7 below shows the initial parabolic thickness profile and thickness profile 30 minutes after failure.

In the region of excavation, the duration of vertical movement (defined as the time to reach a 90% reduction in thickness) is approximately 10 minutes. In the region of deposition, the duration of vertical movement is approximately 22 minutes. The phenomenon of hydroplaning during failure (De Blasio *et al.*, 2004; Elverhøi *et al.*, 2005) may increase the mobility of debris flows and result in shorter durations than estimated here. For comparison, a conservative value of 7.2 minutes was used for duration in modeling the Currituck landslide tsunami (Chapter 8 in ten Brink *et al.*, 2007)

This modeling will be further refined during the independent confirmatory analysis and performed for the other landslide provinces in the Gulf of Mexico.

Figures

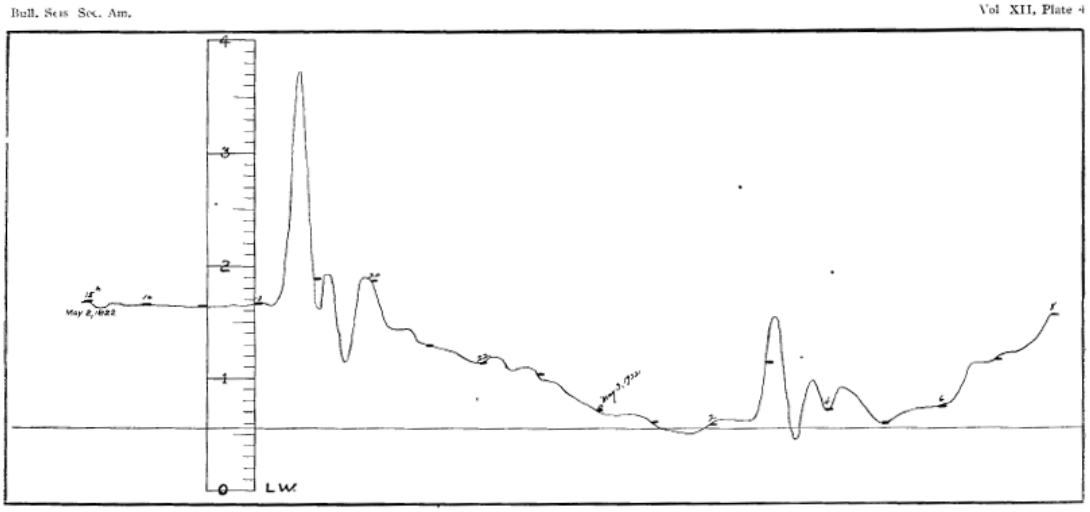

Figure 3-1: Galveston tide gauge record of the May 2, 1922 event (Parker, 1922). Scale in feet.

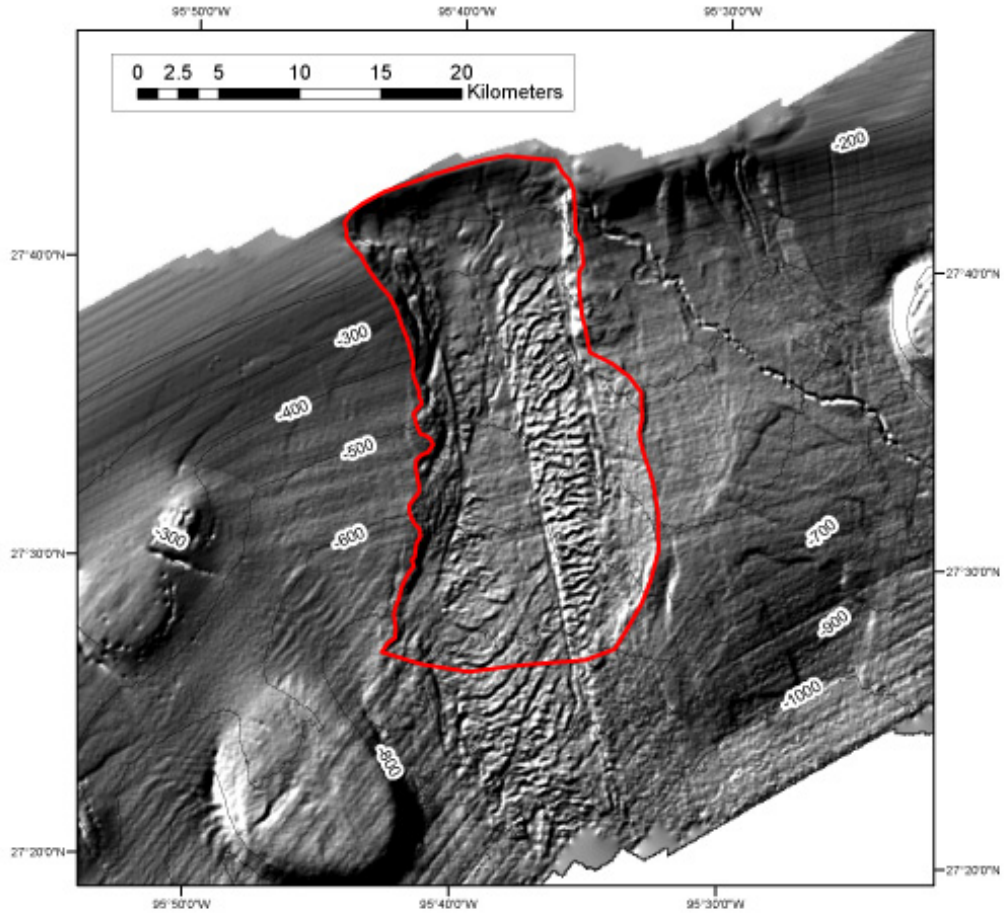

Figure 3-2: Outline (red) of excavation area for the East Breaks landslide based on available multibeam bathymetric data.

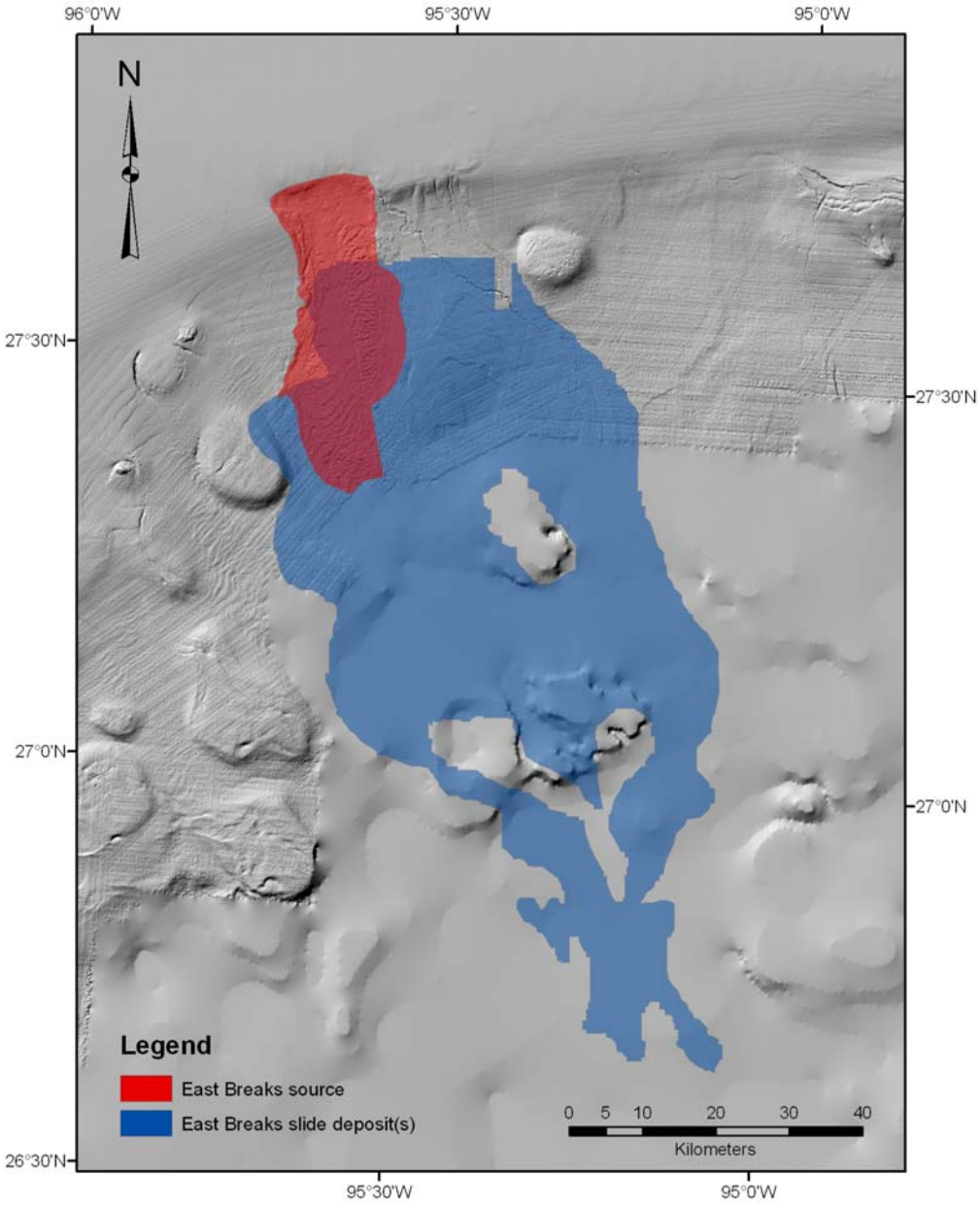

Figure 3-3: Comparison of excavation area (red) and depositional area (blue) for the East Breaks landslide. The extent of the landslide deposit was mapped using GLORIA sidescan sonar imagery (Rothwell et al., 1991).

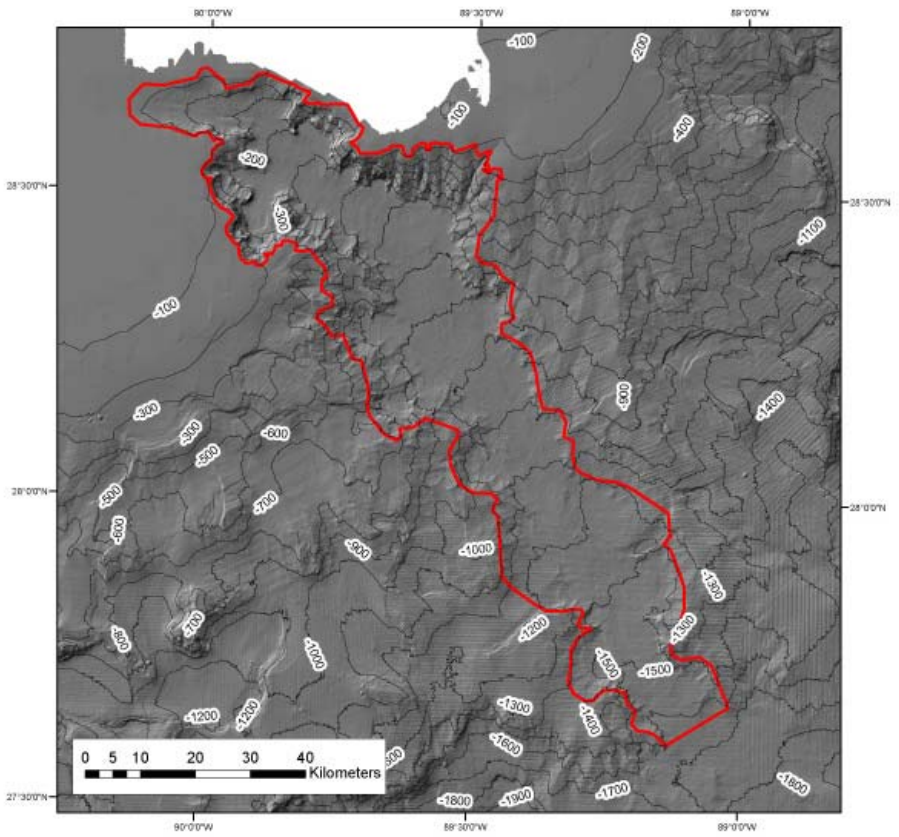

Figure 3-4: Outline (red) of excavation area for the Mississippi Canyon landslide based on multibeam bathymetric data and reports by Coleman and others (1983) and Goodwin and Prior (1989).

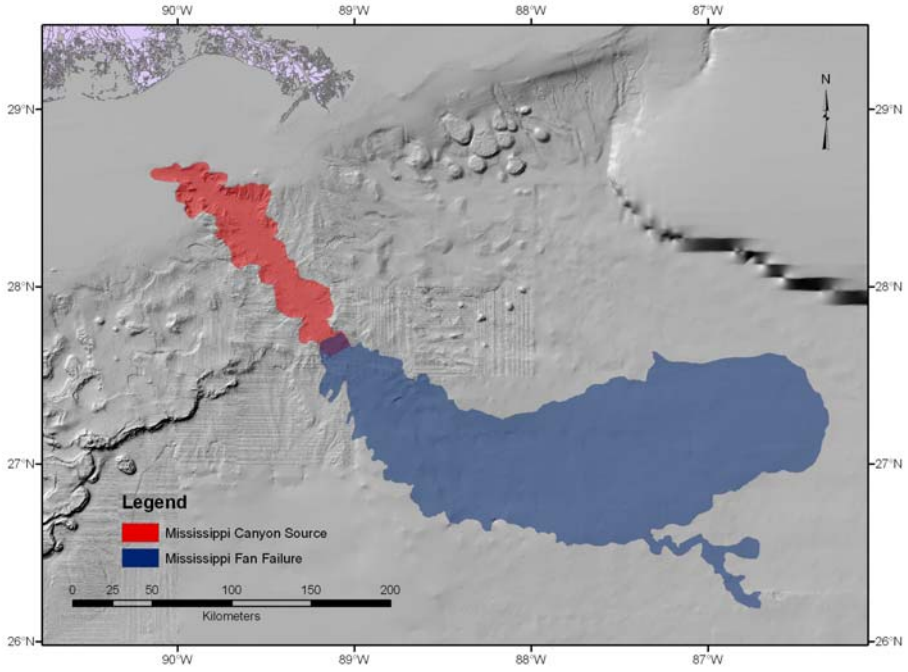

Figure 3-5: Comparison of excavation area (red) and depositional area (blue) for the Mississippi Canyon landslide. The extent of the landslide deposit is based on GLORIA sidescan sonar imagery (Twichell et al., 1991).

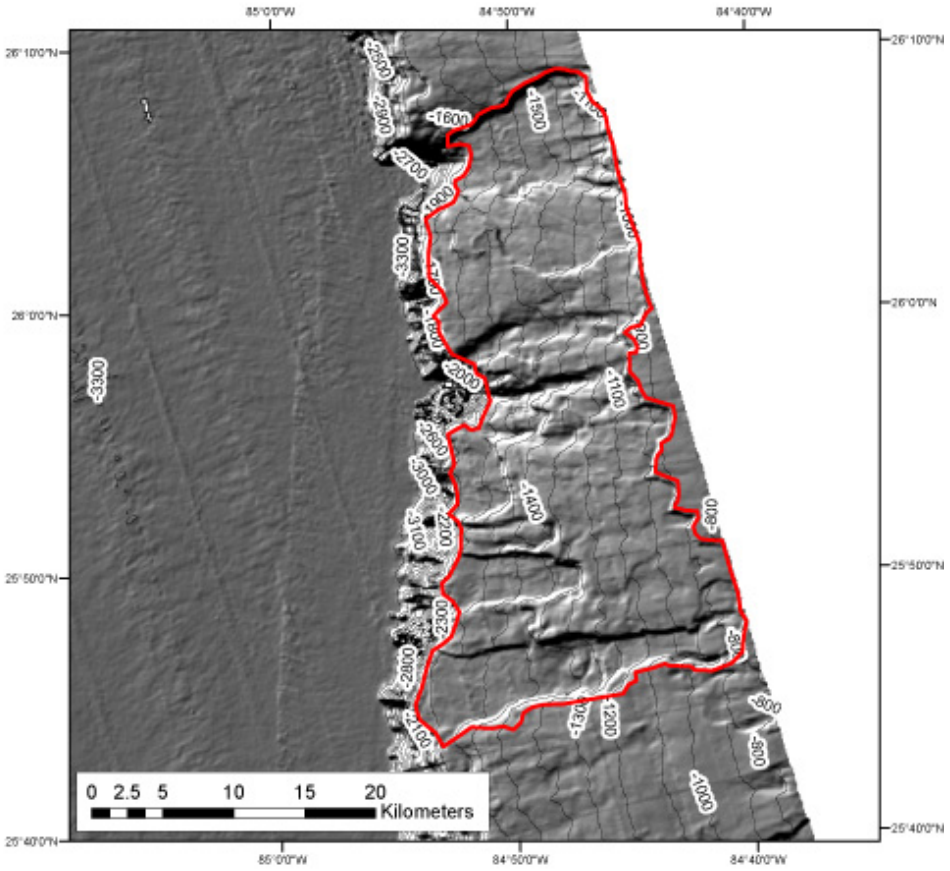

Figure 3-6: Outline (red) of excavation area for the maximum credible landslide above the Florida Escarpment from multibeam bathymetric data.

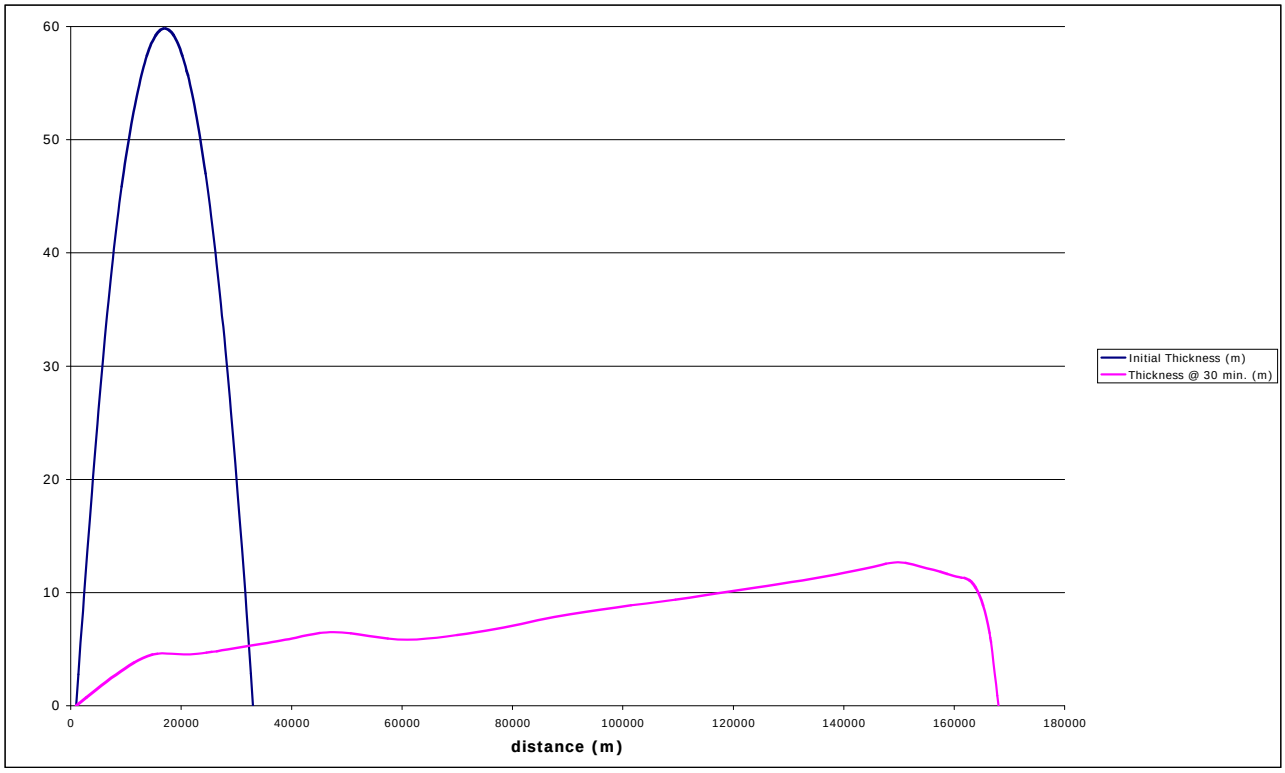

Figure 3-7: The initial parabolic thickness profile and thickness profile 30 minutes after failure.

References

Berninghausen, W.H., 1968, Tsunamis and Seismic Seiches Reported from the Western North and South Atlantic and the Coastal Waters of Northwestern Europe: Naval Oceanographic Office IR No. 68-85, 51 p. [Informal Report].

Coleman, J.M., Prior, D.B., and Lindsay, J.F., 1983, Deltaic influences on shelf edge instability processes, *in* Stanley, D.J., and Moore, G.T. (Editors), The shelfbreak: Critical interface on continental margins: *Society of Economic Paleontologists and Mineralogists Special Publication 33,* p. 121-137.

De Blasio, F.V., Ilstad, T., Elverhøi, A., Issler, D., and Harbitz, C., 2004, High mobility of subaqueous debris flows and the lubricating-layer model, in 2004 Offshore Technology Conference, Houston, TX, p. OTC 16747.

Donn, W.L., 1964, Alaskan earthquake of 27 march 1964: Remote seiche stimulation: *Science, v. 145*, p. 261-262

Doyle, L.J., and Holmes, C.W., 1985, Shallow structure, stratigraphy, and carbonate sedimentary processes of West Florida Continental Slope: *American Association of Petroleum Geologists Bulletin, v. 69*, p. 1133-1144.

Elverhøi, A., Issler, D., De Blasio, F.V., Ilstad, T., Harbitz, C.B., and Gauer, P., 2005, Emerging insights into the dynamics of submarine debris flows: *Natural Hazards and Earth System Sciences*, *v. 5*, p. 633-648.

Engdahl, E.R., and Villaseñor, A., 2002, Global seismicity: 1900-1999, *in* Lee, W.H.K., Kanamori, H., Jennings, P.C., and Kisslinger, C., eds., *International Handbook of Earthquake and Engineering Seismology, Part A*, San Diego, Academic Press, p. 665-690.

Fine, I.V., Rabinovich, A.B., Bornhold, B.D., Thomson, R., and Kulikov, E.A., 2005, The Grand Banks landslide-generated tsunami of November 18, 1929: preliminary analysis and numerical modeling: *Marine Geology*, *v. 215*, p. 45-57.

Heck, N.H., 1947, List of seismic sea waves: *Bulletin of the Seismological Society of America, v. 37*, p. 269-286.

Imran, J., Parker, G., Locat, J., and Lee, H., 2001, A 1-D numerical model of muddy subaqueous and subaerial debris flows: *Journal of Hydraulic Engineering*, *v. 127*, p. 959-958.

Jeong, S.W., Locat, J., Leroueil, S., and Malet, J.-P., 2007, *in* Lykousis, V., Sakellariou, D., and Locat, J., (Editors)., Submarine Mass Movements and Their Consequences: Springer, p. 191-198.

Locat, J., Lee, H.J., Locat, P., and Imran, J., 2004, Numerical analysis of the mobility of the Palos Verdes debris avalanche, California, and its implication for the generation of tsunmis: *Marine Geology*, *v. 203*, p. 269-280.

Lockridge, P.A., Lowell, S., Whiteside, L.A., Lander, J.F., 2002, Tsunamis and tsunami-like waves of the Eastern United States: *International Journal of the Tsunami Society*, *v. 20,* (3), p. 120-157.

Nettles, M., 2007, Analysis of the 10 February 2006 Gulf of Mexico earthquake from global and regional seismic data, *in* 2007 Offshore Technology conference, abstract #19099, Society of Petroleum Engineers. doi: 10.4043/19099-MS.

National Geophysical Data Center (NGDC) Tsunami Database, 2007, Revised November
6, 2007, http://www.ngdc.noaa.gov/seg/hazard/tsu_db.shtml.

Parker, W.E., 1922, Unusual tidal registration of earthquake: *Bulletin of the Seismological Society of America, v. 12*, p. 28-30.

Piper, J.N., 1997, Downslope sediment transport processes and sediment distributions at the East Breaks, northwest Gulf of Mexico: Austin, University of Texas, Thesis.

Piper, J.N., and Behrens, W.E., 2003, Downslope sediment transport processes and sediment distributions at the East Breaks, northwest Gulf of Mexico, in Proceedings of the 23rd Annual Gulf Coast Section SEPM Research Conference, Houston, TX, p. 359-385.

Rothwell, R.G., Kenyon, N.H., and McGregor, B.A., 1991, Sedimentary features of the south Texas continental slope as revealed by side-scan sonar and high-resolution seismic data: *American Association of Petroleum Geologists Bulletin, v. 75,* p. 298-312.

ten Brink, U.S., Geist, E.L., and Andrews, B.D., 2006, Size distribution of submarine landslides and its implication to tsunami hazard in Puerto Rico: *Geophysical Research Letters, v. 33,* p. doi:10.1029/ 2006GL026125.

ten Brink, U.S., Twichell, D., Geist, E.L., Chaytor, J., Locat, J., Lee, H., Buczkowski, B., and Sansoucy, M., 2007, The current state of knowledge regarding potential tsunami sources affecting U.S. Atlantic and Gulf Coasts, *U.S. Geological Survey Administrative Report*, 154 p.

Trabant, P., Watts, P., Lettieri, F.L., and Jamieson, A., 2001, East Breaks slump, northwest Gulf of Mexico, OTC 12960, in 2001 Offshore Technology Conference, Houston, TX, p. 231-238.

Twichell, D.C., Valentine, P.C., and Parson, L.M., 1993, Slope failure of carbonate sediment on the West Florida Slope, in, Schwab, W.C., Lee, H.J., and Twichell, D.C. (Editors), Submarine landslides: Selected studies in the U.S. Exclusive Economic Zone, *U. S. Geological Survey Bulletin 2002*, p. 69-78.

Chapter 4: Hydrodynamic Modeling of Tsunamis Generated by Potential Landslide Sources

Detailed tsunami analysis is performed for two local landslide scenarios: (1) a scenario fashioned after the East Breaks landslide and (2) a hypothetical landslide along the Campeche Escarpment. For each case, tsunami propagation, runup, and inundation was computed using COULWAVE. The numerical model COULWAVE (Lynett and Liu, 2002) solves the fully nonlinear extended Boussinesq equations on a Cartesian grid. COULWAVE has the capability of accurately modeling the wind waves with both nonlinear and dispersive properties. A particular advantage of the model is the use of fully non-linear equations for both deep and shallow water. This avoids the common problem of "splitting" the analysis when the wave reaches shallow water. Applications for which COULWAVE has proven very accurate include wave evolution from intermediate depths to the shoreline, including parameterized models for wave breaking and bottom friction. COULWAVE is based on the Boussinesq-type equations, which are known to be accurate for inviscid wave propagation from fairly deep water (wavelength/depth ~2) all the way to the shoreline (Wei and others, 1995). The equation model consists of a fairly complex set of partial differential equations which are integrated in time to solve for the free surface elevation and the horizontal velocity vector. A fourth order Adams-Bashforth-Moulton predictor-corrector time integration scheme is required, and the spatial derivatives are approximated with fourth order, centered finite differences. The high order scheme is required due to the inclusion of first to third order derivatives in the model equations. Waves are generated in the numerical domain with an internal source (Wei and others, 1999), which can use as input a wave energy spectrum to create a directional, random wave field. In conjunction with the internal source generator, sponge layers are placed along the outgoing lateral boundaries, and provide excellent wave absorption across a wide range of frequencies and amplitudes.

Numerical Grid Development

The bathymetry/topography grid required by the hydrodynamic model is created via two main sources: 1) the Smith and Sandwell (SS) 2-minute global elevation database, and 2) a recent Gulf of Mexico grid created by the U.S. Army Corps of Engineers for use with the storm surge model ADCIRC. The ADCIRC grid is a blend of numerous sources including recent lidar surveys and digitized elevation maps. The ADCIRC grid was used for

bathymetry and topography at locations with bottom elevations greater than -500 m. For depths greater than this (or elevations lower), the SS was primarily used. Barrier islands, coastal waterways, and rivers are all well resolved.

Initial Numerical Simulations – Physical Limits

The purpose of these initial simulations is to provide an absolute upper limit of the tsunami wave height that could be generated. Note that these limiting simulations use physical assumptions that are arguably unreasonable but provide maximum amplitude estimates Specifically, these assumptions are:

(1) Time scale of the seafloor motion is very small compared the period of the generated water wave (tsunami)
(2) Bottom roughness, and the associated energy dissipation, is negligible in locations that are initially wet (*i.e.* locations with negative bottom elevation, offshore)

Assumption (1) simplifies the numerical analysis considerably. With this assumption, the free water surface response matches the change in the seafloor profile exactly. This type of approximation is used commonly for subduction-earthquake-generated tsunamis, but is known to be very conservative for landslide tsunamis (Lynett and Liu, 2002). The initial pre-landslide bathymetry profile, as estimated by examination of neighboring depth contours, is subtracted by the post (existing) landslide bathymetry profile. This difference surface is smoothed and then used directly as a "hot-start" initial free surface condition in the hydrodynamic model. A hot-start initial free water surface condition (*i.e.*, the free water surface response matches the change in the seafloor profile exactly).

Assumption (2) does not simplify the analysis significantly; however is does prevent the use of an overly high bottom roughness coefficient, which could artificially reduce the tsunami energy reaching the shoreline. Note that while the offshore regions are assumed to be without bottom friction, such an assumption is too physically unrealistic to accept for the inland regions where the roughness height may be the same order as the flow depth. For tsunami inundation, particularly for regions such as this project location where the wave would need to inundate long reaches of densely vegetated land to reach the site, inclusion of some measure of bottom roughness is necessary.

East Breaks Landslide Source

As provided in the landslide characterization section, the excavation depth of this slide is approximately 160 m. Therefore, a trough elevation of -160 m is used for the hot-start initial water surface condition. The horizontal dimensions of the slide source region are ~12 km in width and 50 km in length. With this information, and knowledge of characteristic slide-generated waves taken from the literature (Lynett and Liu, 2002; Lynett and Liu, 2005), the hot-start initial condition is constructed as shown in Figure 4-1. From this, model results (Figure 4-2) indicate that wave components (back-going and outgoing) with amplitudes greater than 20 m is initially generated..

For the East Breaks landslide, both one-horizontal-dimension (1HD) and two-horizontal dimension (2HD) simulations were preformed. The 1HD simulations require a small fraction of the CPU time of the 2HD runs, but do not include the radial spreading and refraction effects. Lack of radial spreading will lead to a conservative result in 1HD, while

refraction can be either a constructive or destructive effect on the wave height, depending on the shallow water depth contours.

Examination of the 2HD simulation provides information about the importance of radial spreading and refraction, relative to 1HD results. A constant spatial grid size of 200 m is used in the 2HD results; use of the refined 25 m from the 1HD simulations creates an impractical, large grid. With the 200 m grid, the 2HD simulation uses 10 million grid points, and requires 20 weeks of CPU time (1 day on 144 processors).

It is most reasonable to analyze the 2HD results only to the initial shoreline. The relatively coarse grid size used in the 2HD results might cause accuracy degradation during the inundation phase due to poor resolution of shallow bathymetric and on land features. Figure 4-2 provides a series of snapshots of the 2HD result. Clearly, radial spreading is important, as wave energy is propagating in all directions away from the source. The depth contours are relatively uniform seaward of the west Texas coast, and there is no clear amplification due to refraction. With no refractive amplification, and significant radial spreading, it should be expected that the 2HD tsunami height prediction be less than the 1HD near the shoreline. Indeed that is the case, with the 2HD simulation yielding bore height predictions on the order of +8 m at the shoreline, or 1/3 of the 1HD prediction.

Further modeling and analysis is required to determine if the entire coastline of the Gulf of Mexico would be impacted by a tsunami generated by this source. The magnitude of the tsunami at the coast would be determined by shallow water amplification and energy dissipation of the waves. Furthermore, using landslide durations predicted from the mobility analysis rather than hot-start conditions we expect to see a change in tsunami generation efficiency.

The Campeche Margin

Campeche Landslide

Presently, there is no published information showing the detailed bathymetry nor distribution of landslides on or above the Campeche Margin. As a provisional source for the Campeche Margin, we used initial conditions applicable to the maximum observed landslide along the slope above the Florida Margin, a similar geologic environment (see Chapter 3). This includes an initial drawdown of 150 m, with a horizontal length scale of 20 km (Figure 4-3). The placement of this initial condition is arbitrary, but optimally oriented directly across from south Texas. The very steep slope of the Campeche Margin results in the maximum depression occurring over a depth of 500 m, whereas the maximum positive wave of the initial condition occurs over a depth of 1000 m.

Results: 2HD

Figures 4-4, 4-5, and 4-6 provide a series of snapshots of the 2HD result for a slide width of 20 km. For the sake of comparison, and the fact that there is a high degree of uncertainty in the source parameters for this scenario, a second simulation with a slide width of 60 km was run. The wave heights decrease very quickly near the source, but reach a nearly steady (slowly attenuating) condition when reaching the continental shelf off the Gulf Coast.

Figures 4-7, 4-8, and 4-9 provides a series of snapshots of the 2HD result for the 60 km width case.

Figure 4-10 plots the ocean surface elevation time series for the two slides at an offshore water depth of 50 m directly across from Matagorda Bay, TX. Of note is the larger wave with the wider source, and the fact that the Campeche event creates a leading elevation wave.

It was expected that because the propagation distance for Campeche is so much larger than East Breaks (about 700 km longer), the 2D spreading effect is significant, and results in greater attenuation than for the East Breaks scenario. Figure 4-11 compares the ocean surface elevation time series for the offshore Campeche 20-m wide slide and the East Breaks (2HD simulations) at the same 50-m depth offshore location. The general conclusion made from this comparison is that the approaching wave heights for the hypothetical Campeche scenario are comparable to that of the East Breaks scenario, unless it is found that the maximum slide width in the Campeche province is much less than 20 km. Because the properties of the incoming waves are different (leading elevation vs. leading depression), and the uncertainty in the slide parameters, this analysis indicates that East Breaks and Campeche (20 km width) should have equal tsunami potential on the Texas coast.

Independent analysis of the 10% exceedance high tide was conducted for 16 years of NOAA NOS-CO-OPS data at the Freeport tide gauge station (years 1992-2007). The 10% exceedance high tide was determined to be 0.45 m relative to MSL for these years. The long-term sea-level rise at the Freeport station is 4.35±1.12 mm/yr according to NOAA NOS-CO-OPS data. Therefore, the potential maximum water level for the conservative 2HD tsunami over the next century is 4 m (max. tsunami runup) + 0.45 m (10% exceedance high tide) + 0.59 m (century sea level rise) or approximately 5.0 m (16.5 feet).

Conclusion: Results of the analysis indicates that the largest possible tsunami source is a submarine landslide, either along the continental slope directly across from the site (i.e., East Breaks scenario) or along the Campeche margin. There is a high degree of uncertainty in the source parameters for the latter scenario. Hot-start initial conditions were used representing conservative values related to tsunami generation efficiency. In addition, several bottom friction parameters for overland flow were tested, representing realistic and conservative estimates. Realistic wave propagation in two horizontal dimensions (2HD), yielded the largest possible tsunami runup approximately 4 m (relative to MSL) for conservative hot-start initial conditions.

Seismic Seiches

Seismic seiches are fundamentally a different type of wave than tsunamis. Rather than being impulsively generated by displacement of the sea floor, seismic seiches occur from resonance of seismic surface waves (continental Rayleigh and Love waves) with enclosed or semi-enclosed bodies of water. The harmonic periods of the oscillation are dependent on the dimensions and geometry of the body of water. In 1964, seiches were set up by along the Gulf Coast from seismic surface waves emanating from the M=9.2 Gulf of Alaska earthquake. The efficiency at which the seiches occurred at great distance from the earthquake is primarily explained by amplification of surface wave motion from the thick sedimentary section along the Gulf Coast (McGarr, 1965). Because the propagation path from Alaska to the Gulf Coast is almost completely continental (McGarr, 1965) and because the magnitude of the 1964 earthquake is close to the maximum possible for that subduction

zone (*e.g.*, Bird and Kagan, 2004), it is likely that the historical observations of 1964 seiche wave heights are the maximum attainable.

Conclusion

In summary, we list the following findings of our independent confirmatory analysis of the tsunami source characteristics below:

- There is sufficient evidence to consider submarine landslides in the Gulf of Mexico as a present-day tsunami hazard.
- Four geologic landslide provinces are defined in the Gulf of Mexico: Northwest Gulf of Mexico, Mississippi Canyon, Florida/Campeche Margin. The propagation paths that result in the least attenuation of potential tsunamis are for the East Breaks and Campeche provinces.
- Parameters for the maximum credible submarine landslide were determined for each of the provinces, except for the Campeche Margin where we are awaiting additional data.

It is likely that seismic seiche waves resulting from the 1964 Gulf of Alaska earthquake are nearly the highest possible, owing to a predominantly continental ray path for seismic surface waves from Alaska to the Gulf Coast.

Figures

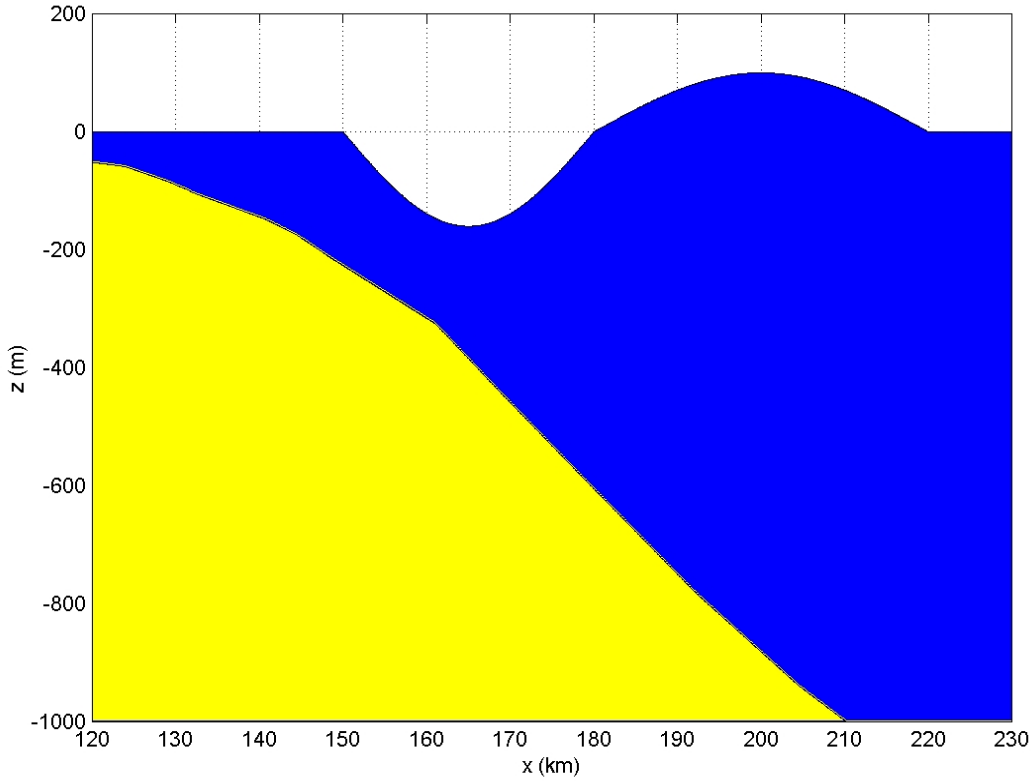

Figure 4-1: Centerline profile of the hot-start water surface condition used for the limiting East Breaks landslide tsunami simulations.

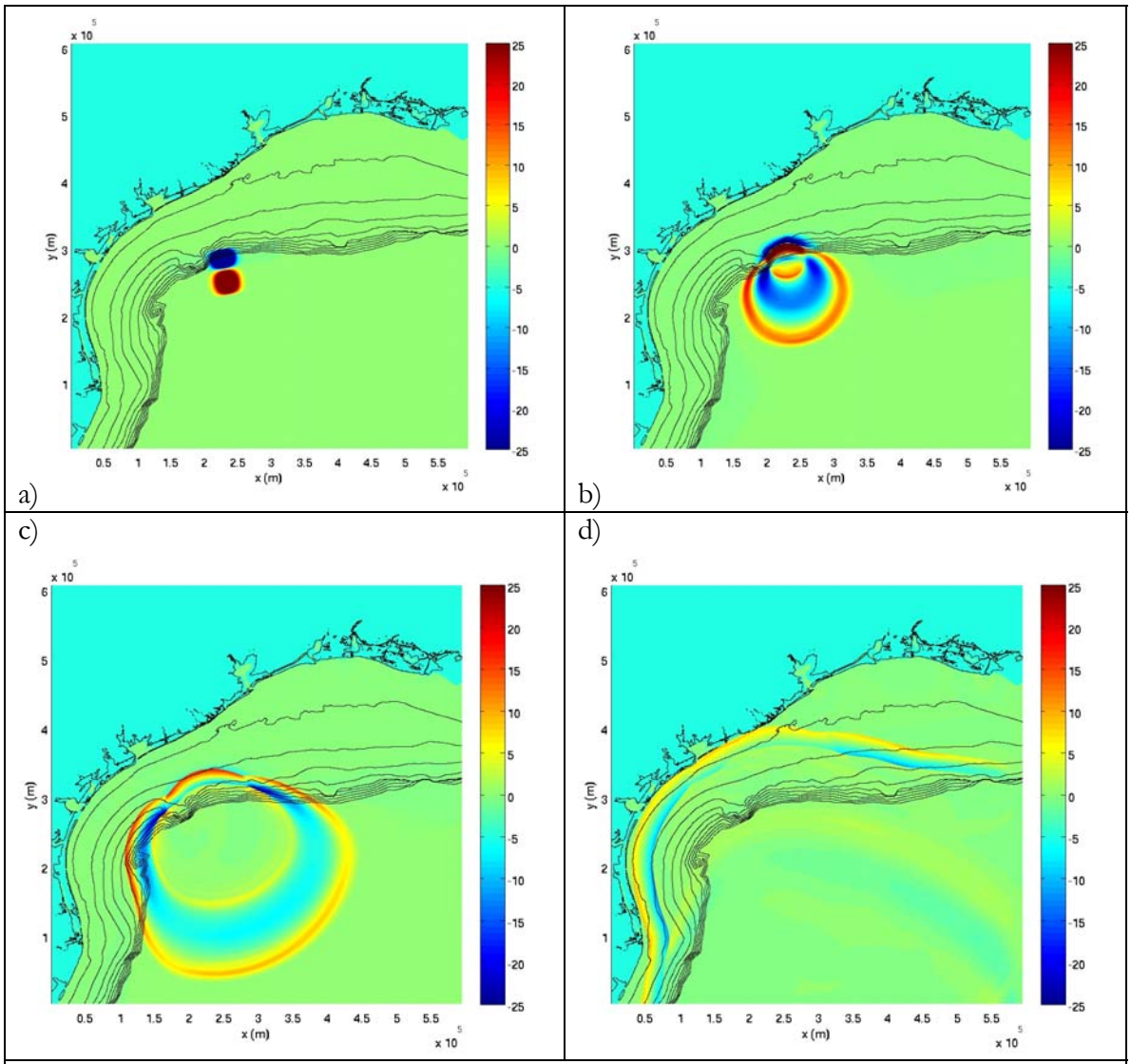

Figure 4-2: Results of two-dimensional simulation of the East Break landslide (headwall depth is 160 m) at (a) 0 minutes (initiation) ,(b) 13 minutes, (c) 33 minutes, and (d) 83 minutes. Note the radial spreading pattern.

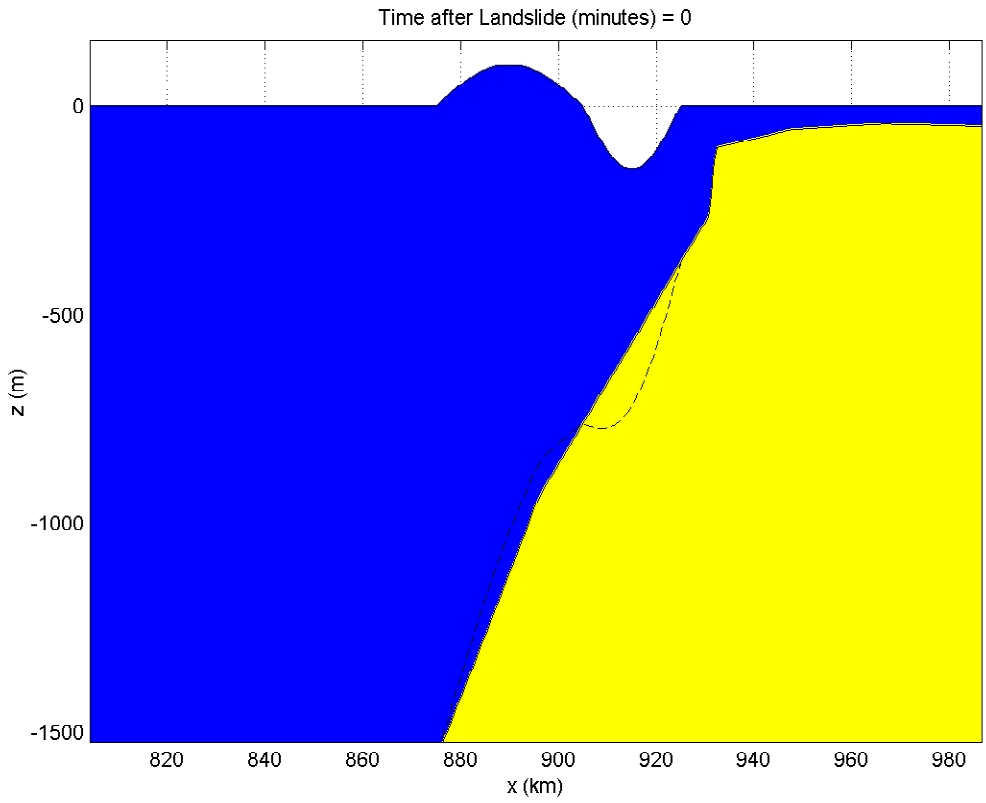

Figure 4-3: Centerline profile of the hot-start water surface condition used for the limiting Campeche landslide tsunami simulations.

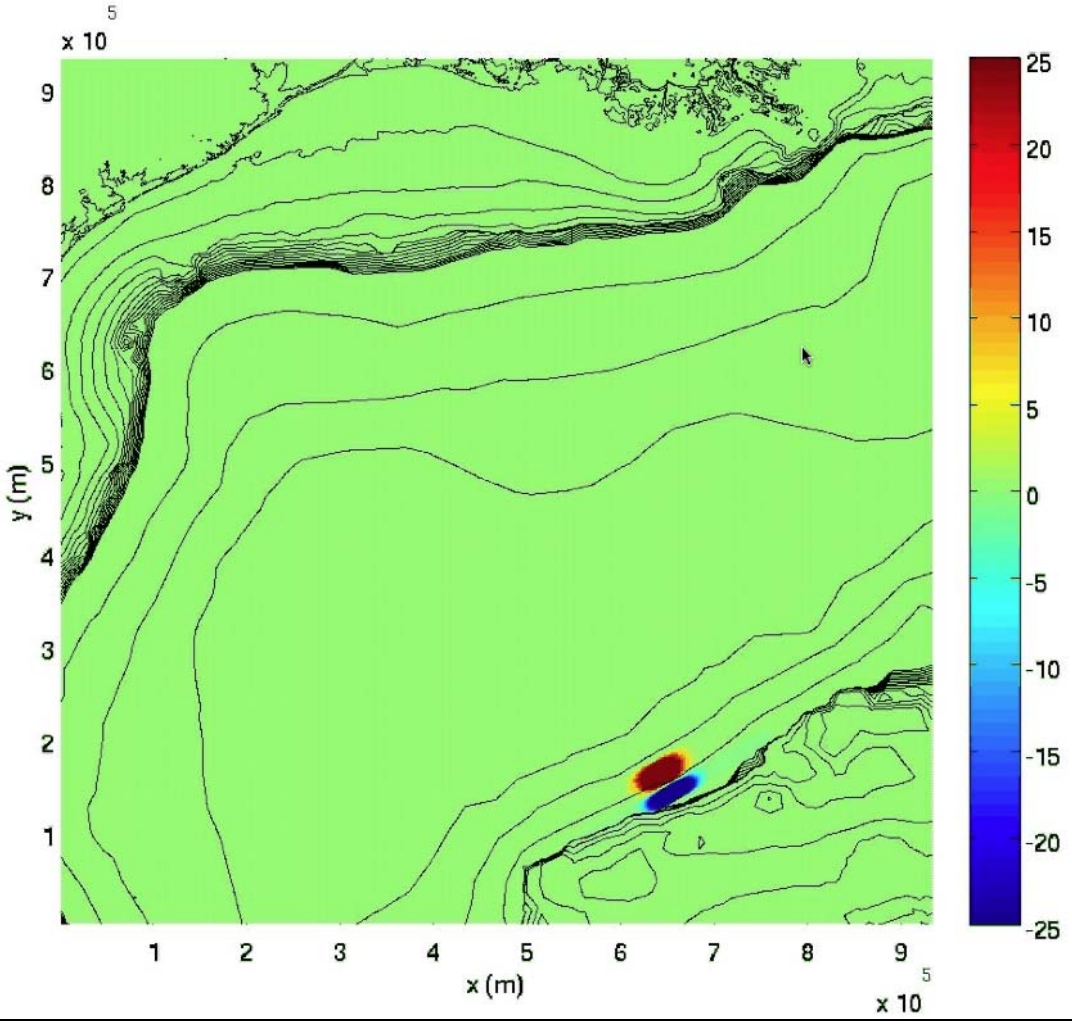

Figure 4-4: Spatial snapshots (plan view) of the tsunami wave field from the 2HD simulation using a 20 km slide width. Start time during tsunami generation.

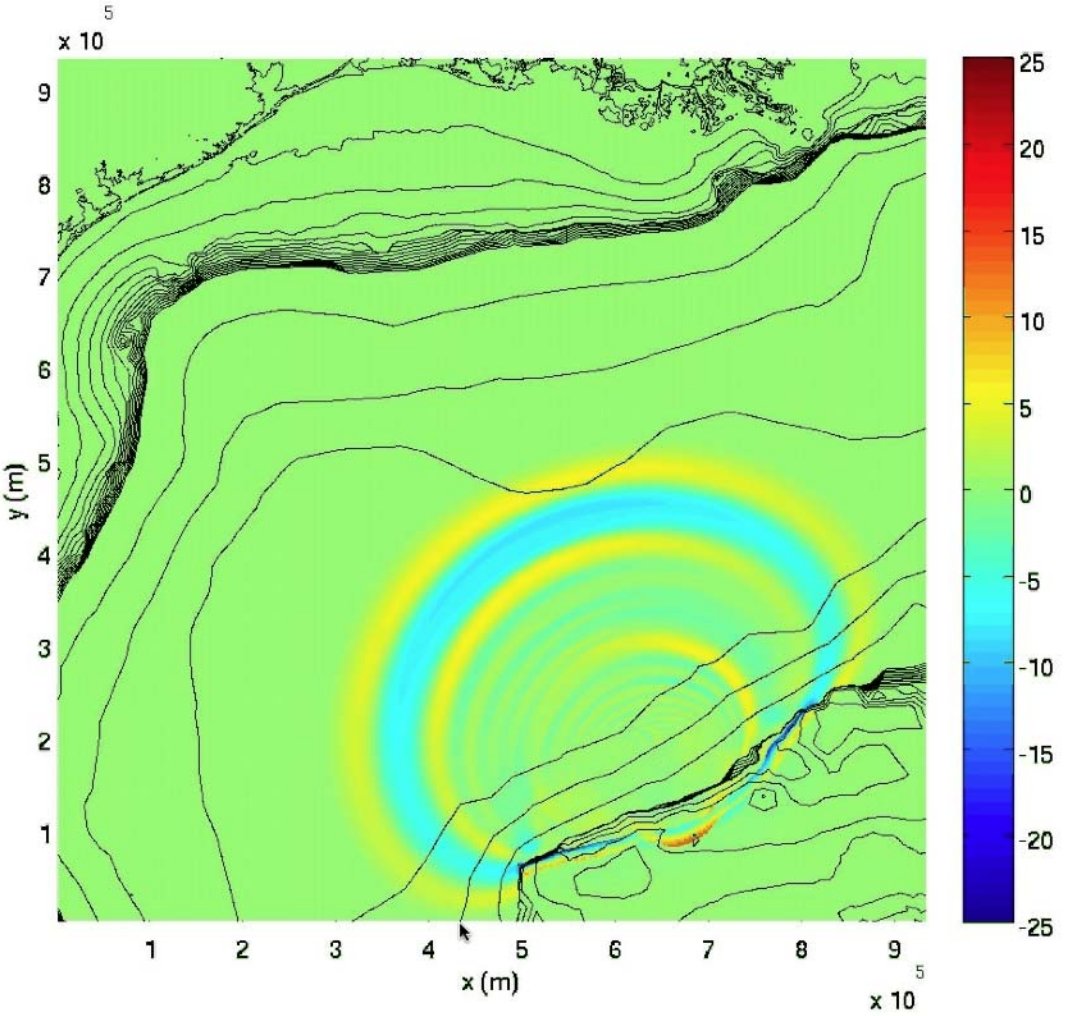

Figure 4-5: Spatial snapshots (plan view) of the tsunami wave field from the 2HD simulation using a 20 km slide width. Time during propagation across the deep Gulf of Mexico.

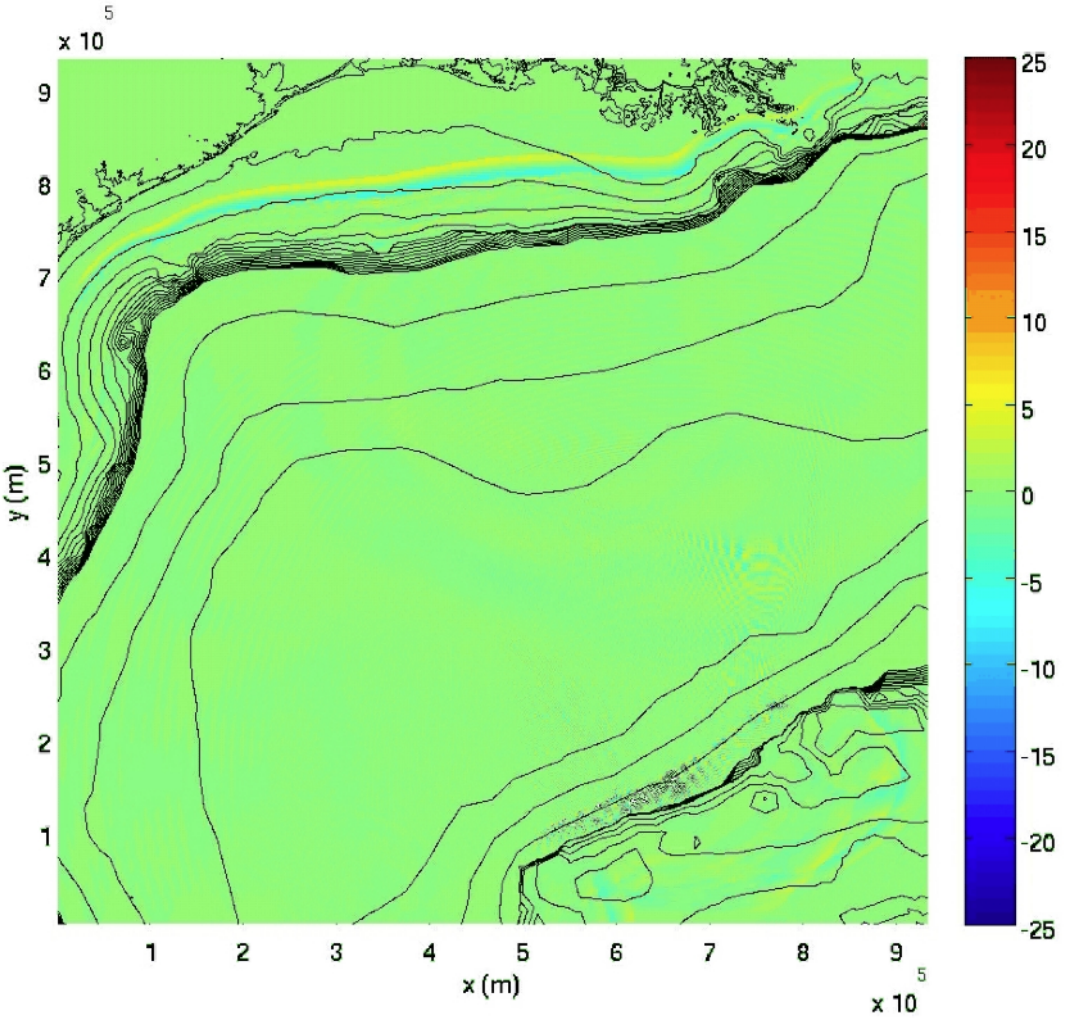

Figure 4-6: Spatial snapshots (plan view) of the tsunami wave field from the 2HD simulation using a 20 km slide width. Time during propagation across the south Texas continental shelf.

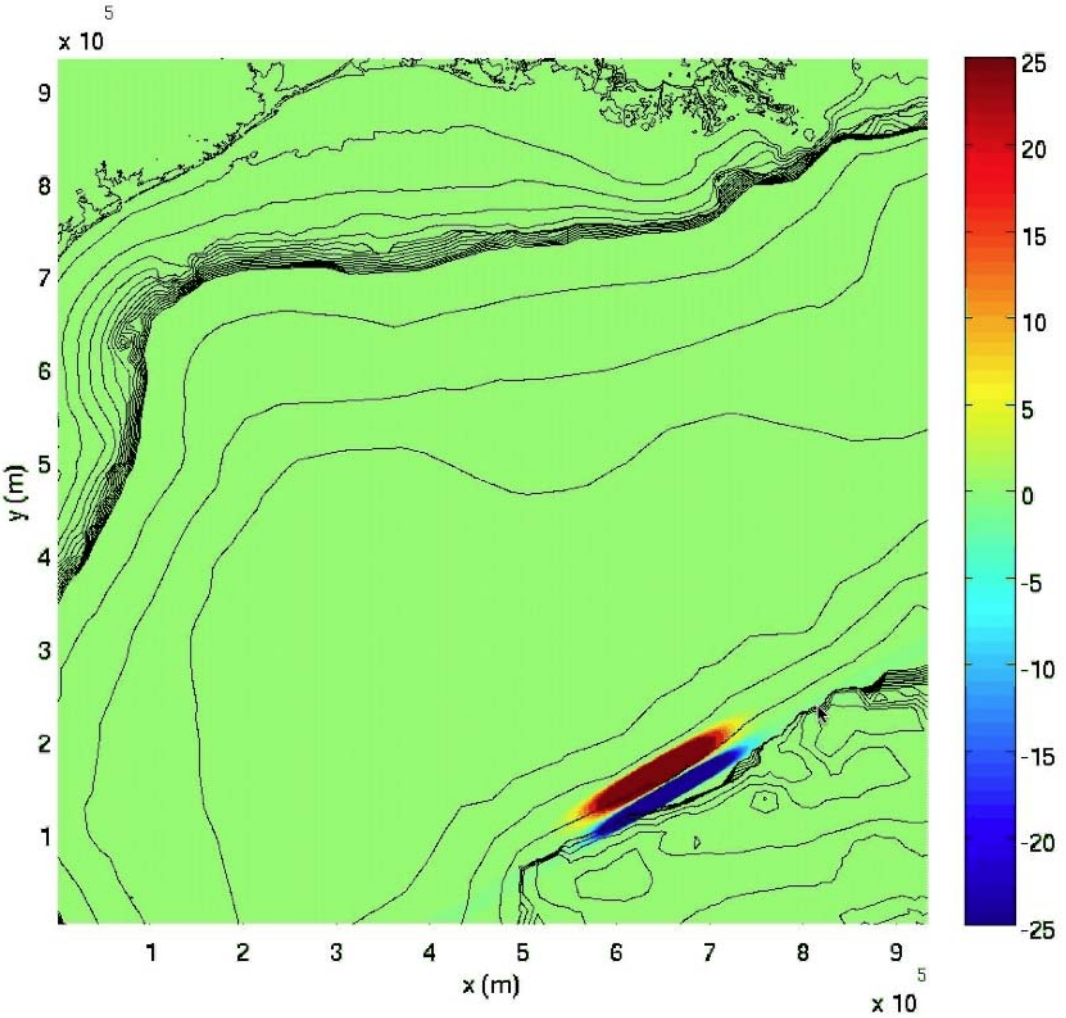

Figure 4-7: Spatial snapshots (plan view) of the tsunami wave field from the 2HD simulation using a 60 km slide width. Start time during tsunami generation.

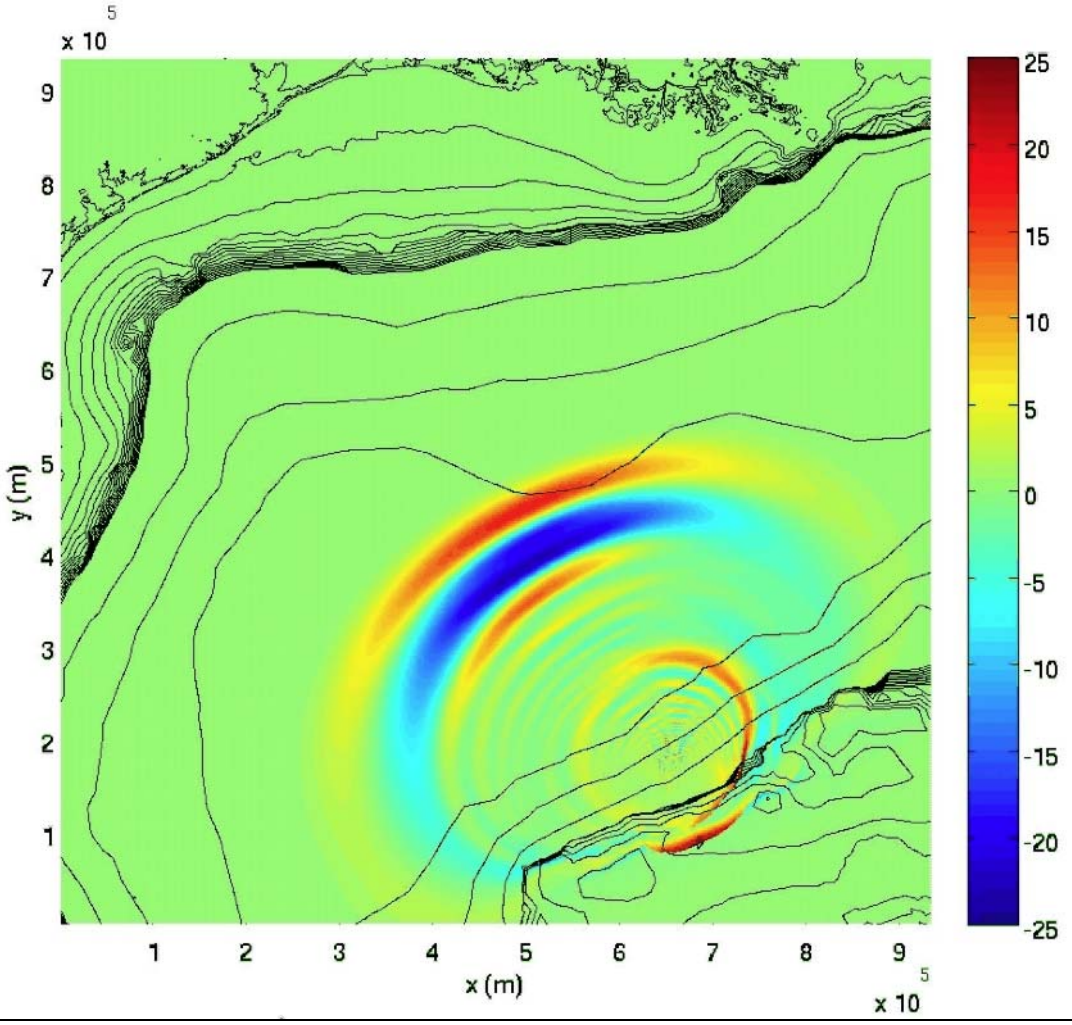

Figure 4-8: Spatial snapshots (plan view) of the tsunami wave field from the 2HD simulation using a 60 km slide width. Time during propagation across the deep Gulf of Mexico.

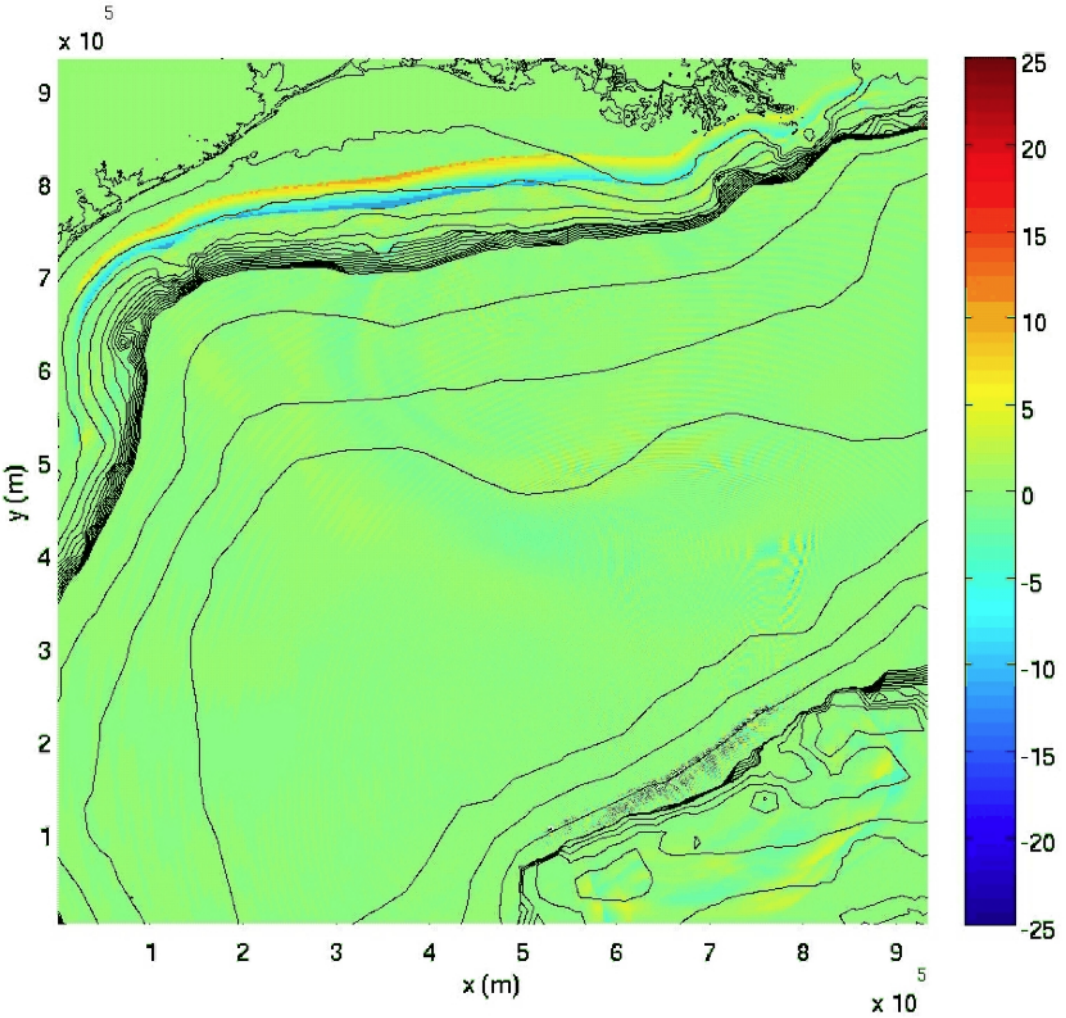

Figure 4-9: Spatial snapshots (plan view) of the tsunami wave field from the 2HD simulation using a 60 km slide width. Time during propagation across the south Texas continental shelf.

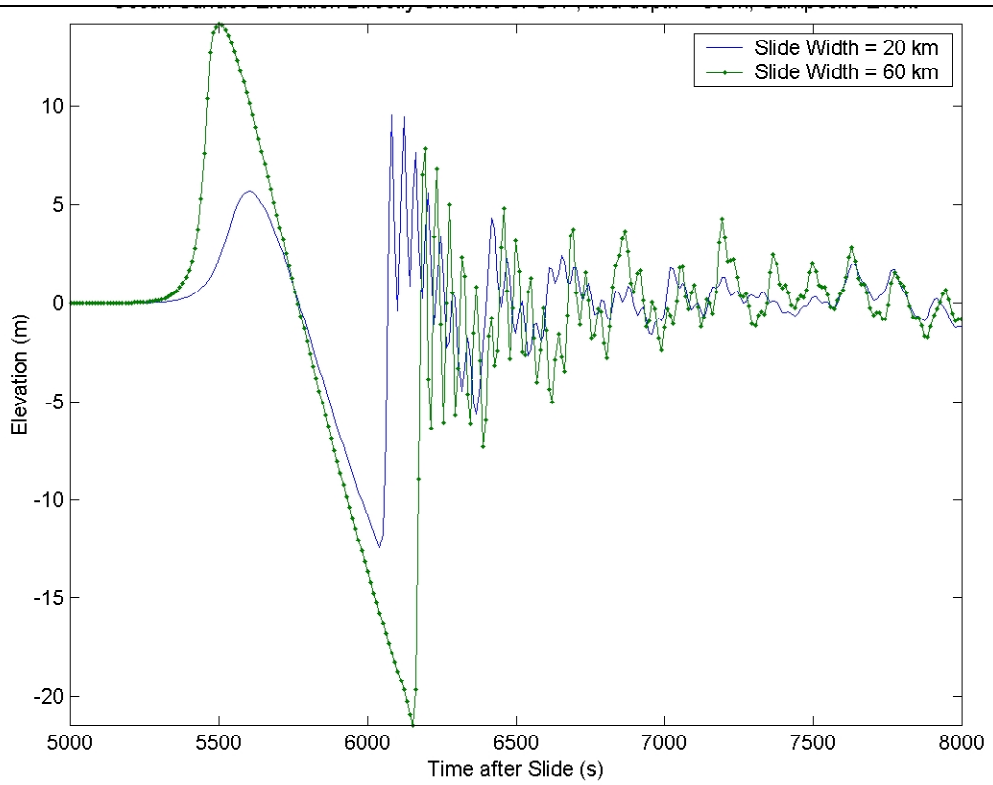

Figure 4-10: Synthetic tsunami time series (marigrams) for the Campeche hypothetical landslide scenario, using two landslide widths directly offshore South Texas at a water depth of 50 m.

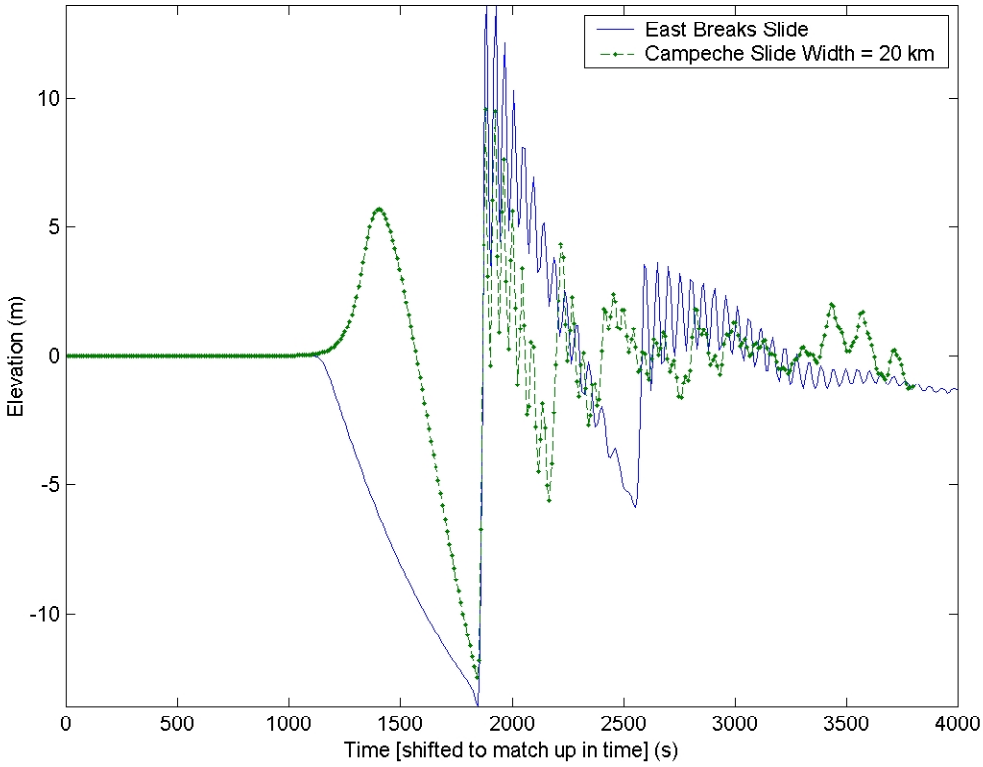

Figure 4-11: Synthetic tsunami time series (marigrams) for the Campeche hypothetical landslide scenario and the East Breaks landslide scenario. Ocean surface elevation at a water depth of 50 m.

References

Aharon, P., 2003, Meltwater flooding events in the Gulf of Mexico revisited: Implications for rapid climate changes during the last deglaciation: *Paleoceanography, v. 18*, 1079, doi: 10.1029/2002PA000840.

Bird, P., and Kagan, Y. Y., 2004, Plate-tectonic analysis of shallow seismicity: apparent boundary width, beta-value, corner magnitude, coupled lithosphere thickness, and coupling in 7 tectonic settings: *Bull. Seismol. Soc. Am., v. 94*, 2380-2399.

Geist, E.L., and Parsons, T., 2009, Assessment of source probabilities for potential tsunamis affecting the U.S. Atlantic coast: *Marine Geology*, *v. 264*, pp. 98-108.

Lockridge, P.A., Lowell, S., Whiteside, L.A., Lander, J.F., 2002, Tsunamis and tsunami-like waves of the Eastern United States: *International Journal of the Tsunami Society*, *v. 20*(3), p. 120-157.

Lynett, P. and Liu, P.L.F., 2002, A numerical study of submarine-landslide-generated waves and run-up: *Proceedings of the Royal Society of London, A*, *v. 458*, p. 2885-2910.

Lynett, P.J. and Liu, P.L.-F., 2005, A numerical study of run-up generated by three-dimensional landslides: *Journal of Geophysical Research*, *v. 10*: doi:10.1029/ 2004JC002443.

McGarr, A., 1965, Excitation of seiches in channels by seismic waves: *Journal of Geophysical Research, v. 70*, p. 847-854.

Twichell, D.C., Nelson, C.H., Kenyon, N. and Schwab, W., 2009, The influence of external processes on the Holocene evolution of the Mississippi Fan, *in,* Kneller, B., McCaffrey, W., Martinsen, O., and Posamentier, H. (Editors), External Controls on Deep Water Depositional Systems: Climate, sea-level, and Sediment Flux, SEPM Special Publication no. 92, p. 145-157.

Wei, G., Kirby, J.T., Grilli, S.T., and Subramanya, R., 1995, A fully nonlinear Boussinesq model for surface waves. Part 1. Highly nonlinear unsteady waves: *Journal of Fluid Mechanics, v. 294*, p. 71-92.

Wei, G., Kirby, J.T., and Sinha, A., 1999, Generation of waves in Boussinesq models using a source function method: *Coastal Engineering, v. 36*, p. 271-299.

Chapter 5: Tsunamigenic Earthquake Sources That May Affect the Gulf of Mexico

Introduction

Earthquake-generated tsunamis generally originate by the sudden vertical movement of a large area of the seafloor during an earthquake. Such movement is often generated by reverse faulting, in subduction and collision zones although normal faulting can also generate vertical movements of the sea floor (e.g. Bakran & ten Brink, submitted to BSSA). The Gulf of Mexico basin is devoid of subduction zones or potential sources of large reverse faults. However, the Caribbean basin contains two convergence zones and a strike-slip plate boundary whose rupture may affect the Gulf of Mexico, the North Panama Deformation Belt and the Northern South America Convergent Zone, and the western side of the Cayman Trough (Figure 5-1, 5-2). Hydrodynamic modeling is needed to evaluate the role of the Yucatan straits (between Cuba and the Yucatan Peninsula) in modifying the propagation of tsunamis into the Gulf of Mexico. The following is a review of local earthquakes in the Gulf of Mexico followed by a review of these convergent zones and western Cayman Trough.

2006 Green Canyon Earthquake

The February 10, 2006 earthquake offshore southern Louisiana in an area known as the Green Canyon, was an unusual earthquake (Figure 5-3). Unlike other earthquakes of its size, the Green Canyon earthquake was rich in low frequency energy and poor in high-frequency energy. This fact was manifested in the magnitude determination of the earthquake as Mb=4.2, Ms=5.3 (Dewey and Dellinger, 2008) where Mb and Ms refer to body waves and surface waves magnitude, respectively. Shown in Figure 5-4 is the multibeam bathymetry near the event and in Figure 5-5, 3 seismograms and accompanying spectrograms: the first for a typical earthquake, the second for a known landslide in SE Alaska, and the third for the 2006 Gulf of Mexico event (P. Whitmore, personal communication). Inefficient generation of high-frequency energy can occur in faulting of weak sedimentary rock at shallow depth (Kovach, 1974; Ottenmøller *et al.*, 2005) and in landslides (Kanamori and Given, 1982; Nettles, 2007). If the earthquake was caused by a landslide, then energetic landslides continue to occur in the Gulf of Mexico. Although most landslides affected by salt tectonics are small in size (*e.g.*, in comparison to the East Breaks landslide; Chapter 3 of this report)

and are unlikely to be tsunamigenic, because the 2006 event generated seismic energy, it had to have occurred rapidly, and would couple efficiently with movement in the water column. However, comparison of a recent multibeam bathymetry survey in the epicenter area to previous surveys does not show evidence for a recent landslide (Dellinger et al., 2009).

The other possible cause of that earthquake is slip on a shallow sub-horizontal surface. Kovach (1974) and Ottenmöller *et al.* (2005) documented such events, which were associated with either pumping from or water injection into the subsurface. However, Gangopadhyay and Sen (2008) explained the cause of the Green Canyon earthquake, as well as other moderate earthquake that occurred in the Gulf of Mexico in 2006 (04/18/2006 Mw 4.6; 09/10/2009 Mw 5.8) and earlier earthquakes by differential stress developing because of contrast in the mechanical properties between salt and the surrounding rock, driven by background tectonic loading. Note, however, that the other earthquakes were not deficient in high-frequency energy. Kovach (1974) calculated rupture velocities of 100-300 m/s, which are slow for regular earthquakes, but are similar to tsunami wave speed. If the Green Canyon earthquake was caused by oil operations, then it and future such earthquakes may have a limited magnitude, which is related to local operations. If, however, the earthquake is related to heterogeneous mechanical properties of the sediment, a larger earthquake and a tsunami can potentially be generated.

Other earthquakes

The size of the November 10, 2006 Mw 5.8 earthquake was a surprise, because the earthquake magnitude of historical seismicity in the Gulf of Mexico is typically less than 4.5-5 (Frohlich, 1982 , Figure 5-3). This thrust earthquake (with possible strike slip) occurred west of the west Florida escarpment where there is no known tectonic feature. However, Salvador (1991), proposed there to have been a zone of transtension during the early opening of the Gulf, which was oriented parallel to the West Florida escarpment. An alternative cause for this earthquake may therefore be reactivation by intraplate stresses.

North Panama Deformation Belt 9-12ºN, 83ºW-77ºW

Summary

The largest segment of the North Panama Deformation Belt is oriented between 60°-77°. The 1882 Panama earthquake appears to have ruptured at least 3/4 of the available length of the convergence zone, and was estimated to have a magnitude of 8 (Mendoza and Nishenko, 1989). While there was significant tsunami damage locally, there were no reports from the Gulf of Mexico of a tsunami from this earthquake (Mendoza and Nishenko, 1989). The low convergent rate (7-11 mm/y, (Trenkamp*, et al.*, 2002)) across the North Panama Deformation Belt supports long recurrence interval for large earthquakes.

Previous tsunamis

A tsunami flooded San Blas islands and the northern coast of Panama (Figure 5-1) and killed 65 people on 09/07/1882 following an offshore earthquake at about 10°N, 78°W (Mendoza and Nishenko, 1989). Mendoza and Nishenko (1989) isoseismal map (Figure 5-6) suggests that rupture occurred along almost the entire segment between longitude 80.3°W-77.8°W. Eyewitnesses report water withdrawal before flooding. The tide gauge in Colon at the northern end of Panama Canal reported a level change of only 62 cm. The Jamaica-Panama underwater cable broke (perhaps indicating a submarine slide). The authors estimated the earthquake to be ~M=8, an increase from previous estimates (Mendoza and Nishenko, 1989).

Plafker and Ward (1992) reported an M_s=7.5 earthquake on 04/22/1991 at 9.74N 83.1W (on land), which caused uplift along 135 km of the Caribbean coast in southern Costa Rica. This earthquake was reported by the Harvard CMT catalog with location: 10.10N, 82.77W, depth: 15 km, and M_w= 7.6. It also caused a damaging tsunami, which was recorded by a tide gauge in St. Croix (Lander, *et al.*, 2002). Plafker and Ward (1992) best fit parameters of the ruptured fault from seismic and geodetic data are: thrust fault, striking between 105-120°, dipping at 30°, fault dimensions: 40 km wide and 80 km long, Their estimated recurrence time on this fault is 200-1100 y.

The parameters for this earthquake are given as:

ref.	*strike*	*dip*	*rake*
1	103°	25°	58° (oblique thrust and left-lateral)
2	123° (91°-138°)	32° (16°-39°)	89° (69°-96°)
3	107±5°	21°±10°	56°±11°

Information is based on the Harvard CMT catalog, Tajima and Kikuchi (1995), and Goes, *et al.* (1993).

Other earthquakes

Within the central and eastern sections of this deformation belt, the USGS catalog lists 10 focal plane solutions, 6 of them, normal mechanisms, 4 reverse mechanisms. Their magnitudes range between 5.4-6.3. The parameters for the 4 reverse focal mechanisms are:

lat	*long*	*strike*	*dip*	*rake*	
9.7	79.7	238	70	31	(LL+ compression facing NW)
10.2	80.0	35	45	57	(compression+LL facing SE)
10.3	79.7	72	54	56	(compression+LL facing ESE)
9.0	77.4	75	26	20	(LL+compression facing ESE);

The USGS catalog lists the following earthquakes with reverse mechanism along the westernmost section (Costa Rica):

lat	*long*	*strike*	*dip*	*rake*	
9.88	-82.34	138	21	105	(compression+RL facing SW)
9.54	-82.64	151	9	108	(compression+RL facing SW)
9.65	-82.47	155	34	135	(compression+RL facing SW)

9.643	-82.3	346	34	134	(compression+RLfacing ENE)
9.91	-82.1	320	32	126	(compression+RL facing ENE)
9.69	-82.46	313	26	94	(compression facing NE)
10.1	-83.07	143	46	112	(compression+RL facing SW)

Relative motion from GPS

The relative motion between Isla San Andres (east of Nicaragua), which is considered representative of Caribbean plate motion, and Panama is 11 mm/y in azimuth 180° (Kellogg, *et al.*, 1995). Others suggest a rate of relative motion of 7±2 mm/y in direction southwest between Isla San Andres and Costa Rica and westernmost Panama (Trenkamp, *et al.*, 2002).

Northern South America Convergent Zone, 11.5°-14°N, 77°W-64°W

Summary

It is difficult to evaluate the potential tsunami hazard from the convergence zone along the north coast of South America. Although there is shortening in the SE direction between the Caribbean and South American plates, much of the shortening is probably absorbed by deformation inland within and at the boundaries of the North Andes and Maracaibo blocks (Figures 5-1, 5-7). The amount of offshore deformation is not well known. There have been only two moderate earthquakes with reverse mechanisms during the past 40 years in the offshore areas. Shallow compressional deformation is more intense west of Aruba than to the east and reaches a maximum around longitude 75°W. There is no Holocene deformation west of 76.5°W on the north/south oriented subduction segment. The shape of the subduction zone under the northwest corner of South America is in dispute, with pieces of Nazca plate entering from the west and Caribbean plate perhaps also entering from the west as well as from the north. Some workers suggest that the Caribbean plate has a dip of 17°, but the lack of seismicity does not enable a good definition of the slab. There are no historical tsunamis associated with the convergent zone.

East of 68°W, 80% of the 2 cm/y motion between Caribbean and South American plates is confined to an 80-km narrow shear zone centered around the El Pilar strike-slip fault. The expected recurrence rate there is 150-200 y with slip magnitude of 3 - 4 m. There have been several devastating tsunamis associated with the El-Pilar fault in the past 500 years, but in our opinion, those are due to local compression or submarine landslides along the strike-slip fault. Between the El-Pilar fault and Aruba, the deformation zone widens but shows signs of extension, not compression.

As a worse case scenario (probably highly unlikely), we suggest thrust faulting along a 550 km long segment of the convergent zone between 72.5°-76.5°W oriented at N53°W with a dip of 17° and an unknown downdip length and slip. Another thrust fault could exist north of Oca fault (Figure 5-1), but motion there should be fairly oblique.

Surface deformation offshore

NE-facing normal faults are found around Aruba, Bonaire, and Curacao (Taboada, *et al.*, 2000). Seismic reflection profiles perpendicular to the margin show an apron of undeformed sediments migrating northward across an older deformed belt (ibid.). The deformation zone is narrow (~45 km) and shows mild compression north of Bonaire, and the sediments of the Venezuela basin entering the trench appear sagged, as if under tension. Deformation is getting more intense and its frontal edge is steeper north of Aruba and Guajira peninsula (~71.5°W). Deformation reaches maximum intensity along the NW corner of the convergence zone, and becomes less intense farther south (Ladd, *et al.*, 1984). No deformation is observed in offshore Holocene sediments of western Columbia (from Cartagena all the way south (Duque-Caro, 1984)).

Previous tsunamis

01/17/1929 – A tsunami destroyed Cumana, Venezuela (South of Isla Margarita) following an Ms=6.9 earthquake (*Lander, et al.*, 2002). All other historical tsunamis appear to concentrate in the Gulf of Cariaco, Isla Margarita, and the Gulf of Paria, (Lander, *et al.*, 2002) where the Pilar fault has a strike slip motion.

Earthquakes

Only four earthquakes are listed in the Harvard CMT catalog between 1976 and 2007 offshore NW South America. All four earthquakes were located east of 72.8°W and show normal fault mechanisms. Two earthquake with reverse mechanisms were quoted by Perez *et al.*, (1997):

03/12/1968	13.15°N	72.3°W	depth 58 km	Mb=5.3
04/28/1978	11.99°N	72.54°W	depth 62 km	Mb=5.2

Earthquakes around Aruba, Bonaire, and Curacao, show right-lateral strike slip. Seismicity is shallower than 50 km deep between the northern edge of the deformation zone and the coast (200 km east of 73.5W) (Figure 5-7). The slab has a sharp corner at 73.5°W-75°W (Colmenares and Zoback, 2003).

Large historic earthquakes occurred along the coast on the El Pilar strike-slip fault system which connects to the Bocono fault system which continues inland to the southwest (McCann and Pennington, 1990). The Oca fault, a westerly continuation of the El Pilar fault (Figure 5-1) has not been active historically (Figure 5-7). There is a disagreement whether the Caribbean actually subducts under northern South America, because of lack of shallow seismicity (McCann and Pennington, 1990).

Relative block motion from GPS

The relative motion between the Caribbean plate (as measured on San Andres Island) and stable South America is 20 mm/y in direction 104° (Corredor, 2003). Perez, *et al.* (2001) and Weber, *et al.* (2001) showed that east of 68°W, 80% of the motion between Caribbean and South American plates is confined to an 80-km narrow shear zone centered around the El Pilar strike-slip fault. The expected recurrence rate of earthquakes there is estimated to be 150-200 y with a slip magnitude of 3-4 m (Perez, *et al.*, 2001). The deformation zone widens to the west. The region south of Aruba and north of Bonoco fault (the Falcon Basin) moves at 15 mm/y at N82°E, implying a very small component of N-S compression (Perez, *et al.*, 2001).

The relative block motion Caribbean (San Andres) – North Andes Block (as represented by the Bogota, Columbia station) is 14±2 mm/y in a southeast direction (Trenkamp, *et al.*, 2002). However 2/3 of this motion may be comprised of internal deformation of the north Andean block on shore, as evidenced by the fact that relative motion between the Caribbean and the stable South America plate is 20 mm/y, while the relative motion between Cartagena, Columbia, and stable South America is 14 mm/y at almost the same direction (Trenkamp, *et al.*, 2002). Trenkamp, *et al.*, (2002) suggested that the North Andes block escapes to the NE along the Bonoco Fault at a rate of 6 mm/y.

Stress indicators

Colmenares and Zoback (2003) show evidence for maximum horizontal compression in a southeast direction on land west of Maracaibo basin (Figure 5-7).

The deep structure of the convergent zone

The Caribbean subduction zone under western Columbia is suggested to be very steep. However, the shape of subduction zones under northern South America is in dispute, with various authors proposing that pieces of Nazca plate enter from west and the Caribbean plate perhaps entering from west as well as from north (Malave and Suarez, 1995; van der Hilst and Mann, 1994). van der Hilst and Mann (1994) proposed an average dip of 17° for Caribbean under northwest S. America.

Western Cayman Trough

The Cayman Trough is a 1400-km-long and about 100-km-wide oceanic depression with a maximum depth of 7100 m that extends from southeast Cuba in the east to Honduras and Guatemala in the west (Figure 5-1, 5-2) (ten Brink et al., 2002). The trough is a tectonic plate boundary between the North American plate, which moves westward with respect to the Caribbean plate at a rate of 15-20 mm/y. As a result of this differential motion, large earthquakes sometimes take place along the plate boundary. A recent (05/28/2009) magnitude 7.2 earthquake along the western end of the trough, which is 1500 km from the northern Gulf of Mexico, allows us to evaluate the tsunami potential from this plate boundary (Figure 5-8). The earthquake rupture was a left-lateral strike-slip with the following parameters strike= 64 dip= 67 rake= 0 and depth= 10 km. There was no evidence for a tsunami in the Gulf of Mexico. Note that tsunami propagation models predict very little

energy crosses the Yucatan Channel (between Cuba and the Yucatan Peninsula) into the Gulf of Mexico. Local tsunami warning was broadcast by the NOAA Pacific Tsunami Warning Center but was cancelled. This is because strike-slip faults do not generate large tsunami waves due to their mainly horizontal rupture (Figure 5-9).

Figures

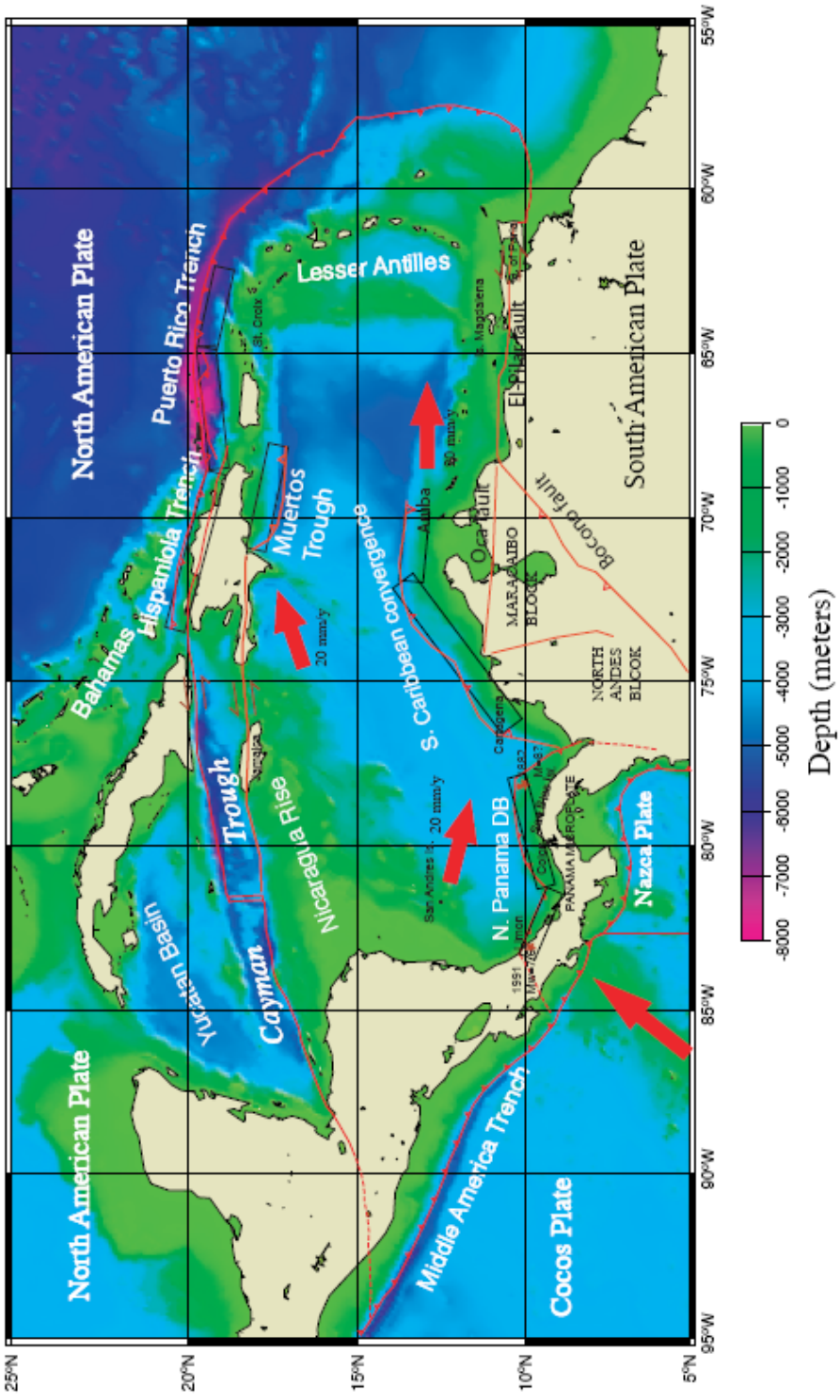

Figure 5-1: The Caribbean plate boundary and its tectonic elements.

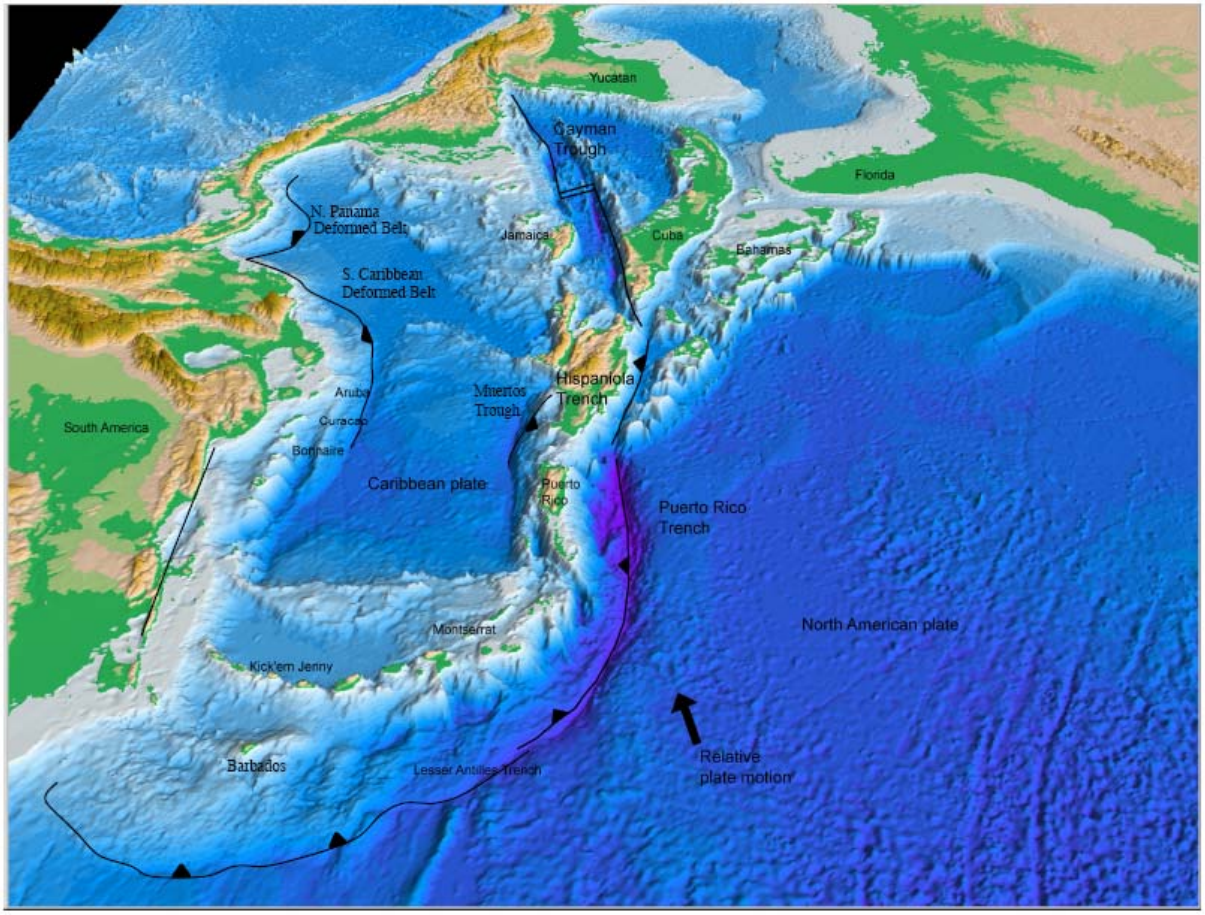

Figure 5-2: Perspective view of the tectonic elements in the Caribbean plate and seafloor topography.

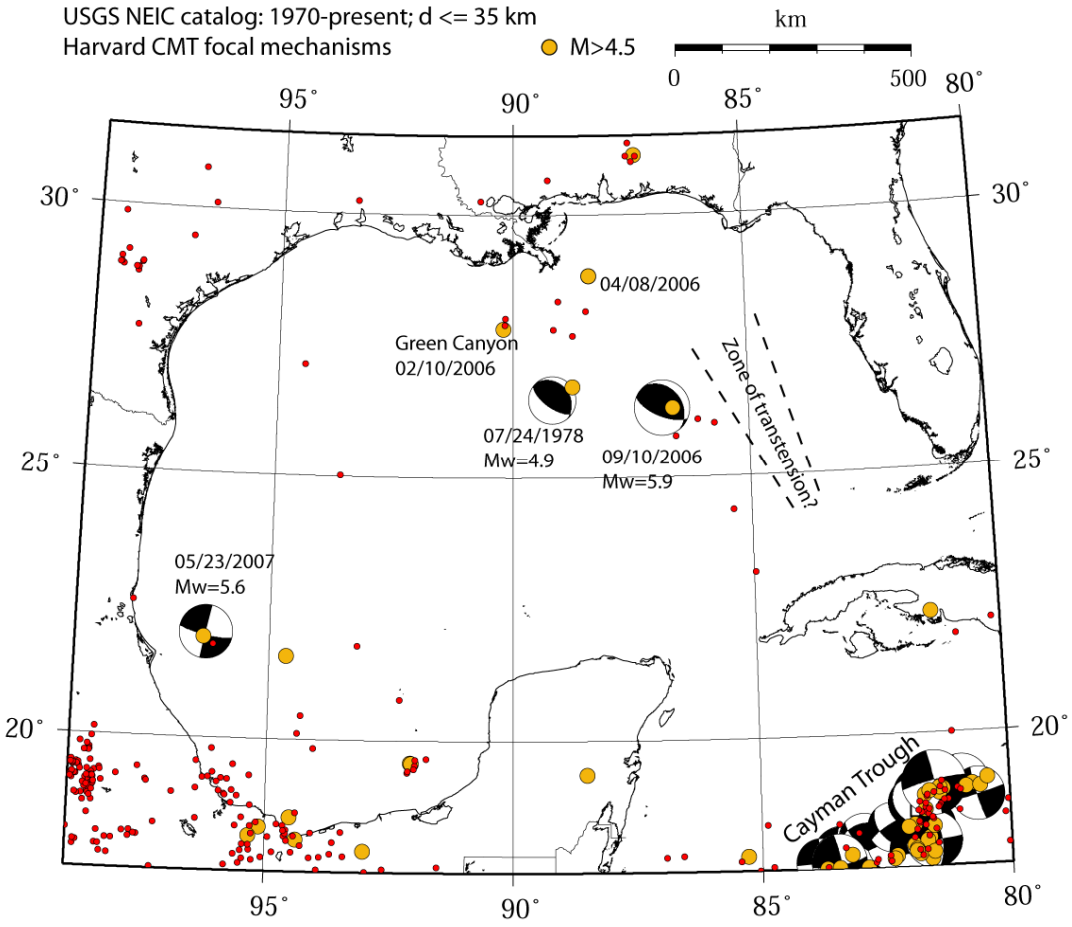

Figure 5-3: Historical seismicity data for the Gulf of Mexico, 1970 to present.

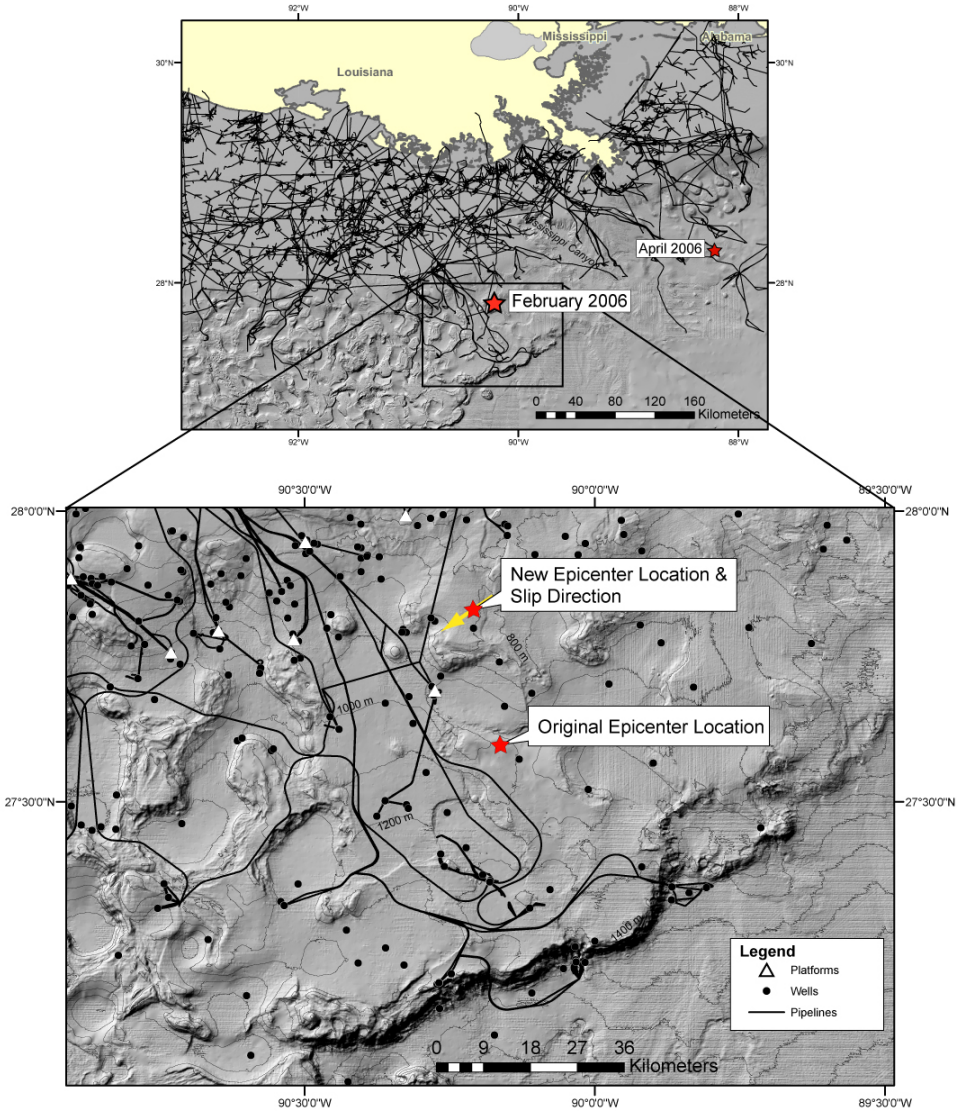

Figure 5-4: Multibeam bathymetry near the February 10, 2006 Green Canyon event in the Gulf of Mexico that was seismically recorded.

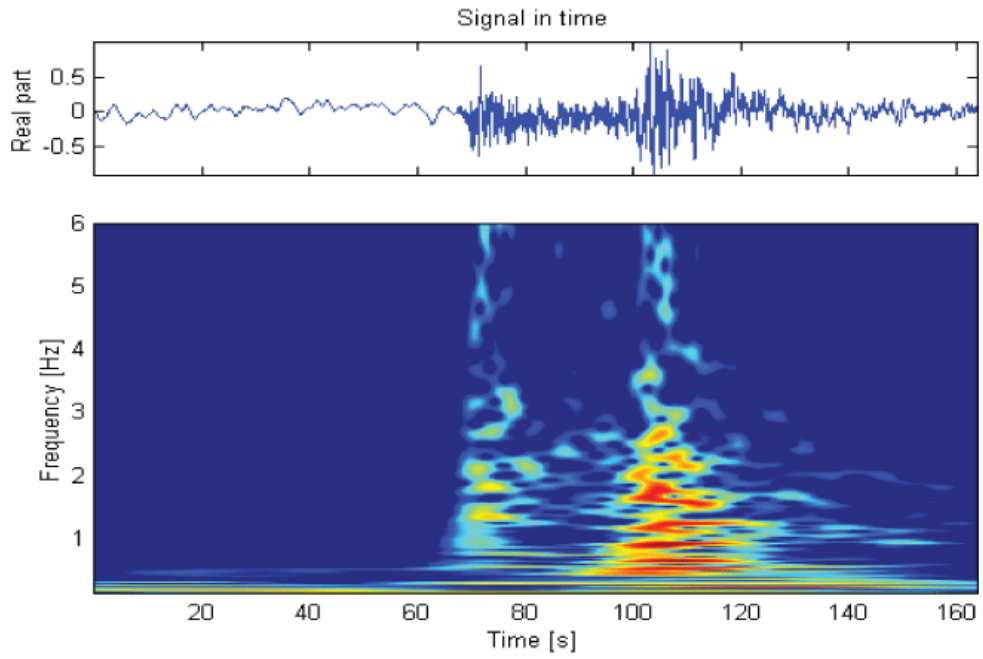

Figure 5-5 A: Seismogram (top) and spectrogram of a typical shallow earthquake (M 3.9 January 27, 2006 Denali earthquake)

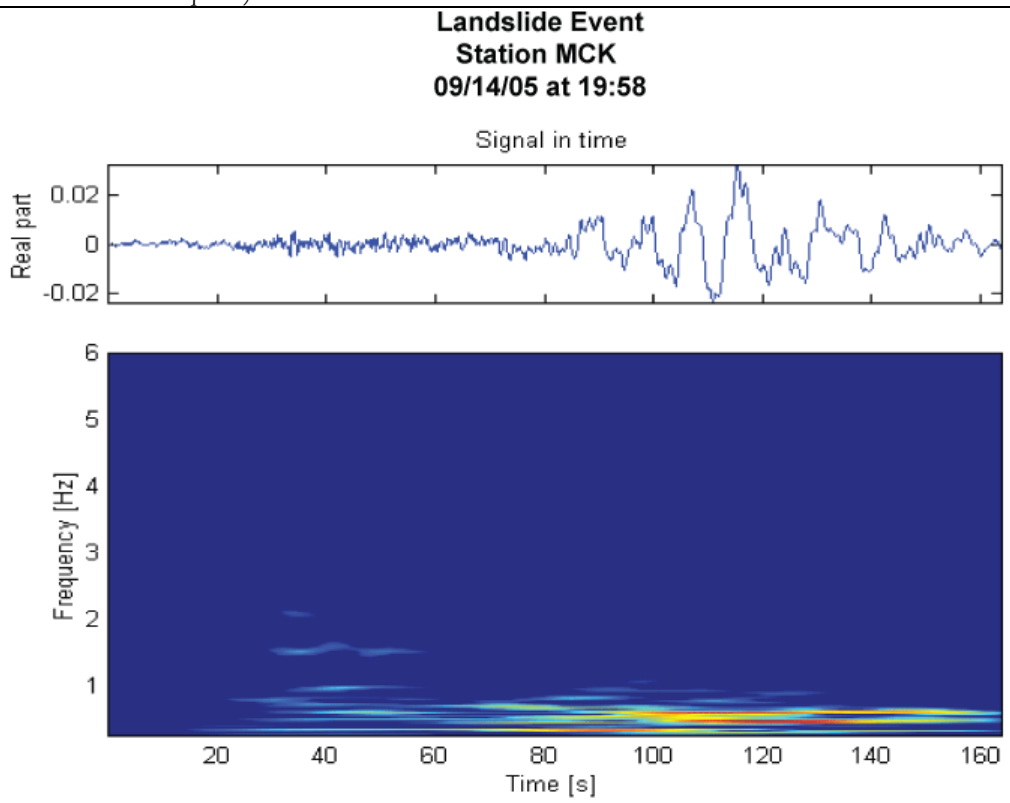

Figure 5-5 B: Seismogram (top) and spectrogram of a known subaerial landslide in SE Alaska. MCK: McKinley Park seismic station.

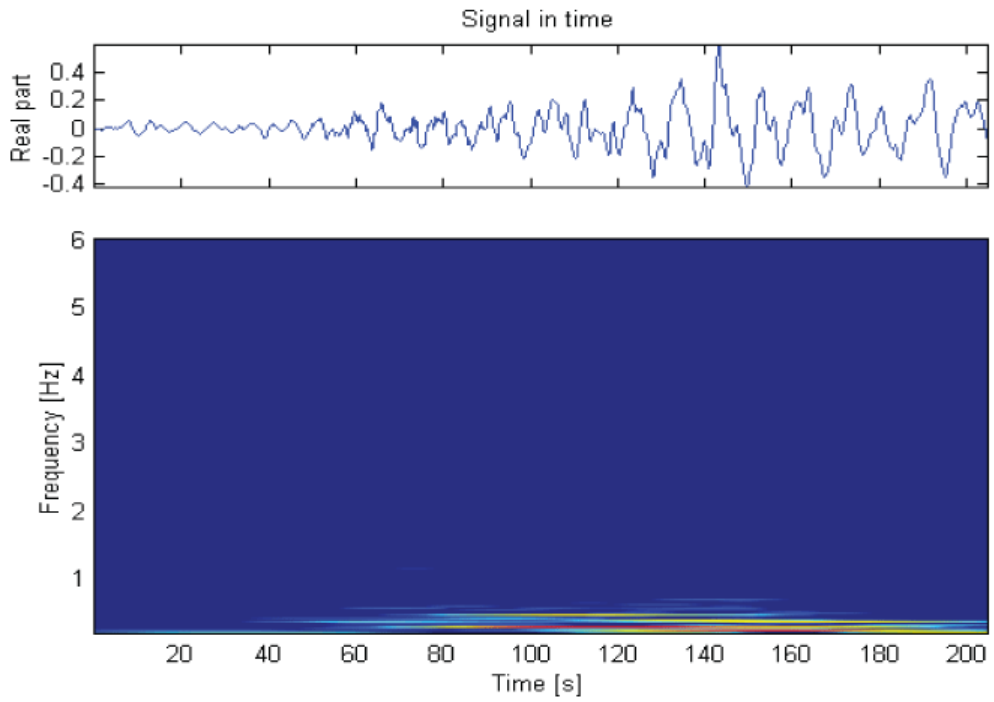

Figure 5-5 C: Seismogram (top) and spectrogram of the February 10, 2006 Gulf of Mexico Green Canyon event (see Figure 3-6 for location). Note the similarity with Figure 3-8 (landslide) and the dissimilarity with Figure 3-7 (earthquake).

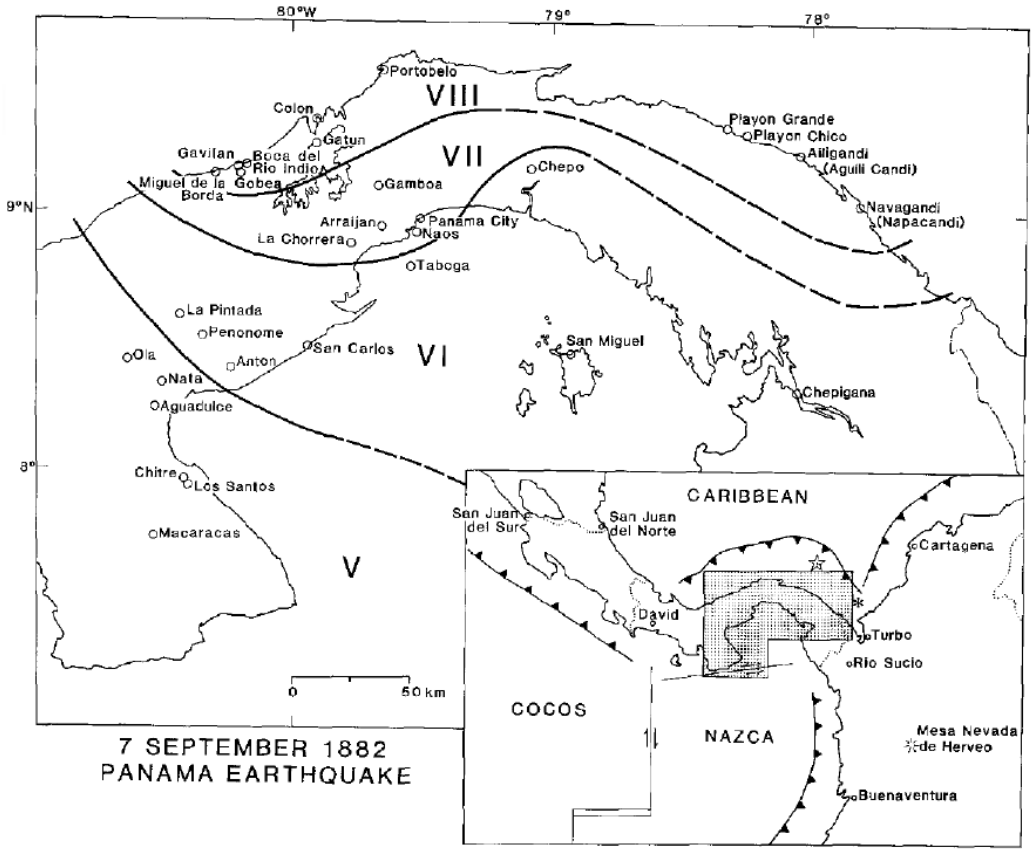

Figure 5-6: Isoseismal map of the 1882 earthquake in the North Panama Deformation Belt (from Mendoza and Nishenko, 1989). The star in the inset is their preferred epicenter.

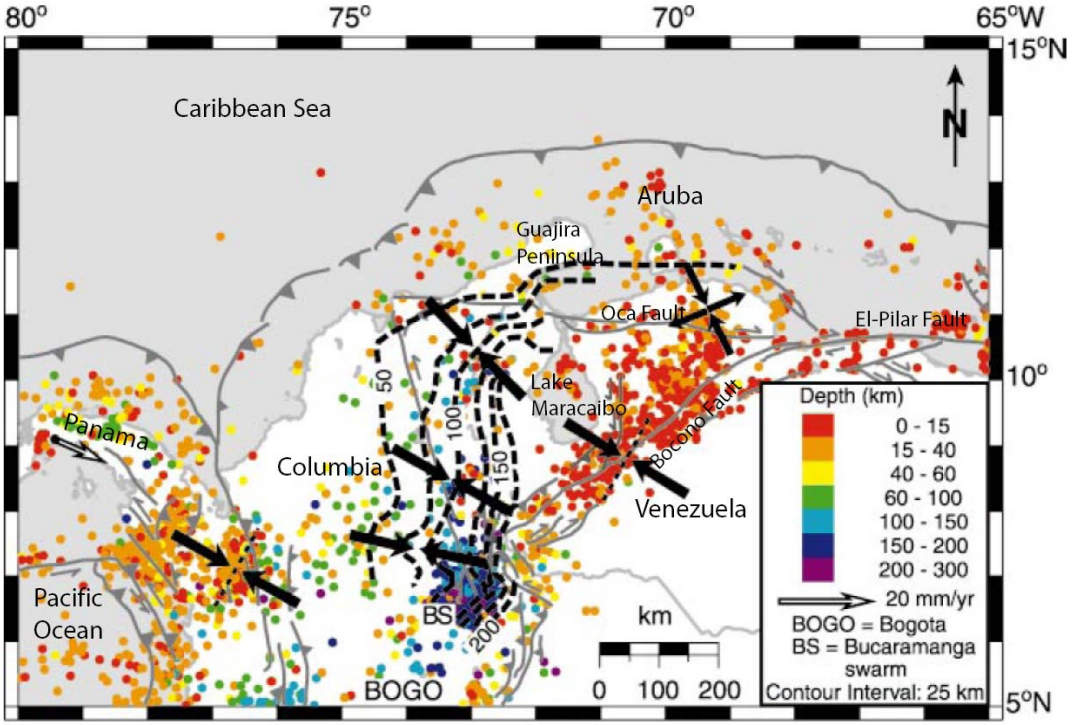

Figure 5-7: Depth of seismicity and generalized stress directions (from Colmenares and Zoback, 2003). Contour lines depths in km to top surface of inclined seismic zones.

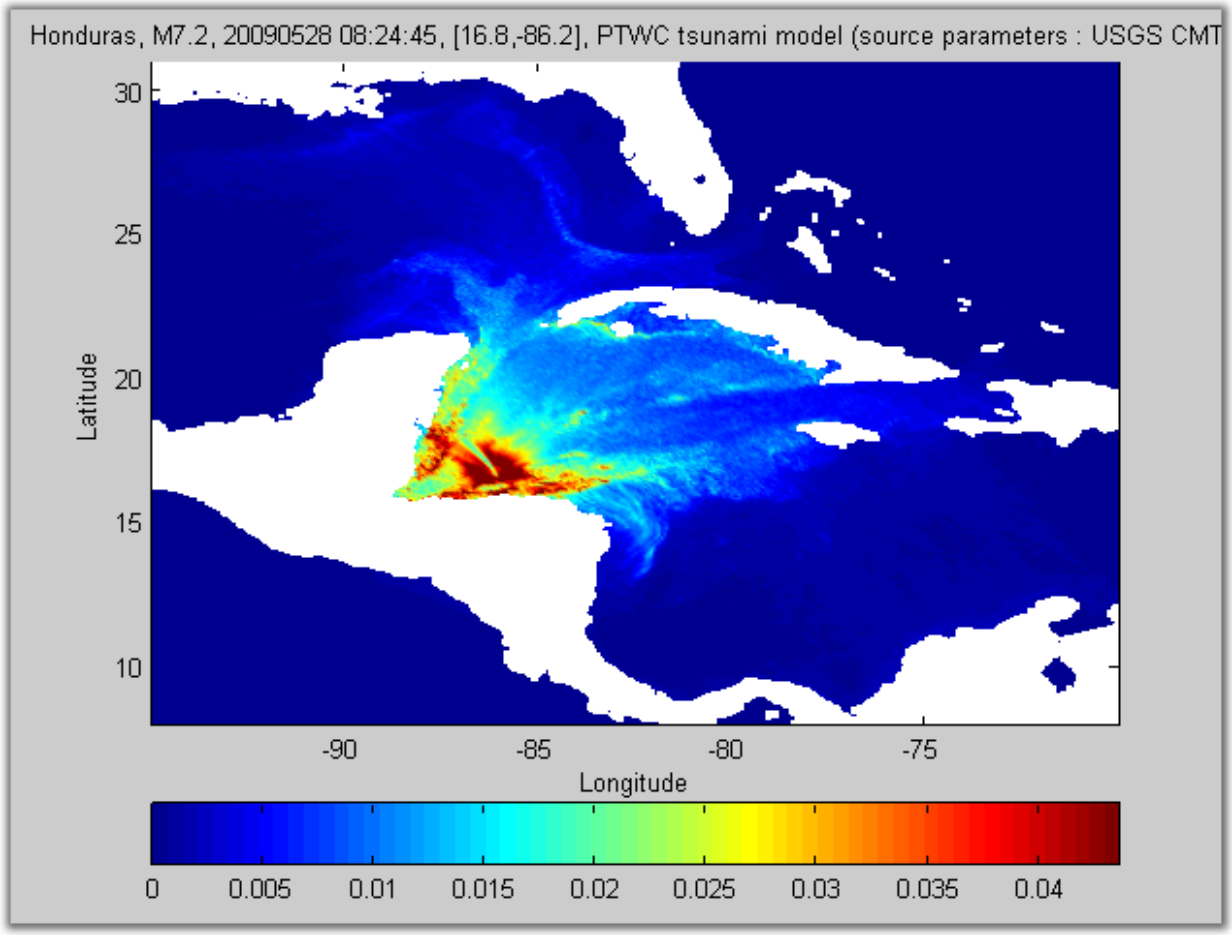

Figure 5-8: Tsunami propagation from the source. Map is an energy map (maximum range is 15 cm in the open ocean, but only shown to 5 cm to show details). (From e-mail 05/29/2009 to tsunami Bulletin board by Dailin Wang, NOAA)

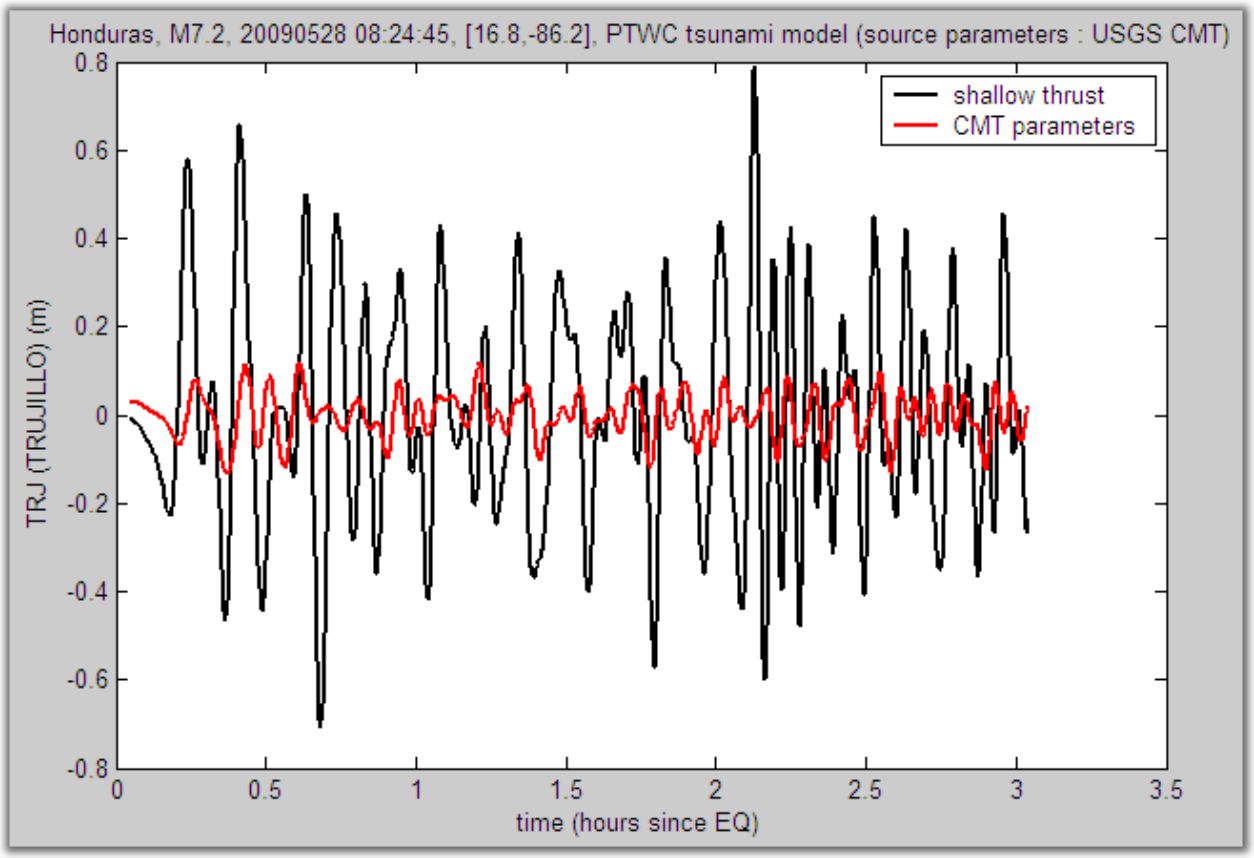

Figure 5-9: Time series plot are two runs (the red curve is a run with USGS CMT parameters: strike slip; the black curve is a run assuming shallow thrust, strike parallel to the coast). Note the dramatic differences between the two, underlining the importance of source parameters." (From e-mail 05/29/2009 to tsunami Bulletin board by Dailin Wang, NOAA)

References

Barkan, R., ten Brink, U.S., and Lin, J., 2009, The source of the 1755 Lisbon earthquake: Implications for tsunami hazard to the U.S. Atlantic coast: *Marine Geology, v. 264,* p. 109-122.

Colmenares, L., and Zoback, M. D., 2003, Stress field and seismotectonics of northern South America: *Geology, v. 31*, p. 721-724.

Corredor, F., 2003, Seismic strain rates and distributed continental deformation in the Northern Andes and three-dimensional seismotectonics of northwestern South America: *Tectonophysics, v. 372*, p. 147-166.

Dellinger, J., Blum. J., Nettles. M., and Peel, F., 2009, The 10 February 2006 "Green Canyon" earthquake: a case history of an unusual seismic event: *SEG Expanded Abstracts, v. 28*.

Dewey, J.W. and Dellinger, J.A., 2008, Location of the Green Canyon (offshore southern Louisiana) seismic event of February 10, 2006: *U.S. Geological Survey, Open-File Report 2008-1184,* 30 p.

Duque-Caro, H., 1984, Structural style, diapirism, and accretionary episodes of the Sinu-San Jacinto terrane, southwestern Caribbean borderland: *Memoir - Geological Society of America, v. 162*, p. 303-316.

Frohlich C., 1982, Seismicity of the central Gulf of Mexico: *Geology, v. 10,* p. 103-106.

Gangopadhyay, A. and Sen, M.K., 2008, A possible mechanism for the spatial distribution of seismicity in northern Gulf of Mexico: *Geophysical Journal International, v. 175,* p. 1141-1153.

Goes, S. D. B., Velasco, A. A., Schwartz, S. Y., and Lay, T., 1993, The April 22, 1991, Valle de la Estrella, Costa Rica (M (sub w) = 7.7) earthquake and its tectonic implications; a broadband seismic study: *Journal of Geophysical Research, v. 98*, p. 8127-8142.

Kanamori, H. and Given, J.W., 1982, Analysis of long-period waves excited by the May 18, 1980, eruption of Mount St. Helens; a terrestrial monopole? : *Journal of Geophysical Research, v. 87,* p. 5422-5432.

Kellogg, J. N., Vega, V., Stallings, T. C., Aiken, C. L. V., and Kellogg, J. N., 1995, Tectonic development of Panama, Costa Rica, and the Colombian Andes; constraints from Global Positioning System geodetic studies and gravity: *Special Paper - Geological Society of America, v. 295*, p. 75-90.

Kovach R.L., 1974, Source mechanisms for Wilmington Oil Field, California, subsidence earthquakes: Bulletin of the Seismological Society of America, v. 64, p. 699-711.

Ladd, J. W., Truchan, M., Talwani, M., Stoffa, P. L., Buhl, P., Houtz, R., Mauffret, A., and Westbrook, G. K., 1984, Seismic reflection profiles across the southern margin of the Caribbean: *Memoir - Geological Society of America, v. 162*, p. 153-159.

Lander, J. F., Whiteside, L. S., and Lockridge, P. A., 2002, A brief history of tsunamis in the Caribbean Sea: *Science of Tusnami Hazards, v. 20*, p. 57-94.

Malave, G., and Suarez, G., 1995, Intermediate-depth seismicity in northern Colombia and western Venezuela and its relationship to Caribbean Plate subduction: *Tectonics, v. 14*, p. 617-628.

McCann, W. R., and Pennington, W. D., 1990, Seismicity, large earthquakes, and the margin of the Caribbean Plate, Geol. Soc. Am. Boulder CO United States (USA).

Mendoza, C., and Nishenko, S. P., 1989, The North Panama earthquake of 7 September 1882; evidence for active underthrusting: *Bulletin of the Seismological Society of America, v. 79*, p. 1264-1269.

Nettles, M., 2007, Analysis of the 10 February 2006 Gulf of Mexico earthquake from global and regional seismic data, in 2007 Offshore Technology conference, abstract #19099, Society of Petroleum Engineers. doi: 10.4043/19099-MS.

Ottenmöller, L, Neilsen, H.H., Atakan, K., Braunmiller, J., and Havskov, J.,, 2005, The 7 May 2001 induced seismic event in the Ekofisk oil field, North Sea: *Journal of Geophysical Research, v. 110,* doi:10.1029/2004JB003374.

Perez, O. J., Bilham, R., Bendick, R., Velandia, J. R., Hernandez, N., Moncayo, C., Hoyer, M., and Kozuch, M., 2001, Velocity field across the southern Caribbean plate boundary and estimates of Caribbean/South-American plate motion using GPS geodesy 1994-2000: *Geophysical Research Letters, v. 28*, p. 2987-2990.

Perez, O. J., Jaimes, M. A., and Garciacaro, E., 1997, Microseismicity evidence for subduction of the Caribbean Plate beneath the South American Plate in northwestern Venezuela: *Journal of Geophysical Research, v. 102*, p. 17,875-817,882.

Plafker, G., and Ward S. N., 1992, Backarc thrust faulting and tectonic uplift along the Caribbean Sea coast during the April 22, 1991 Costa Rica earthquake: *Tectonics, v. 11*, p. 709-718.

Salvador, A., 1991, Origin and development of the Gulf of Mexico basin: *in* Salvador, A. (Editor), The Geology of North America, Vol. J., The Gulf of Mexico Basin, Geological Society of America, Boulder, CO, p. 389-444.

Taboada, A., Rivera, L. A., Fuenzalida, A., Cisternas, A., Philip, H., Bijwaard, H., Olaya, J., and Rivera, C., 2000, Geodynamics of the Northern Andes; subductions and intracontinental deformation (Colombia): *Tectonics, v. 19*, p. 787-813.

Tajima, F., and Kikuchi, M., 1995, Tectonic implications of the seismic ruptures associated with the 1983 and 1991 Costa Rica earthquakes: *Special Paper - Geological Society of America, v. 295*, p. 327-340.

ten Brink, U.S., Coleman, D. F., Dillon, W.P., The nature of the crust under Cayman Trough from gravity: *Marine and Petroleum Geology, v. 19,* p. 971-987.

Trenkamp, R., Kellogg, J. N., Freymueller, J. T., and Mora, H. P., 2002, Wide plate margin deformation, southern Central America and northwestern South America, CASA GPS observations: *Journal of South American Earth Sciences, v. 15*, p. 157-171.

van der Hilst, R., and Mann, P., 1994, Tectonic implications of tomographic images of subducted lithosphere beneath northwestern South America: *Geology, v. 22*, p. 451-454.

Weber, J. C., *et al.*, 2001, GPS estimate of relative motion between the Caribbean and South American plates, and geologic implications for Trinidad and Venezuela: *Geology, v. 29*, p. 75-78.

Chapter 6: Regional Tsunami Propagation Patterns from Caribbean Earthquakes

Tsunami propagation from large-magnitude earthquakes in the Caribbean is calculated in order to estimate tsunami amplitudes offshore U.S. Atlantic and Gulf of Mexico coasts. Sources for the tsunami calculations are discussed previously in Chapter 4. This is a preliminary effort for the purpose of determining the relative severity among tsunamis from different sources and complements recent work by Knight (2006). A range of tsunami amplitudes is determined based on natural variations in slip distribution patterns expected for large magnitude earthquakes along plate boundaries in the Caribbean. This work predicts maximum wave amplitudes in 250 m of water at the shelf edge and does not predict runup nor propagation characteristics across the continental shelf. Therefore, the wave positive amplitude is much smaller (N=1/3) than expected to be encountered at the shoreline.

Method

Large magnitude earthquakes in the Caribbean (Figure 6-1) were specified by determining a maximum rupture length along the following plate boundary segments (using the classification scheme by Bird, 2003): (1) west Cayman oceanic transform fault (OTF), also known as Swan Island Fault, (2) east Cayman (OTF), also known as Oriente Fault, (3) northern Puerto Rico/Lesser Antilles subduction zone (SUB), (4) north Panama deformation belt, classified by Bird (2003) as an oceanic convergent boundary (OCB), and (5) the north coast of South America convergence zone classified by Bird (2003) as a subduction zone (SUB) (termed the north Venezuela subduction zone below). This classification scheme will be used to assess the probability of earthquakes along these fault zones in a later study.

Other faults in the Caribbean that can generate destructive local tsunamis, but unlikely to generate far-field tsunamis such as thrust faulting in the Muertos Trough and normal faulting in the Mona Passage were not modeled in this study. For the transform faults, the moment magnitude was estimated from rupture length using the Wells and Coppersmith (1994) empirical relationships. From this relationship and an estimate of the fault width (seismogenic thickness) from Bird and Kagan (2004), an average slip was assigned to each fault, assuming a shear modulus of 35 GPa. Fault dip and rake were estimated from analysis

of past focal mechanisms from the Global CMT database (http://www.globalcmt.org/). For the subduction boundary faults, geometric parameters were taken from regional studies described previously in the report and in prior publications (*e.g.*, ten Brink and Lin, 2004). Scaling of average slip from rupture length was taken from compiled databases of source parameters for subduction interplate thrust earthquakes (Lay *et al.*, 1982; Geist, 2002). Uncertainty caused by variations in slip distribution patterns is assessed by computing 100 different slip distributions that all have nearly the same average slip and slip spectrum (Herrero and Bernard, 1994; Geist, 2002; Geist *et al.*, 2007). A summary of the range of magnitude and average slip for each fault is given in Table 6-1.

Initial conditions for the propagation model are specified by the coseismic displacement of the seafloor. This includes primarily the vertical component of displacement. In addition, horizontal displacement in regions of steep bathymetric gradient will also contribute to vertical displacement of the water column in a manner described by Tanioka and Satake (1996). Since this component of the initial wavefield depends on the bathymetric gradient field near the source region, it is relatively incoherent compared to the primary component of the initial wavefield from vertical coseismic displacement. The transform faults (OTF) are much less efficient at generating tsunami waves (Figure 6-1a, b) than the thrust faults along subduction zones (SUB) and oceanic convergent boundaries (OCB) (Figure 6-1c, d, e).

Tsunami propagation was modeled using the linear long-wave equation, numerically implemented with a leap-frog, finite-difference algorithm. Only deep-ocean tsunami propagation is modeled, where linear theory is most applicable. Propagation across the continental shelf (specified by water depth less than 250 m) and runup are not modeled. As a very rough approximation, runup is approximately 3 times the tsunami amplitude at 250 m water depth, accounting for shoaling and runup amplification (Shuto, 1991; Satake, 1995, 2002), but not including energy dissipation from geometric spreading, bottom friction, and non-linear attenuation that is evident in the simulations of the Currituck landslide tsunami offshore Virginia, USA (Locat, 2009). It is unclear whether the latter two dissipation mechanisms are as significant for far-field seismogenic tsunamis as they are for landslide tsunamis. Radiation boundary conditions are specified at the open-ocean boundaries, whereas reflection boundary conditions are specified at the 250 m isobath. The spatial grid size for the simulations is 2 arc-minutes and the time step is 8 s, which satisfies the Courant-Friedrichs-Lewy stability criterion (Satake, 2002). Total propagation time for each simulation is 4.4-6.6 hours, which is sufficient to capture the first few waves at the 250 m isobath within the model domain.

Results

For each fault, results from the simulation are shown in Figure 6-1 through Figure 6-3. Figure 6-1 shows the maximum tsunami amplitude in the open ocean for one of the 100 simulations for each source. Figure 6-2 shows the range of peak offshore tsunami amplitudes from all 100 simulations at the 250 m isobath for a latitudinal profile in the Gulf of Mexico (Figure 6-2). Figure 6-3 shows the range in tsunami amplitudes as a time series (*i.e.*, marigrams) for selected offshore locations in the Gulf of Mexico. Tsunami characteristic for coastal regions will be different, because of nearshore propagation and runup effects.

In terms of overall severity, large earthquakes along the northern Puerto Rico subduction zone generate the largest tsunamis propagating toward the U.S. Atlantic coast (Figure 6-1c).

For the Gulf Coast, the largest tsunamis are generated by large earthquakes along the north Venezuela subduction zone. The absolute tsunami amplitudes are highly dependent, however, on the magnitude specified for each of these fault zones. Distributions of earthquake magnitudes for these fault zones will be discussed in a future study. In general, these results are consistent with the findings of Knight (2006), where the far-field tsunamis generated from earthquakes located beneath the Caribbean Sea are higher along the Gulf coast than the Atlantic coast because of dissipation through the Greater Antilles islands. Conversely, tsunamis generated from earthquakes north of the Greater Antilles are higher along the Atlantic coast than the Gulf coast.

In the Gulf of Mexico (Figure 6-2), tsunami amplitudes are higher where the shelf edge is approximately normal to the incidence of tsunami waves propagating from the south (*i.e.*, between ~83-85°W and ~87.5-88.5°W). The range in tsunami amplitudes caused by variations in slip distribution patterns is dependent on the propagation path distance from the source to the shelf edge. This distance dependence of the resulting tsunami amplitude variability is also evident on the synthetic marigrams (graph of tsunami amplitude as a function of time) (Figure 6-3). In addition, for most cases except for the northern Puerto Rico subduction zone scenario tsunami, the onset of the tsunami at the 6 marigram stations can be characterized as emergent (*i.e.*, initial tsunami waves are smaller than later ones), primarily because of obstructed propagation paths. In general, spectral characteristics of tsunami marigrams is dependent on source characteristics, propagation path, and site response (Rabinovich, 1997).

To determine the tsunami characteristic along the coast from these sources, a more refined hydrodynamic model needs to be employed. For example, the Method of Splitting Tsunami (MOST) model (Titov and Synolakis, 1996; Titov and González, 1997; Titov and Synolakis, 1998) is specifically designed to determine propagation and runup characteristics for regional and far-field tsunamis. Source characterizations similar to what is being used for the tsunami forecasting system (Titov *et al.*, 2005) should be adequate for determining tsunami characteristics along the Gulf coast.

For comparative purposes, we re-compute here the offshore tsunami water levels for earthquake scenarios (3) and (5) using the COMCOT model. The COMCOT model is more accurate than the model used in ten Brink et al. (2008) since it includes non-linear terms in the propagation equations (hence, the computations can be carried into shallower water), a moving boundary condition at the shoreline, and is computed in spherical coordinates. Bottom friction is also included, but is set at a low, conservative value ($f = 10^{-4}$) in this case. Figures 6-4 and 6-5 show the peak tsunami amplitude for M~9 earthquakes along the northern Caribbean subduction zone and northern South America convergent zone, respectively.

These results confirm that tsunami amplitudes from distant Caribbean earthquakes are less than 1.0 m along the Gulf Coast of the U.S. Tsunami amplitudes from earthquakes along the Azores-Gibraltar oceanic convergence boundary are also likely to be less than 1 m in the Gulf of Mexico (Mader, 2001; Barkan *et al.*, 2009).

Table 6-1: Source parameters and range of average slip and moment magnitudes of earthquakes from which tsunami simulations were computed.

Fault #*	Name	Type†	Length (km)	Width (km)	strike (°)	dip (°)	rake (°)	Avg. Slip-low (m)	Avg. Slip-high (m)	M_w (low)	M_w (high)
1	W. Cayman	OTF	746	15	N73E	83N	185	10.6	12.4	8.3	8.35
2	E. Cayman	OTF	915	15	N77E	80S	175	12.1	14.2	8.4	8.45
3a	Hispaniola	SUB	525	110	N98E	20S	70				
3b	Puerto Rico	SUB	385	110	N83E	20S	23	8.2	9.4	9.11	9.15
3c	Virgin Islands	SUB	485	110	N102E	20S	42				
4a	W. Northern Panama	OCB	200	40	N113E	30S	90	3.7	4.3	8.24	8.28
4b	E. Northern Panama	OCB	350	40	N75E	35S	90				
5a	W. Southern Caribbean	SUB	550	50	N53E	17S	90	4.7	5.4	8.46	8.5
5b	E. Southern Caribbean	SUB	200	50	N95E	17S	90				

*Faults with same numeral are treated as one tsunami source.

†See Bird (2003).

Figures

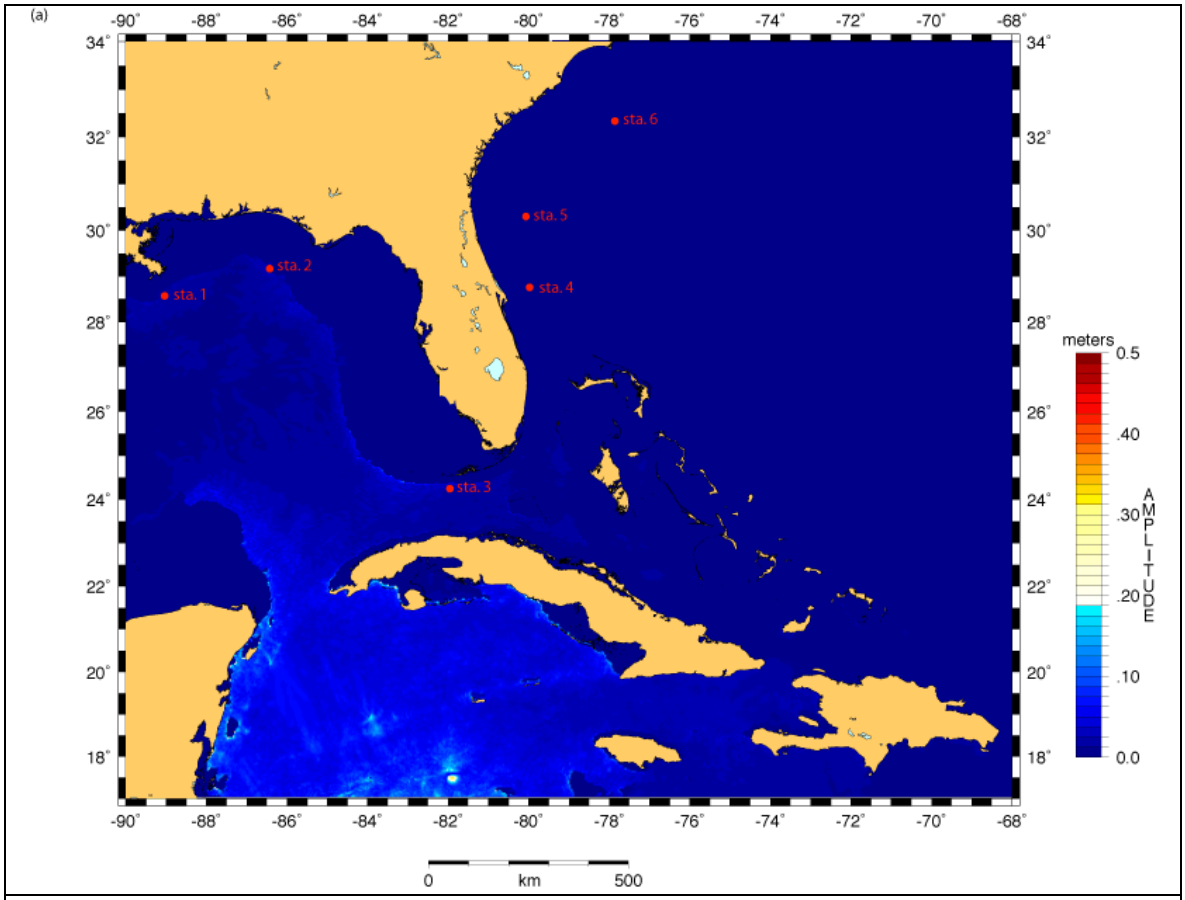

Figure 6-1 A: One simulation of maximum open-ocean tsunami amplitude over 4.4 hours of propagation time for the faults in the Caribbean: (a) W. Cayman OTF. Red dots indicate locations where synthetic marigrams are shown in Figure 6-3.

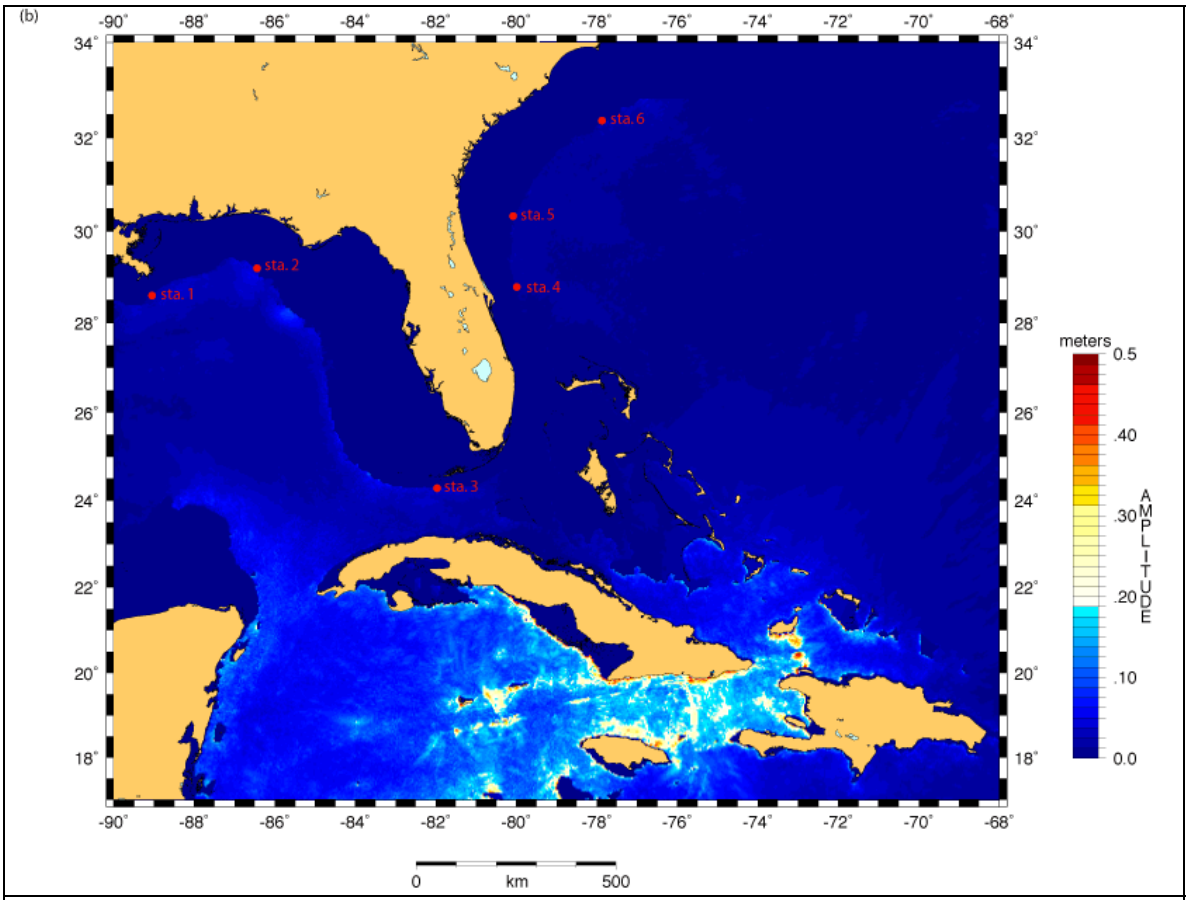

Figure 6-1 B: One simulation of maximum open-ocean tsunami amplitude over 4.4 hours of propagation time for the faults in the Caribbean: (b) E. Cayman OTF. Red dots indicate locations where synthetic marigrams are shown in Figure 6-3.

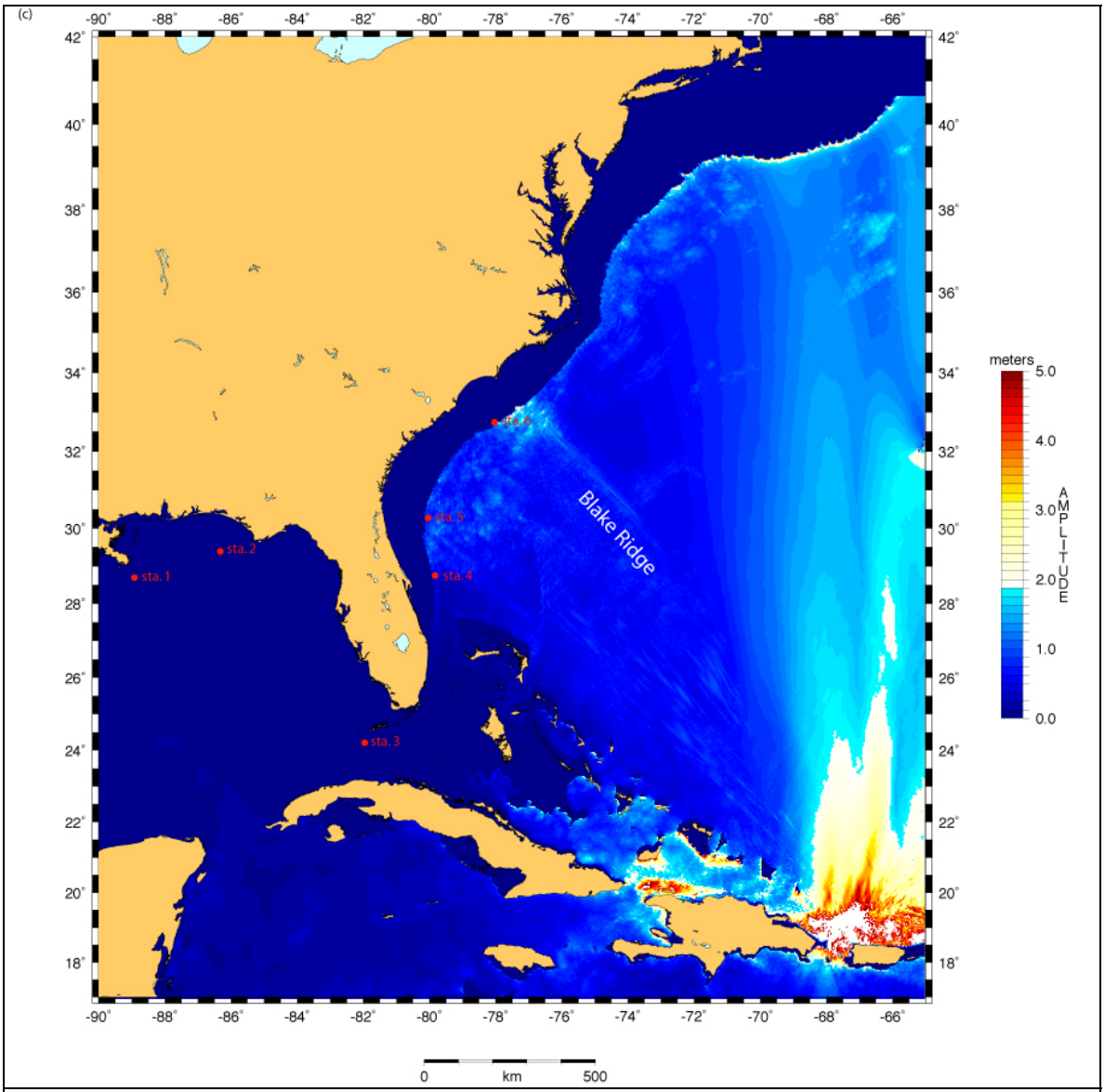

Figure 6-1 C: One simulation of maximum open-ocean tsunami amplitude over 4.4 hours of propagation time for the faults in the Caribbean: (c) N. Puerto Rico/Lesser Antilles SUB. Note change in amplitude scale for (c). Red dots indicate locations where synthetic marigrams are shown in Figure 6-3.

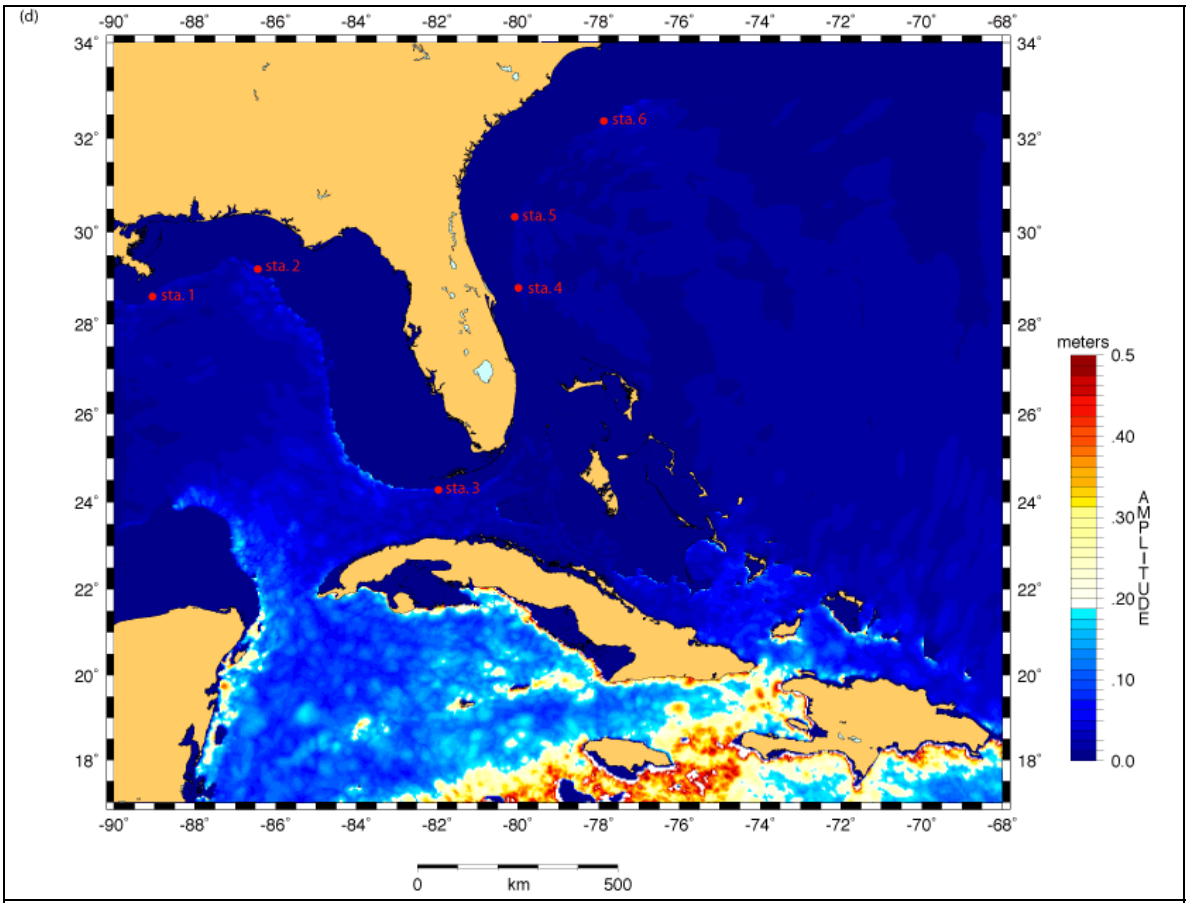

Figure 6-1 D: One simulation of maximum open-ocean tsunami amplitude over 4.4 hours of propagation time for the faults in the Caribbean: (d) N. Panama OCB). Red dots indicate locations where synthetic marigrams are shown in Figure 6-3.

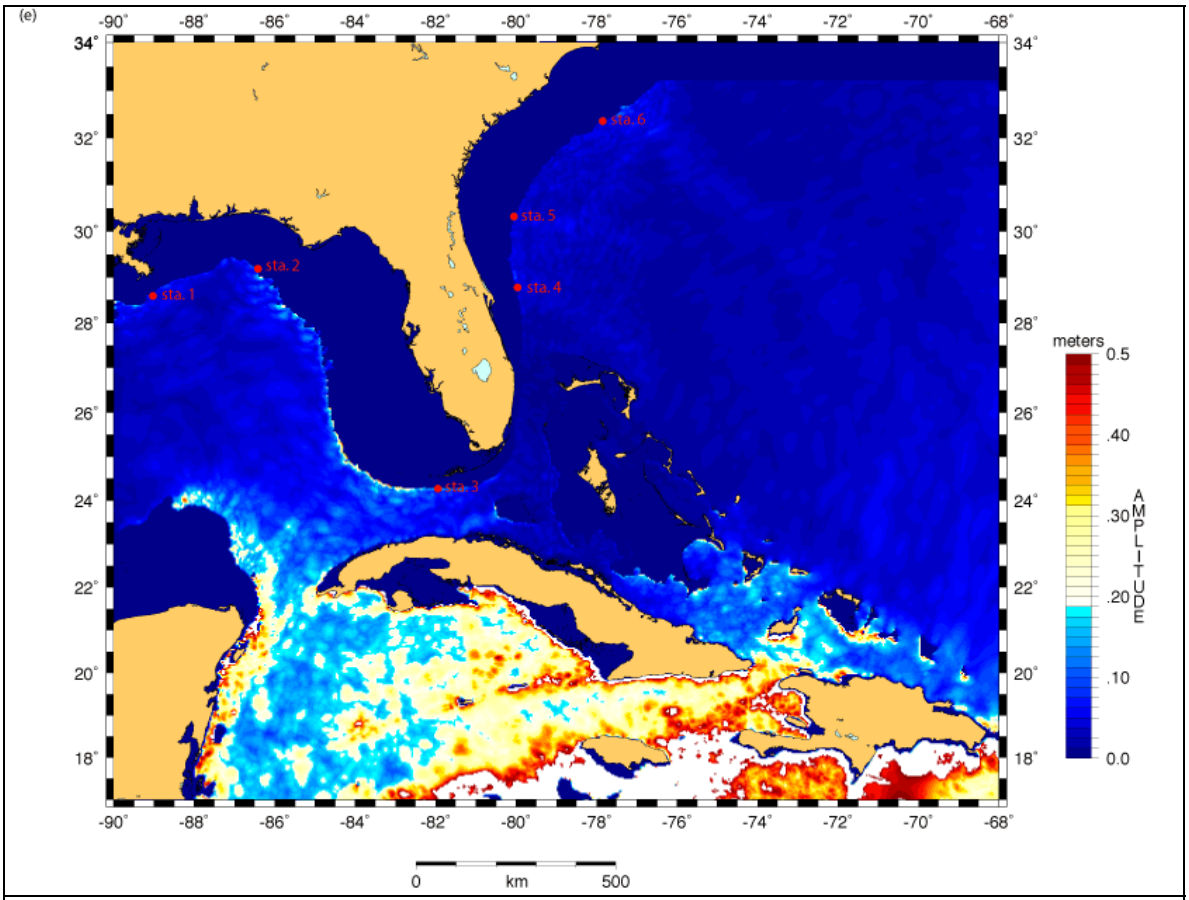

Figure 6-1 E: One simulation of maximum open-ocean tsunami amplitude over 4.4 hours of propagation time for the faults in the Caribbean: (e) N. Venezuela SUB. Red dots indicate locations where synthetic marigrams are shown in Figure 6-3.

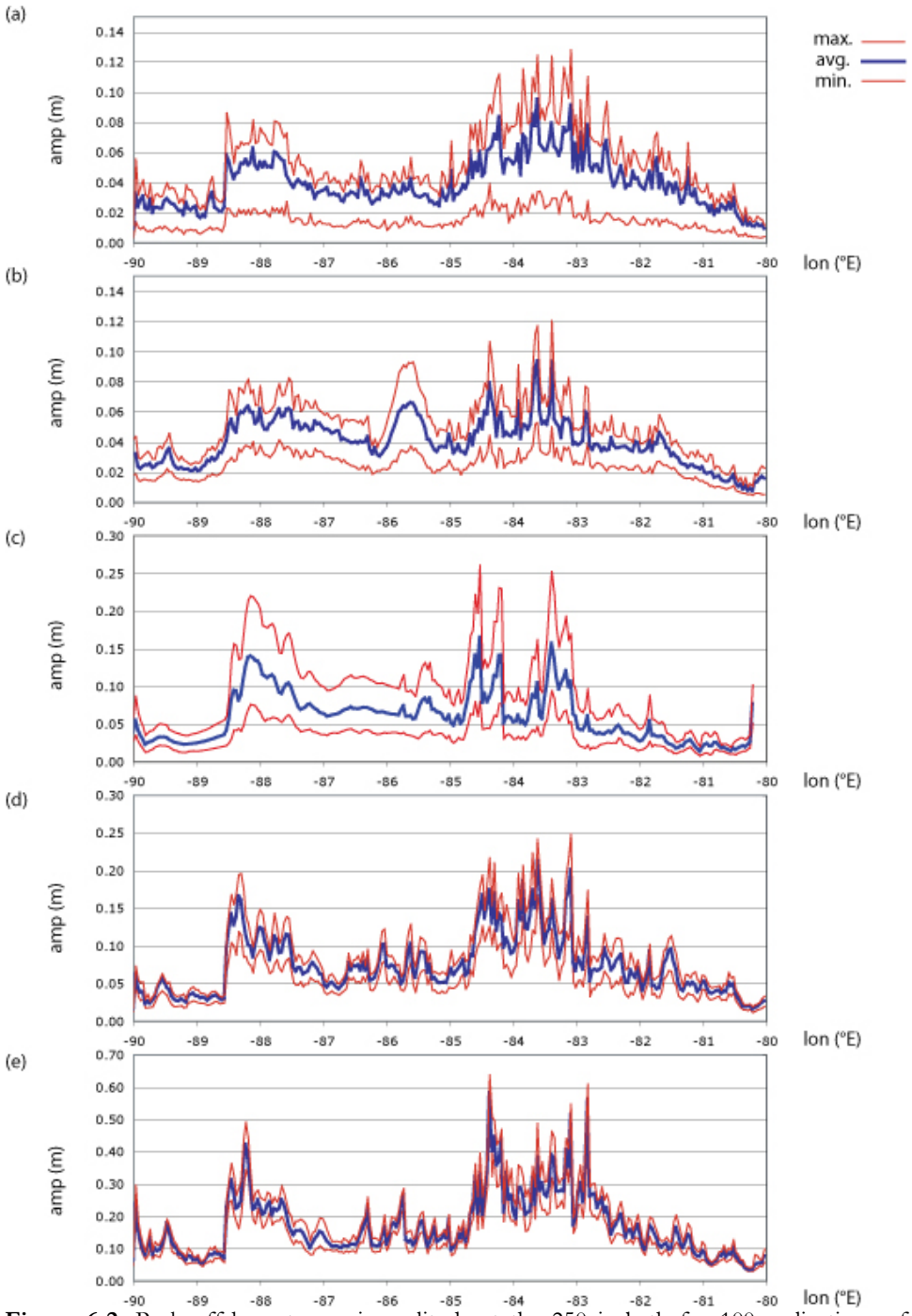

Figure 6-2: Peak offshore tsunami amplitude at the 250 isobath for 100 realizations of earthquakes on faults in the Caribbean: (a) W. Cayman OTF, (b) E. Cayman OTF, (c) N. Puerto Rico/Lesser Antilles SUB, (d) N. Panama OCB, (e) N. Venezuela SUB. Blue line shows average values; red lines extrema values. Results plotted along a latitudinal profile for the Gulf of Mexico coast. Note change in amplitude scale for (d) and (e).

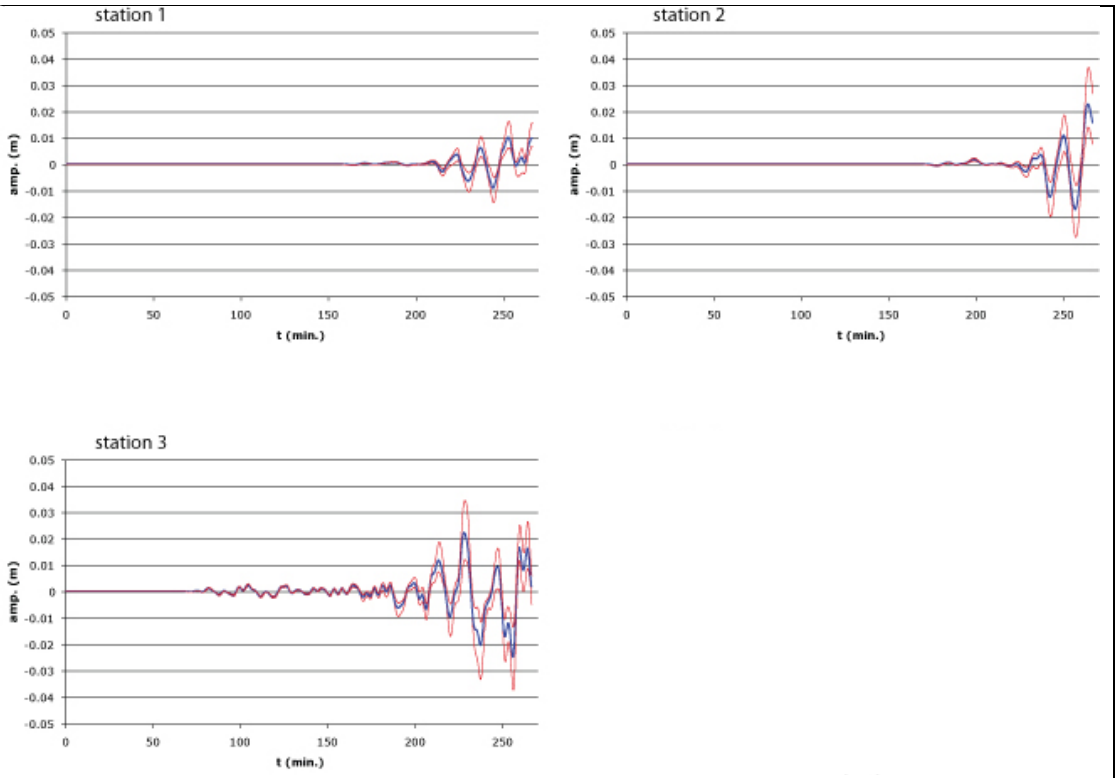

Figure 6-3 A: Range in synthetic marigrams (tsunami amplitude as a function of time) for three locations in the Gulf of Mexico shown in Table 5-1. Results shown for each of the faults in the Caribbean: (A) W. Cayman OTF, (B) E. Cayman OTF, (C) N. Puerto Rico/Lesser Antilles SUB, (D) N. Panama OCB, (E) N. Venezuela SUB. Blue line shows average values; red lines extrema values. Note changes in amplitude scale.

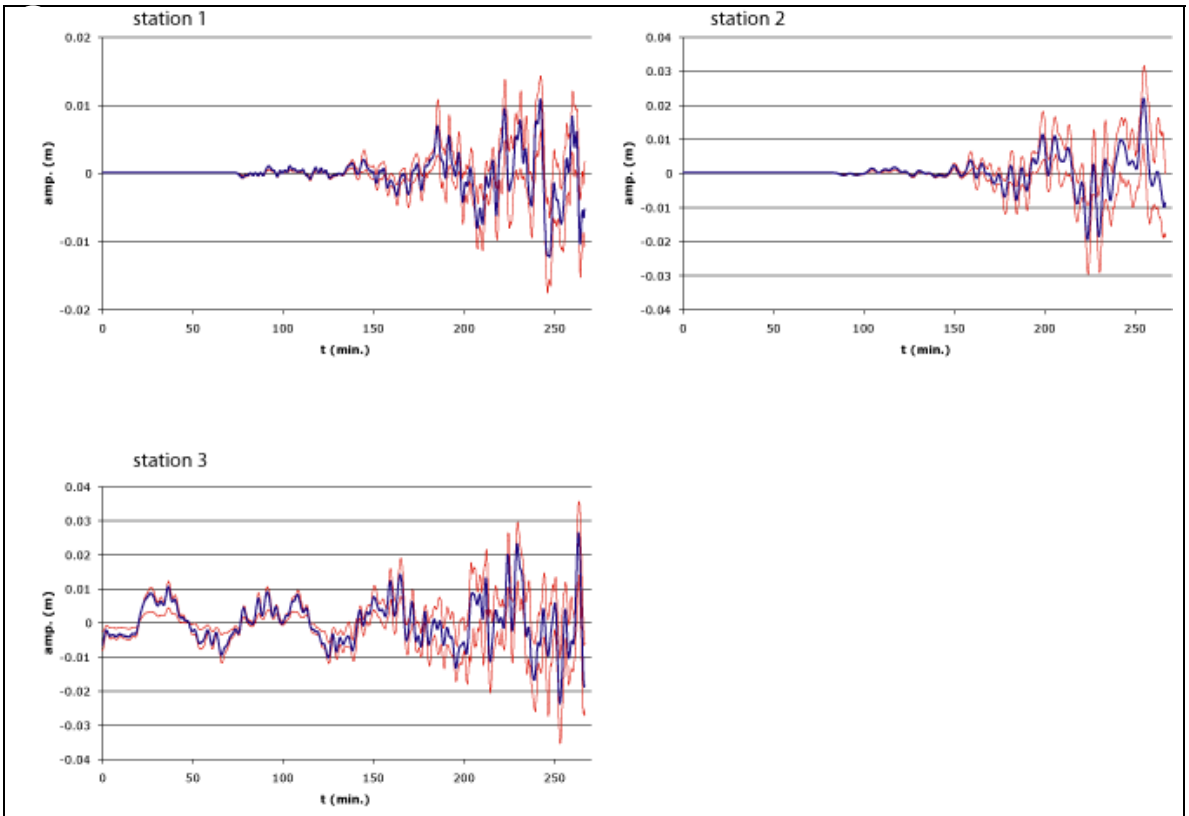

Figure 6-3 B: Range in synthetic marigrams (tsunami amplitude as a function of time) for three locations in the Gulf of Mexico shown in Table 5-1 (East Cayman OTF). Blue line shows average values; red lines extrema values. Note changes in amplitude scale.

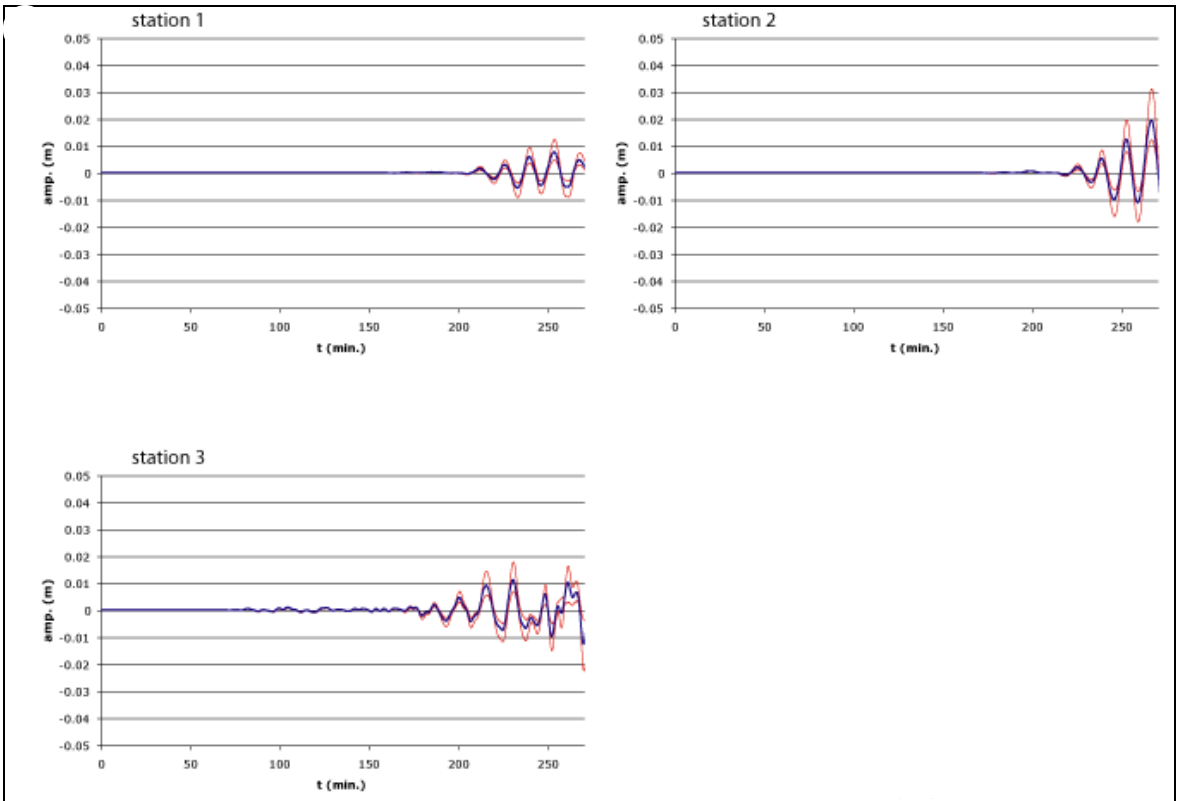

Figure 6-3 C: Range in synthetic marigrams (tsunami amplitude as a function of time) for three locations in the Gulf of Mexico shown in Table 5-1 (N. Puerto Rico/Lesser Antilles SUB). Blue line shows average values; red lines extrema values. Note changes in amplitude scale.

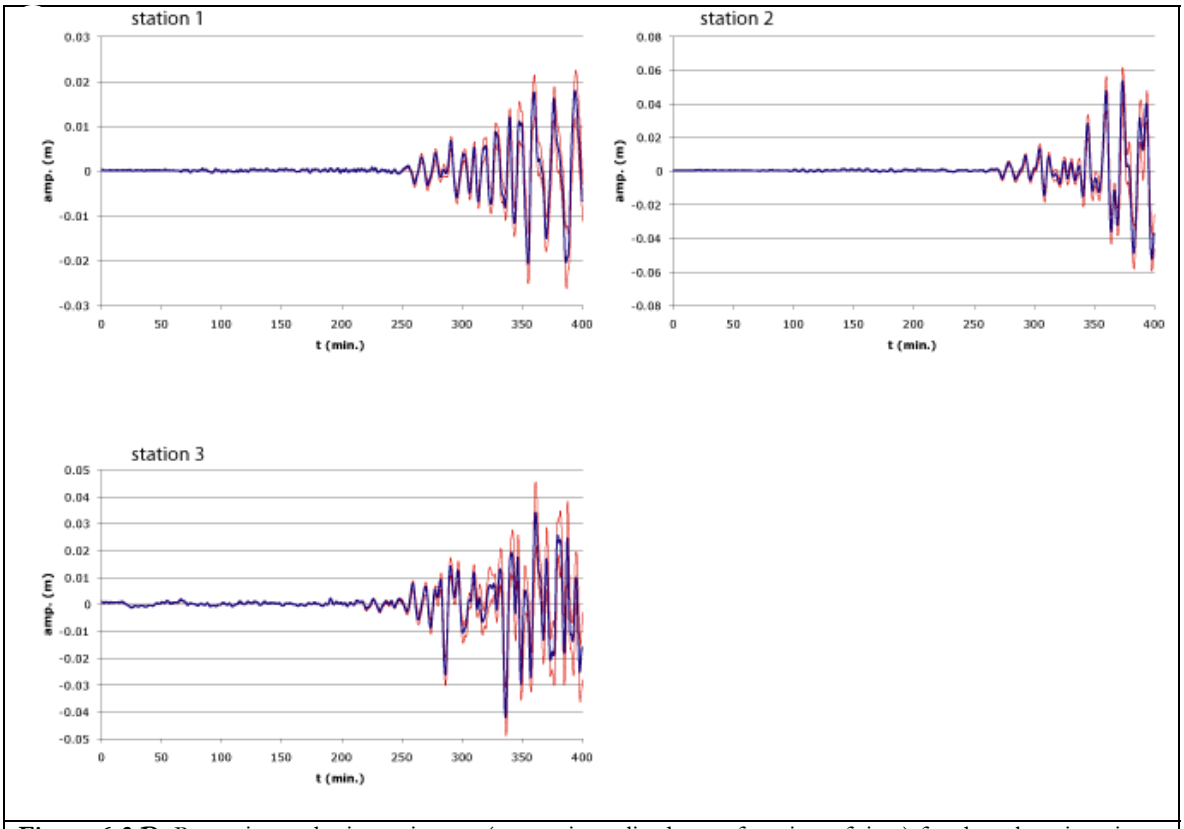

Figure 6-3 D: Range in synthetic marigrams (tsunami amplitude as a function of time) for three locations in the Gulf of Mexico shown in Table 5-1 (N. Panama OCB). Blue line shows average values; red lines extrema values. Note changes in amplitude scale.

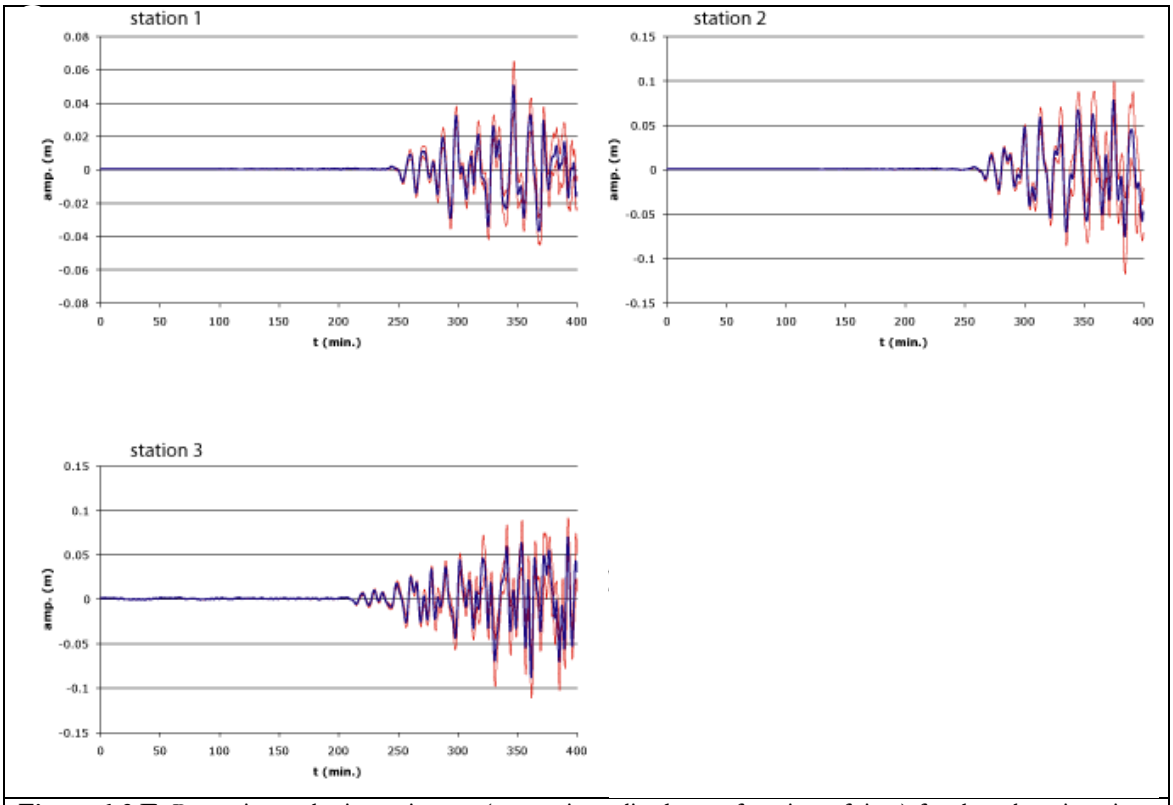

Figure 6-3 E: Range in synthetic marigrams (tsunami amplitude as a function of time) for three locations in the Gulf of Mexico shown in Table 5-1 (N. Venezuela SUB). Blue line shows average values; red lines extrema values. Note changes in amplitude scale.

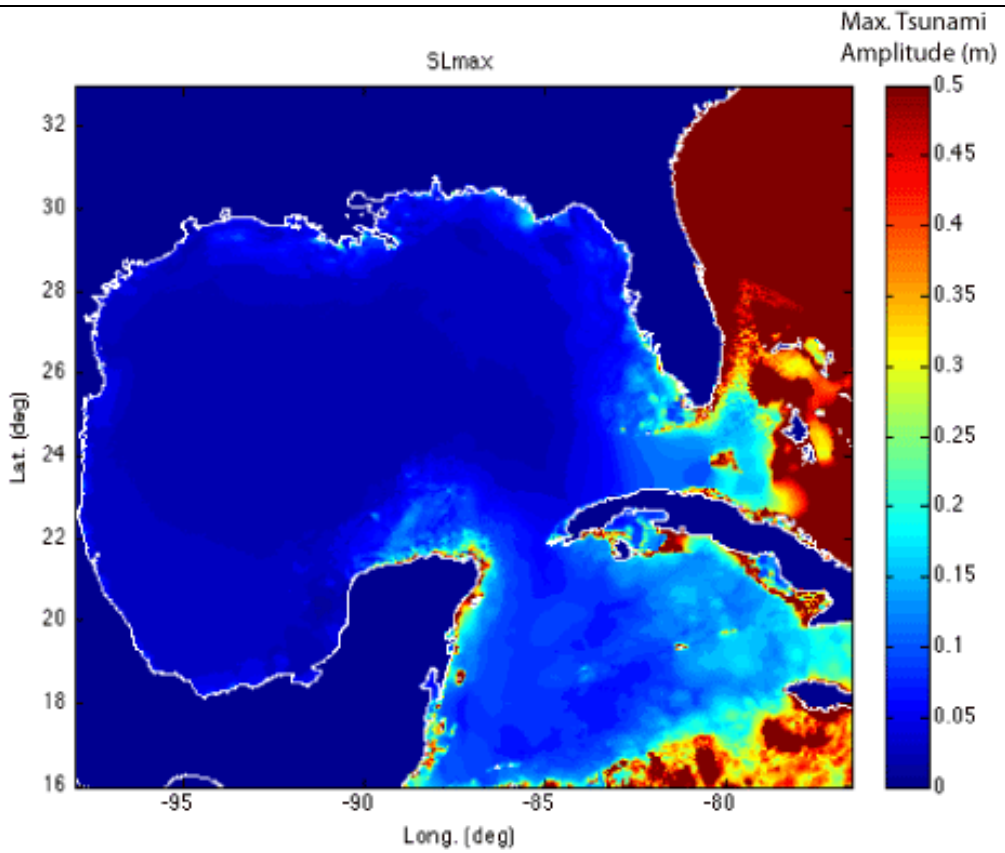

Figures 6-4: Peak tsunami amplitude over 12 hours of propagation time for a hypothetical M~9 earthquake along the northern Caribbean subduction zone. Amplitudes are clipped at 0.5 m.

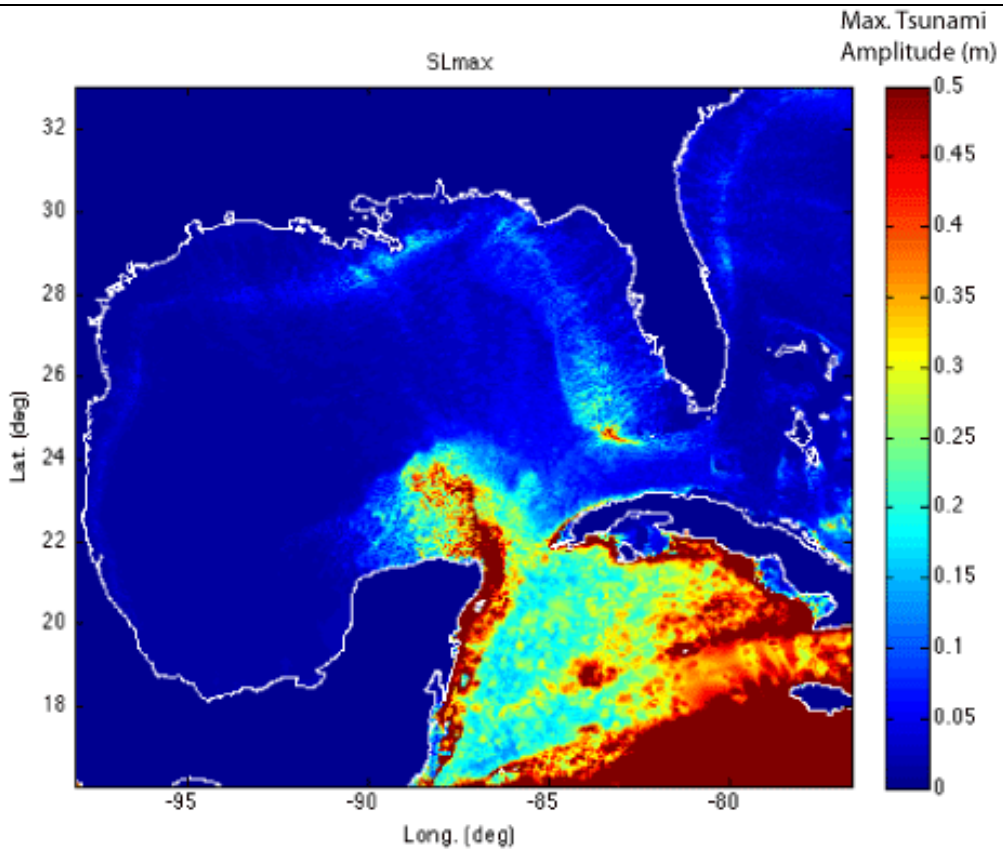

Figures 6-5: Peak tsunami amplitude over 12 hours of propagation time for a hypothetical M~9 earthquake along the northern South America convergent zone. Amplitudes are clipped at 0.5 m.

References

Barkan, R., ten Brink, U.S., and Lin, J., 2009, The source of the 1755 Lisbon earthquake: Implications for tsunami hazard to the U.S. Atlantic coast: *Marine Geology, v. 264*, p. 109-122.

Bird, P., 2003, An updated digital model of plate boundaries: *Geochemistry, Geophysics, Geosystems, v. 4*, doi:10.1029/2001GC000252.

Bird, P., and Kagan, Y. Y., 2004, Plate-tectonic analysis of shallow seismicity: apparent boundary width, beta-value, corner magnitude, coupled lithosphere thickness, and coupling in 7 tectonic settings: *Bull. Seismol. Soc. Am., v. 94*, 2380-2399.

Geist, E. L., 2002, Complex earthquake rupture and local tsunamis, J. Geophys. Res., v. 107, doi:10.1029/2000JB000139.

Geist, E. L., Titov, V. V., Arcas, D., Pollitz, F. F., and Bilek, S. L., 2007, Implications of the December 26, 2004 Sumatra-Andaman earthquake on tsunami forecast and assessment models for great subduction zone earthquakes: *Bull. Seismol. Soc. Am., v. 97*, p. S249-S270.

Herrero, A., and Bernard, P., 1994, A kinematic self-similar rupture process for earthquakes: *Bull. Seismol. Soc. Am., v. 84*, p. 1216-1228.

Knight, W., 2006, Model predictions of Gulf and southern Atlantic coast tsunami impacts from a distribution of sources: *Science of Tsunami Hazards, v. 24*, p. 304-312.

Locat, J., Lee, H.J., ten Brink, U.S., Twichell, D.C., Geist, E.L., and Sansoucy, M., 2009, Geomorphology, stability and mobility of the Currituck slide, *Marine Geology*, *v. 264*, pp. 28-40.

Lay, T., Kanamori, H., and Ruff, L. J., 1982, The asperity model and the nature of large subduction zone earthquakes: *Earthquake Prediction Research, vol. 1*, p. 3-71.

Mader, C.L., 2001, Modeling the 1755 Lisbon tsunami: Science of Tsunami Hazards, v. 19, p. 93-98.

Mei, C. C., 1989, The Applied Dynamics of Ocean Surface Waves, World Scientific, Singapore, 740 p.

Rabinovich, A. B., 1997, Spectral analysis of tsunami waves: Separation of source and topography effects: *J. Geophys. Res., v. 102*, p. 12,663-612,676.

Satake, K., 1995, Linear and nonlinear computations of the 1992 Nicaragua earthquake tsunami: *Pure Appl. Geophys., v. 144*, p. 455-470.

Satake, K., 2002, Tsunamis, *in* Lee, W. H. K., *et al.* (Editors), International Handbook of Earthquake and Engineering Seismology, Part A, Academic Press, San Diego, p. 437-451.

Satake, K., Yoshida, Y., and Abe, K., 1992, Tsunami from the Mariana earthquake of April 5, 1990: Its abnormal propagation and implications for tsunami potential from outer-rise earthquakes: *Geophys. Res. Lett., v. 19*, p. 301-304.

Shuto, N., 1991, Numerical simulation of tsunamis--Its present and near future: *Natural Hazards, v. 4*, p. 171-191.

Tanioka, Y., and Satake, K., 1996, Tsunami generation by horizontal displacement of ocean bottom: *Geophys. Res. Lett., v. 23*, p. 861-865.

ten Brink, U. S., and Lin, J., 2004, Stress interaction between subduction earthquakes and forearc strike-slip faults: Modeling and application to the northern Caribbean plate boundary: *J. Geophys. Res.*, v. 109, B12310, doi:12310.11029/12004JB003031.

Titov, V. V., and Synolakis, C. E., 1996, Numerical modeling of 3-D long wave runup using VTCS-3, *in* Yeh, H., *et al.* (Editor), Long wave runup models: World Scientific Publishing Co., Singapore, p. 242-248.

Titov, V. V., and González, F. I., 1997, Implementation and testing of the Method of Splitting Tsunami (MOST) model, Technical Memorandum, , NOAA, 11 p.

Titov, V. V., and Synolakis, C. E., 1998, Numerical modeling of tidal wave runup: *Journal of Waterway, Port, Coastal, and Ocean Engineering, v. 124*, p. 157-171.

Titov, V. V., González, F. I., Bernard, E. N., Ebel, J. E., Mofjeld, H. O., Newman, J. C., and Venturato, A. J., 2005, Real-time tsunami forecasting: Challenges and solutions: *Natural Hazards, v. 35*, p. 40-58.

Wells, D. L., and Coppersmith, K. J., 1994, New empirical relationships among magnitude, rupture length, rupture width, rupture area, and surface displacement: *Bull. Seismol. Soc. Am., v. 84*, p. 974-1002.